



CENTRO FEDERAL DE EDUCAÇÃO TECNOLÓGICA DE MINAS GERAIS
PROGRAMA DE PÓS-GRADUAÇÃO EM MODELAGEM MATEMÁTICA E COMPUTACIONAL

NUMERICAL SIMULATION OF GRANULAR MATERIALS: BRAZIL NUT EFFECT AND SEDIMENT TRANSPORT

GUSTAVO HENRIQUE BORGES MARTINS

Advisor: Allbens Atman Picardi Faria
CEFET-MG

Co-Advisor: Philippe Claudin
ESPCI - France

BELO HORIZONTE
2021 AUGUST

GUSTAVO HENRIQUE BORGES MARTINS

**NUMERICAL SIMULATION OF GRANULAR
MATERIALS: BRAZIL NUT EFFECT AND SEDIMENT
TRANSPORT**

Thesis presented to the Graduate Program in Mathematical and Computational Modeling at Centro Federal de Educação Tecnológica de Minas Gerais, as partial requirement to obtain the degree of Doctor of Philosophy in Mathematical and Computer Modeling.

Research field: Mathematical and Computational Modeling

Research line: Applied Mathematical Methods

Advisor: Allbens Atman Picardi Faria
CEFET-MG

Co-Advisor: Philippe Claudin
ESPCI - France

CENTRO FEDERAL DE EDUCAÇÃO TECNOLÓGICA DE MINAS GERAIS
PROGRAMA DE PÓS-GRADUAÇÃO EM MODELAGEM MATEMÁTICA E COMPUTACIONAL
BELO HORIZONTE
2021 AUGUST

This sheet should be replaced by the scanned copy of the approval sheet provided.

Abstract

The simulation of granular materials is studied widely in many research centers around the world, and applied in industries and engineering companies. For the understanding and quantification of granular materials properties, Discrete Element Method (DEM) is used to simulate the behavior of granular materials. Many of the challenges to understanding the behavior of granular materials begin in the dry grain segregation phenomenon. Classically, we have the Brazil-Nut Effect (BNE) - which consists of a confined granular material containing grains of different sizes which, when agitated, displays segregation, with the larger grains rising up to surface. For many years, it was believed that this segregation occurred due to the presence of walls that confine the material. In the first part of this thesis we show that in systems with periodic boundary conditions (pbc), BNE can also occur. We also proposed that BNE exhibits resonance effect, and we differentiate systems with walls and pbc by using Large-Deviation function (LDF). In the second part of this thesis we studied a different area of granular materials: sediment transport. Sediment transport occurs in the interaction between granules and fluids. To simulate the behavior of granular materials immersed in a fluid, we use a Computational Fluid Dynamics (CFD) technique. The solid sediments move in the velocity field transported by the fluid. Three dimensionless parameters are required to describe the transport: the Reynolds number, which relates the inertial forces to the viscous forces, and consequently the fluid turbulence effects; the number of Shields, which is related to the drag forces and the inertial forces of the fluid; and finally, the density ratio between the solid and the fluid phases. It is possible to reproduce the different modes of transport only by changing such dimensionless parameters. In this thesis, we calculate and characterize the saturation time for bedload transport mode in the viscous regime, and we also predict the saturation length for this transport mode. This sediment transport was possible to studied thanks to the sandwich PhD. done in PMMH-ESPCI with CAPES grant No.88881.187077/2018-01.

Keywords: Granular materials. Computer simulations. Discrete Element Method (DEM). Computational Fluid Dynamics (CFD). Brazil-Nut Effect. Sediment transport.

Resumo

A simulação de materiais granulares é estudada nas academias de todo o mundo, também aplicada em indústrias e empresas de engenharia. Para o entendimento e quantificação das propriedades dos materiais granulares, o Método de Elementos Discretos, ou *Discrete Element Method* (DEM), é usado para simular o comportamento de materiais granulares. Muitos dos desafios de se compreender o comportamento de materiais granulares têm início no fenômeno de segregação de grãos secos. Classicamente, temos o efeito castanha do Pará - *Brazil Nut Effect* (BNE) - que consiste em um material granular confinado contendo grãos de diferentes volumes e que, quando agitados, exibem segregação, sendo que os grãos maiores ascendem até a superfície. Por muitos anos, acreditou-se que esta segregação ocorria devido a presença de paredes que confinam o material. Na primeira parte desta tese mostramos que em sistemas com condição periódica de contorno também pode ocorrer o BNE. Propomos que o BNE se comporta com efeito ressonante, e diferenciamos os sistemas com paredes do com condição periódica de contorno usando a função de grandes desvios - *Large-Deviation function* (LDF). Na segunda parte desta tese estudamos também o transporte de sedimentos, que ocorre na interação entre granulares e fluidos. Para simular o comportamento de materiais granulares imersos em um fluido, utilizamos uma técnica de Fluidodinâmica Computacional, ou *Computational Fluid Dynamics* (CFD). Os sedimentos sólidos se movem em um campo de velocidades transportados pelo fluido. Três parâmetros adimensionais são necessários para descrever o comportamento do transporte: o número de Reynolds, que relaciona as forças iniciais com as forças viscosas, e consequentemente os efeitos de turbulência do fluido; o número de Shields, que está relacionado com as forças de arraste e as forças iniciais do fluido; e finalmente, a razão de densidade entre o sólido e a fase fluida. É possível reproduzir os diferentes modos de transporte apenas mudando tais parâmetros adimensionais. Nesta tese, calculamos o tempo de saturação para o modo *bedload* no regime viscoso, e também predizemos o tempo de saturação para este modo de transporte. Este estudo de transporte de sedimentos foi possível graças ao doutorado sanduíche realizado no PMMH-ESPCI com a bolsa CAPES No.88881.187077/2018-01.

Palavras Chaves: Materiais granulares. Simulação computacional. Método de Elemento Discreto (DEM). Fluidodinâmica Computacional (CFD). Efeito castanha do Pará (BNE). Transporte de sedimentos.

Résumé

Des simulation de matériaux granulaires ont étudiée en centres de recherche de tout le monde, également elles ont appliquée dans les industries et des société d'ingénierie. Pour comprenez et qualifiez des propriétés des matériaux granulaire, la Méthode de Éléments Discrètes, ou *Discrete Element Method* (DEM), est utilisée pour simuler des comportement des matériaux granulaires. De nombreux défis pour comprenez le comportement des matériaux granulaires commencement par le phénomène de ségrégation de grains secs. Classiquement, il y a l'effet noix du Brésil - *Brazil Nut Effect* (BNE) - qui consiste en des matériaux granulaires confinés contenant grains de différents volumes et qui, lorsqu'ils sont agités, présentent une ségrégation, le plus gros grains remontent jusqu'à la surface. Pendant de nombreuses années, on a cru que cette ségrégation était due à la présence de murs qui confinement le matériau. Dans la première partie de cette thèse, nous montrons que dans le systèmes avec de condition aux limites périodiques, le BNE peut également se produire. Nous avons également proposé que le BNE présente un effet de résonance, et nous différencions les systèmes avec murs et de condition aux limites périodiques en utilisant la fonction de grande déviation. Dans la deuxième partie de cette thèse, nous avons étudié un autre domaine des matériaux granulaires : le transport des sédiments. Le transport des sediment se produit dans l'interaction entre le granules et les fluides. Pour simuler le comportement de matériaux granulaires immergés dans un fluide, nous utilisons une technique de Dynamique des Fluides Computationnelle, ou *Computational Fluid Dynamics* (CFD). Les sédiments solides se déplacent dans un champ de vitesses portées par le fluide. Trois paramètres adimensionnels sont nécessaires pour décrire le comportement du transport: le nombre de Reynolds, qui est lié aux forces d'inertie aux forces visqueuses, et par conséquent aux effets de la turbulence des fluides; le nombre de Shields, qui est lié aux forces de traînée et aux forces d'inertie du fluide; et enfin, le rapport de densité entre le solide et la phase fluide. Il est possible de reproduire les différents modes de transport simplement en modifiant ces paramètres adimensionnelles. Dans cette thèse, nous calculons et caractérisons le temps de saturation pour le modes de transport charrié en régime visqueux, et nous prédisons également la longueur de saturation pour ce mode de transport. Ce transport sédimentaire a pu être étudié grâce à le stage de thèse fait au PMMH-ESPCI avec la bourse CAPES 88881.187077/2018-01.

Mots clés: Matériaux granulaires. Simulation par ordinateur. Méthode des éléments discrets (DEM). Dynamique des fluides computationnelle (CFD). Effet de Noix du Brésil (BNE). Transporte de sédiments.

List of Figures

Figure 1 – Examples of granular materials.	5
Figure 2 – Granular phases.	6
Figure 3 – Angle of repose and angle of movement.	7
Figure 4 – Pathway of force chain.	8
Figure 5 – Example of force chain.	9
Figure 6 – Arch in a funnel.	9
Figure 7 – Effect of the preparation history using funnel and sieve.	10
Figure 8 – Stress response in ordered/disordered granular packings.	11
Figure 9 – Cavity formed by a fixed intruder in a dense granular packing.	12
Figure 10 – Granular scales.	12
Figure 11 – Contact force model.	16
Figure 12 – Friction.	18
Figure 13 – Neighbor search.	21
Figure 14 – Granular convection in vibrated bed.	24
Figure 15 – BNE cycles.	25
Figure 16 – Intruder height in an agitated media.	26
Figure 17 – Phase diagram of BNE: density ratio and size ratio.	27
Figure 18 – Phase diagram of BNE: Γ and v_c .	27
Figure 19 – Phase diagram of BNE/RBNE from experiment: density ratio and size ratio.	28
Figure 20 – Phase diagram of BNE/RBNE from analytics: density ratio and size ratio.	28
Figure 21 – Phase diagram of BNE/RBNE in swirling: density ratio and size ratio.	29
Figure 22 – BNE snapshot.	31
Figure 23 – BNE with walls: sample of intruder positions.	32
Figure 24 – BNE with frictional walls: $\rho_I/\rho_g = 1$.	32
Figure 25 – BNE with frictional walls: $\rho_I/\rho_g = 1/3$.	33
Figure 26 – BNE with frictional walls: $\rho_I/\rho_g = 1$.	33
Figure 27 – BNE with frictionless walls.	34
Figure 28 – BNE with frictional walls: Ascent rate versus Γ .	35
Figure 29 – Frictionless grains and walls.	36
Figure 30 – BNE with periodic boundary: sample of intruder positions.	36
Figure 31 – BNE with periodic boundary: time series.	37
Figure 32 – BNE with periodic boundary: resonance.	37
Figure 33 – BNE with periodic boundary: resonance collapse.	38
Figure 34 – BNE with periodic boundary: resonance fitting parameters.	38
Figure 35 – BNE with periodic boundary: $25d$ and $37.5d$.	39
Figure 36 – BNE with periodic boundary: large deviation.	40

Figure 37 – Steady-state analytical solution for viscous fluid profiles.	44
Figure 38 – Temporal solution for viscous fluid profiles.	46
Figure 39 – Normalized profiles for viscous fluid.	47
Figure 40 – 1 st Fourier mode for viscous fluid velocity.	48
Figure 41 – Transport modes.	55
Figure 42 – Transport volumetric flux.	56
Figure 43 – Transport profiles.	61
Figure 44 – Transport laws for viscous bedload transport.	62
Figure 45 – Temporal transport transition.	63
Figure 46 – Saturation time T_{sat} for the transport.	64
Figure 47 – Saturation length L_{sat} for the transport.	66
Figure 48 – Steady-state numerical solution for viscous-turbulent fluid profiles.	99

List of Tables

Table 1 – Table of units normalization related to the fluid.	54
--	----

List of Frames

List of Algorithms

Algorithm 1 – DEM algorithm.	20
Algorithm 2 – Neighbor list.	21
Algorithm 3 – Predictor.	21
Algorithm 4 – Detect contacts.	22
Algorithm 5 – Force calculation	23
Algorithm 6 – Corrector	23
Algorithm 7 – DEM+CFD algorithm.	51
Algorithm 8 – Force calculation with fluid force	52
Algorithm 9 – Update fluid.	53
Algorithm 10 – Thomas' algorithm.	53

List of Abbreviations and Acronyms

BNE	Brazil-Nut Effect
CFD	Computational Fluid Dynamics
DEM	Discrete Element Method
MD	Molecular Dynamics
LDF	Large Deviation Function
pbc	Periodic boundary condition
FDM	Finite Discrete Method

List of Symbols

G	Galileos number
R	Reynolds number
Θ	Shields number
ρ	Density
Γ	Dimensionless number that compares shaken acceleration and gravity
ω	Oscillation frequency of shaken systems
ϕ	Packing fraction

Contents

1 – Introduction	1
1.1 Justification	2
1.2 Motivation	2
1.3 Workflow	3
2 – Granular Materials	4
2.1 Theory	4
2.2 Fenomenology	6
3 – Discrete Element Method - DEM	14
3.1 Equations of motion	14
3.1.1 Force model	15
3.1.1.1 Rheological model of grains	16
3.1.1.2 The external force: Gravity	18
3.1.2 Temporal discretization	19
3.2 Algorithm	19
3.2.1 Neighbors	20
3.2.2 Predictor	21
3.2.3 Detect contacts	22
3.2.4 Force calculation	22
3.2.5 Corrector	22
3.3 Important parameters	22
4 – Brazil Nut Effect (BNE)	24
5 – Result Analysis and Discussion - BNE	30
6 – Methodology - CFD	41
6.1 The fluid model	41
6.1.1 Viscous steady-state regime	43
6.1.2 Viscous transient regime	44
6.2 Force model - Fluid forces	48
6.2.1 Temporal discretization	49
6.3 Algorithm	51
6.3.1 Force calculation	51
6.3.2 The fluid	52
6.4 Important parameters	53

7 – Transporte de Sedimentos	55
7.1 Threshold	57
7.2 Contribution of moving grains	58
8 – Result Analysis and Discussion - Sediment transport: Viscous Bedload	60
8.1 Steady and homogeneous transport	60
8.2 Temporal response and saturation time	61
8.3 Spatial perturbation and saturation length	64
9 – Conclusions	67
9.1 Future works	67
Referências	68
APPENDIX	75
Appendix A–Artigos publicados	76
A.1 <i>Large-deviation quantification of boundary conditions on the Brazil nut effect</i>	76
A.2 <i>Methods of parallel computation applied on granular simulations</i>	76
A.3 <i>Mechanical properties of inclined frictional granular layers</i>	81
A.4 <i>Non-Gaussian behavior in jamming / unjamming transition in dense granular materials</i>	91
Appendix B–Códigos	96
Appendix C–Turbulence	97
C.1 Turbulent steady-state regime	97
C.1.0.1 A little bit more complicated mixing length	99
ANNEX	100
Annex A–Solving the diffusion equation	101
Annex B–Runge-Kutta	103

1 Introduction

Granular materials are present in various contexts of nature and in many human activities [1, 2, 3, 4, 5]. Economic activities, like agricultural production, mining and building technology, are essentially linked to the usage of granular materials [2]. For many years, research in granular materials were linked mainly to engineering [6, 7, 8], in order to optimize production process, storing, transportation, and structural applications to these materials. Nowadays, some areas of physics, such as statistical mechanics [9], study intensively the characterization and behavior of these materials, and as well applications, due to the richness of observed phenomena. Its ubiquity reflects the importance of studies about it to better understand their manipulation in the most diverse situations.

Granular materials can be characterized as a cluster of bodies larger than a few hundred micrometers up to the size of asteroids [2, 3]. In addition to the size, another feature of bodies is that they are individually in solid state. Their interactions result in energy dissipation, either by friction or by inelastic collisions interaction. They are not subject to movement caused by thermal fluctuations, and therefore, do not exhibit Brownian motion. More characterizations of granular materials can be found in the Chapter 2 of this thesis.

The aim of this work is to computationally simulate granular materials, using Discrete Element Method (DEM), specifically based on the Molecular Dynamics (MD) [10]. The simulations are in 2D, with grains that have circular geometry, hard-core potential repulsion when in contact, and are under the action of gravity. To simulate the contacts, we also take into account the Coulomb friction between the grains. Once the properties of the materials are defined, such as hardness, friction, mass, position and radius, we apply Newton's laws of motion to perform the simulation. We detail these equations and peculiarities of the simulation of dry granular materials in the Chapter 3.

Among the phenomena presented by the dry granular materials, we were interested this thesis in the Brazil Nut Effect (BNE), related to the segregation of confined grains when submitted to the vibration, and in the presence of a gravitational field. Larger grains segregate to surface, while smaller grains sink to bottom. The Chapter 4 provides more details about the phenomenology of BNE, as well the numerical approach employed. The results and the discussion about BNE phenomena we studied are presented in Chapter 5.

Associated with DEM, we are interested in simulate granular materials carried by fluids and characterize the transport mode of bedload, using Computer Fluid Dynamics (CFD). The fluid flows homogeneously in one direction and varies in another, making the simulation of the fluid been in 1D. In this thesis we describe the technique to simulate 1D flow in viscous regime and a turbulent approach, in Chapter 6, and how to link it with the

granular phase.

We also researched the phenomenon of sediment transport in fluids interested in. The Navier-Stokes [11, 12] equation is used in this work to model the fluid that flows and carries part of the granular materials with. There are some transport modes that are characterized by the way the grains are transported by the fluid, which are briefly described in the Chapter 7. In this thesis, we focused in the bedload transportation mode, and the results of our work are presented in Chapter 8.

1.1 Justification

Because we realize that there is still a lack of understanding in the phenomena involving granular materials, we propose to study in this thesis the techniques that can predict the behavior of the conglomerate, or to characterize some emerging properties of the system that has not yet been reported or documented, as well as to use results already known from the materials, and try to apply them in other areas where measurement is difficult.

Specifically, we will deal with a subject that has not yet been reproduced in the literature: BNE in two dimensions with periodic boundary conditions. To analyze this problem we use computer simulations and the Large Deviation Function (LDF) [13] technique.

We also computed by simulations the saturation time scale¹ and the saturation length scale² of the material for the viscous bedload regime when transported by a fluid. Such measurement is quite difficult to achieve in experiments due to the scales we are treating.

1.2 Motivation

In the context of engineering, it is necessary to understand how the processes are elaborated, in order to adjust them to optimize the production costs, transportation and storage of materials essential to human activities, such as food and ores. In this sense, the understanding of the behavior of these materials, when subjected to certain conditions, allows them to be manipulated in the way of greatest interest, whether due to the need to conserve the material, either due to faster transport or the efficiency of another parameter in which it is intended spend less resources or have the greatest financial, energy or social return.

¹ Saturation time in sediment transport indicates the characteristic time it takes for the material to enter a steady state, leaving a configuration and arriving at the final configuration.

² Saturation length in the sediment transport indicates the characteristic length it takes for the material to enter its normal flux regime, when there is a difference of concentration of the material according to the space.

In grain segregation, problems related to clogging may occur depending on the geometry of the materials [14]. When these materials are subjected to vibration, or when they flow, the larger ones are naturally separated from the smaller ones, thus facilitating the filtration, but making it difficult to mix. These sets of agglomerates can have negative consequences for industrial process, such as wear of silos related to the resistance of materials, corrosion of the silo or granular, rotting or aging of stored food, etc. [15].

Thus, understanding how the granular materials interact and how they are transported, whether transported on a conveyor belt, or carried by the currents of a river, gives the possibility to control its possible effects, or to predict its consequences, such as the amount of residues remaining in the rivers due to the collapse of the Fundão dams in Mariana-MG in November 2015 [16, 17, 18], and the Brumadinho dam in January 2019 [19, 20, 21].

1.3 Workflow

This work is divided into a bibliographic review on granular materials, in Chapter 2, with phenomenology on the study of granular materials. The descriptions of the Chapter 3 relates to the equation of motion and modelling of the granular phase, concerning the interaction forces between grains and how the governing equations are implemented in this system. The Chapter 4 refers in particular to the phenomenon known as BNE and the proposition of this work in studying the dry granular. In Chapter 5 we present the first part of the results of this thesis. The Chapter 6 relates to the equation of motion and modelling the fluid phase, relating to the interaction between grains and fluid in different regimes. The Chapter 7 represents the characterizations of each transport mode, and the descriptions of the transport of materials by fluids in laminar regime. The Chapter 8 contains discussions on the results obtained, referring to the transport of sediments. The Chapter 9 presents the conclusions of this thesis and perspectives for the continuation of this work.

2 Granular Materials

Granular Materials are sets of solid bodies, composed by a given material or different materials. They can have a varied geometries, different densities, friction coefficients, hardness *etc.*, but an individual grain must be larger than $100\mu\text{m}$ [2] to ensure the athermous nature. The solid bodies that composes granular materials should be large enough to do not present kinetic fluctuation induced by thermodynamic temperature. Therefore, Brownian motion do not play a role in those systems. Granular materials interact each other when they are in contact, loosing energy by inelastic collision, as well as by friction.

Inelastic collision occurs when two or more grains collide losing part of their initial kinetic energy, in which they have transformed these loss to heat and they may deform in the process [22]. We are modeling the inelastic collision between two grains in section 3.1.1.1.

2.1 Theory

Examples of granular materials includes sand, stones, soils, drugs, ores, grain foods (rice, corn, soybeans *etc.*), even the asteroid belt and Saturn's rings. The sand alone constitutes 10% of the materials on surface of planet Earth. Besides that, it is estimated that the second most used material in industries are granular materials, using approximately 10% of all the energy on the planet, whether in extraction, transport, or processing, with the most used material being water [2].

Due to the absence of Brownian movements, as well as the dissipation of energy in the contacts, granular systems does not undergo spontaneous relaxation of its stable configurations in the absence of external disturbances, and therefore do not present ergodicity. An ergodic system has the characteristic of visit their micro-states of energy spontaneously, implying that their states are all equiprobable when a very long time is taken in account [9, 23].

To demonstrate this non-ergodicity, we can think about a pile of dry sand that rests at a base. If this base does not oscillate, the structure of the pile does not change, the structure of internal forces will remain unchanged, even if it is heated or cooled. This means that sand grains cannot transit between all equipotential states spontaneously, and then this sand pile will rest with internal configurations (chain-forces, stress tensors, grain contact, *etc.*) unchanged. In the section 2.2, one can find more details.

Granular materials also have particularities regarding their phases-like, analogously to the state of matter. They are presented individually in solid bodies, and when the grains are close to rest, they constitute the equivalent solid phase. However, if the granular system

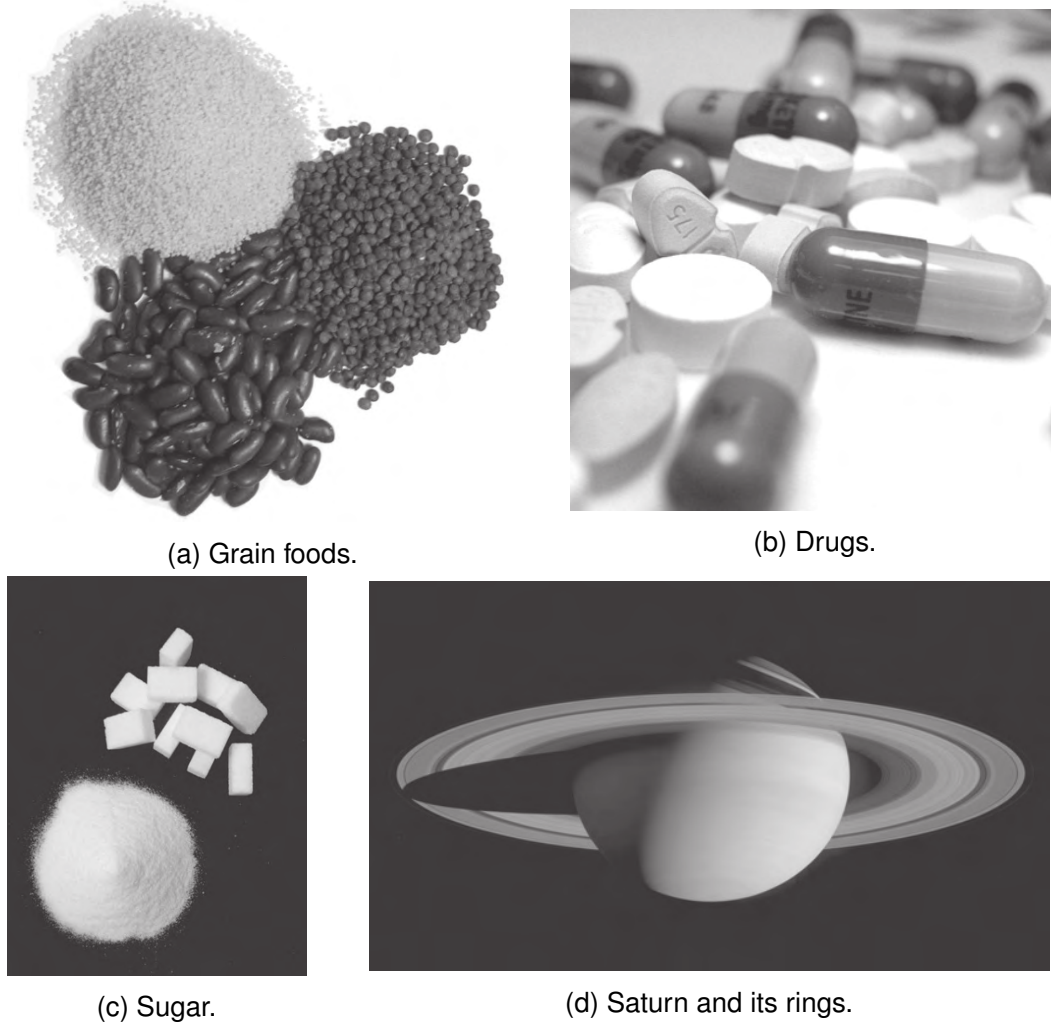


Figure 1 – Examples of granular material. Figures taken from [1].

is slightly agitated, or configured beyond a critical threshold of angle of rest, its behavior can be similar of the liquid. Solid-like and liquid-like granular can coexist and a boundary layer may appear, that indicates the liquid-like flows over the solid-like. When a granular system is vigorously agitated, the behavior is alike gases, they tend to occupy large part of the container which contains them, meaning that its packing fraction (ϕ) is low and the number of contacts between grains are much rarer, compared to the granular liquid-like and solid-like. An example of the granular states is shown in Figure 2, where the solid-like phase is in the bottom, the liquid-like phase is flowing through layers in the middle, and the gaseous-like phase is flowing in a higher disordered portion at top. Such classification is still open in the literature, although there are proposals for what would be the granular temperature of the system, in analogy of thermal temperature [24].

Packing fraction is the measure of the occupied space by the solid portion in relation of the total space occupied by the system.

A differentiation between granular systems can be a direct result of the interaction forces between grains. Systems that have only repulsive interactions are called dry granulars,

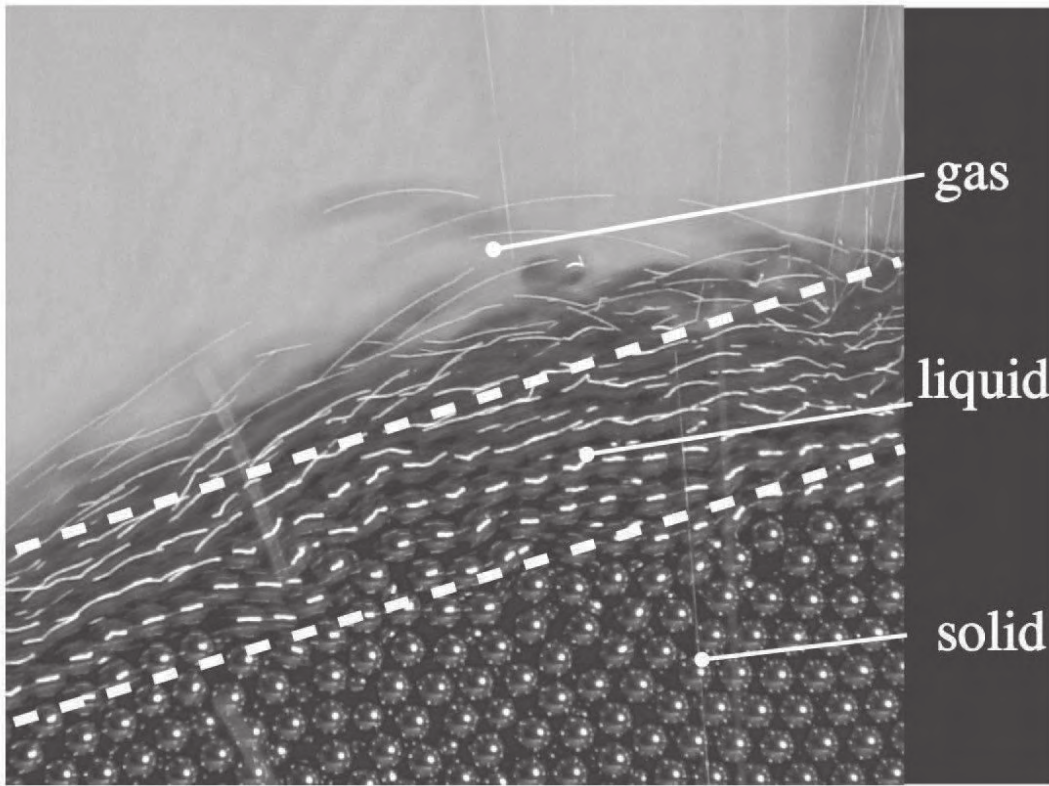


Figure 2 – Example of three granular phases according their kinetic energy. Dashed line is a proposition of the phase-like separations. The gas-like, referred as gas in the Figure, phase is much more agitated and the contact between grains in this region is rare, compared to the other phases-like. The liquid-like phase, referred as liquid in the Figure, is able to move, but still the slide each other. The solid-like phase, referred as solid in the Figure, is an immobile region that grains are in contact each other and this contact does not change over time. Figure taken from [1].

while wet granulars have van der Waals forces in grain-to-grain interactions. In this thesis, we will only consider repulsive contact interactions, although in some cases, there is a fluid surrounding the material. We consider that all the material that is involved by the fluid does not suffer forces of attraction, and therefore, van der Waals force is not included in the interaction between the grains.

2.2 Fenomenology

Perhaps the first image related to granular materials remit to the sand pile. In this case, a static pile of sand is heaped on a surface. In a pile like the one shown in Figure 3, the deposition of the grains forms an angle θ_m as large as possible, called the angle of movement, and when more material is placed on the pile, the upper layers of the pile run down to the base, restoring the angle to the lowest value θ_r , called the angle of repose [2, 4]. The rearrangement of the sand pile after the avalanche can be understood as an example of

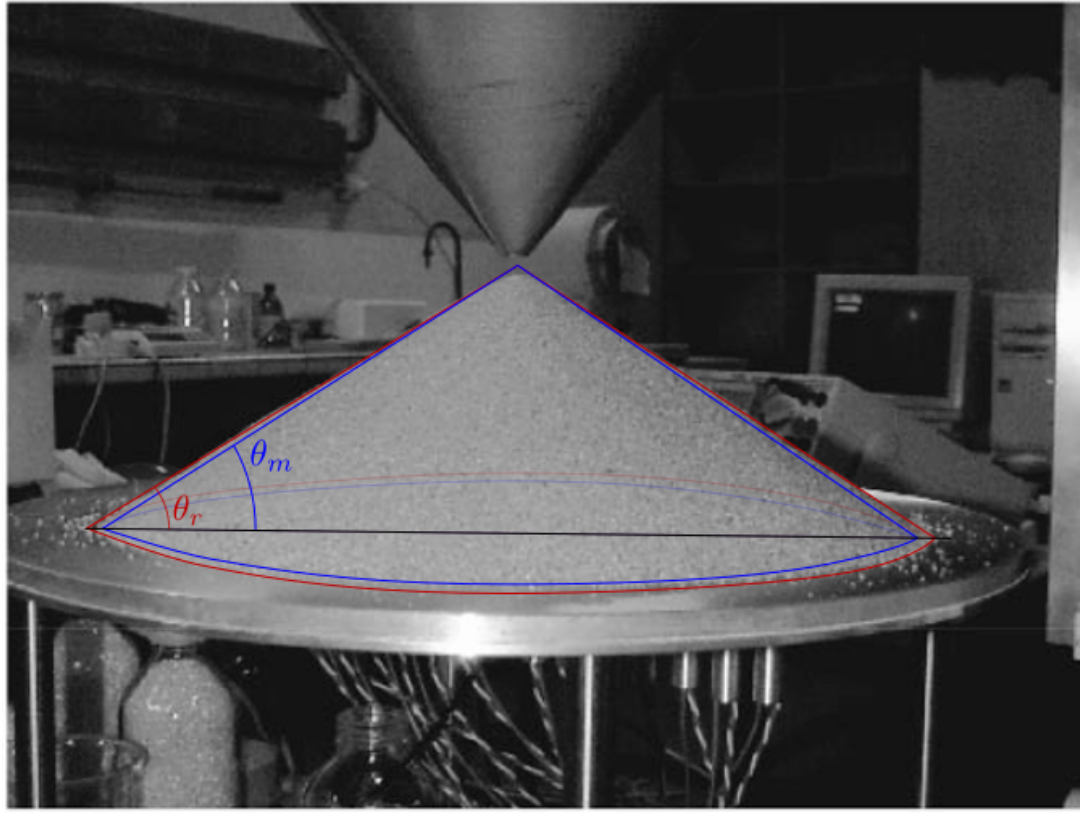


Figure 3 – Example of angle of repose θ_r and angle of movement θ_m in sand. The common values for these angles are $\theta_r = 33^\circ$ and $\theta_m = 35^\circ$. Figure taken from [33].

self-organized criticality in granular materials. A good approximation to the angle of repose is given by:

$$\tan(\theta) = \mu_s, \quad (1)$$

where θ is the angle of repose, and μ_s is the coefficient of static friction of the material's surface.

A system which has no central controller, governed by various agents that interact with rules known in the interaction of agents, and exhibit unforeseen property feature a Complex System. A characteristic property of Complex Systems and granular materials is self-organization. Some authors [25, 26, 27, 28, 29, 30, 31, 32] classify granular materials within the area of study Complex Systems.

Avalanche is the process phenomena that dropping some few grains in a pile part of the surface slides.

Also in sand piles, the preparation method of the system is reflected in the angle of repose [34]. This preparation history allows the system to be configured differently, and therefore, the angle of repose can assume different values using the same material. The angle of repose depends on the relaxation mode in which the pile was made: an inertial mode that relaxation is faster, and a collective mode that relaxation is slower. These dynamics in the angle of repose are called bistability of the angle of repose.

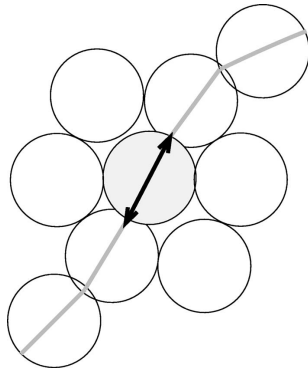


Figure 4 – Portion of an idealized force chain. The transmission of the force coincides with the direction of the contacts between grains, forming a path. Figure taken from [35].

Another common property of dense granular materials is the force chain, which is the force arrangement through the compressed media. Force chains carry most part of the forces of the media and usually the compression stress coincide with the direction of the force chain [35, 36]. The number of grains carrying larger force than the average force decays exponentially with increasing contact force. The force chain is a pathway that the force is transmitted, as shown in Figure 4. The interconnection between two or more branches of force chains forms a force network. The force network is then a subset of the contacts network. The experimental importance of visualizing the chain forces lies in understanding the distribution of the internal forces that sustains the material. As an example, Figure 5 reveals the chain of forces due point force applied on the top of the granular material.

Chains of forces are important to understand the phenomenon that is present in the arching effect. Arches are collective structures that have mutual support, and, consequently, a chain of forces linking the entire structure, being able to support their own weight and that of all the grains above, preventing them from flowing. In the formation of arches, segregation effects can occur, as verified by Magalhães, C. [14] and the flow regimes in a funnel reported by Magalhães, F. [38]. Figure 6 is an example of arch and its chain forces.

To better comprehend the rheology of dense granular materials, there is also the stress tensor, which is a macroscopic quantity of the outer product of contact force between grains and the displacement vector around the analyzed volume [4, 40, 41, 42, 43]. The stress tensor in granular materials shows us the preferable direction of a force propagation in the general form, and with it, one can infer how this granular assembly was built [33], like in Figure 7.

An evidence that the preparation history changes the configuration of the material is described in the references [33, 37]. The circular base shown in Figure 7 was made with two different depositions and the pressure profile is measured along the center. In the experiment, the pressure measured at the base varies according to the deposition, with the deposition made from the funnel having a maximum peak pressure around 0.25 and 0.5 of

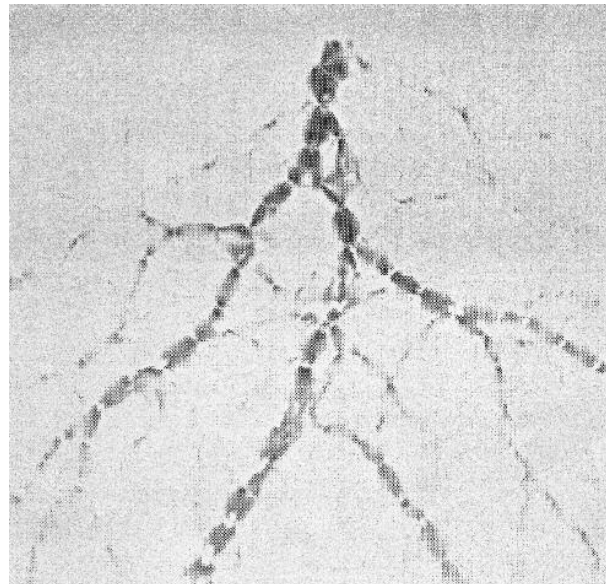


Figure 5 – The application of a point force on top of the material results in the chain of forces, which can be seen in the system's response function, after the gravitational component was subtracted from it. In this case, the system contains photoelastic grains in a two-dimensional space. Photoelastic grains diffract light differently when a force is applied on it. The force applied on a photoelastic grain produces different tensions, which can be seen by lighting it with a polarized light, and then a polarizing plate blocks the non polarized light. The darker, the greater the stress in the material. Figure taken from [37].

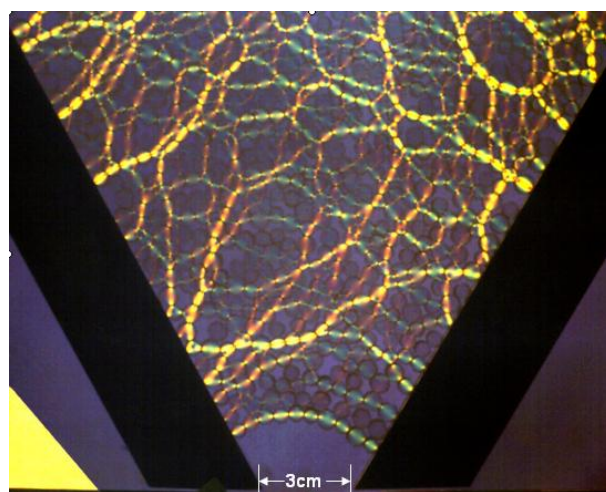


Figure 6 – Arch formation in a funnel. Photoelastic grains were used to display the chain forces, and clearly there is a blocking arch with a chain force sustaining all grains above. Figure taken from [39].

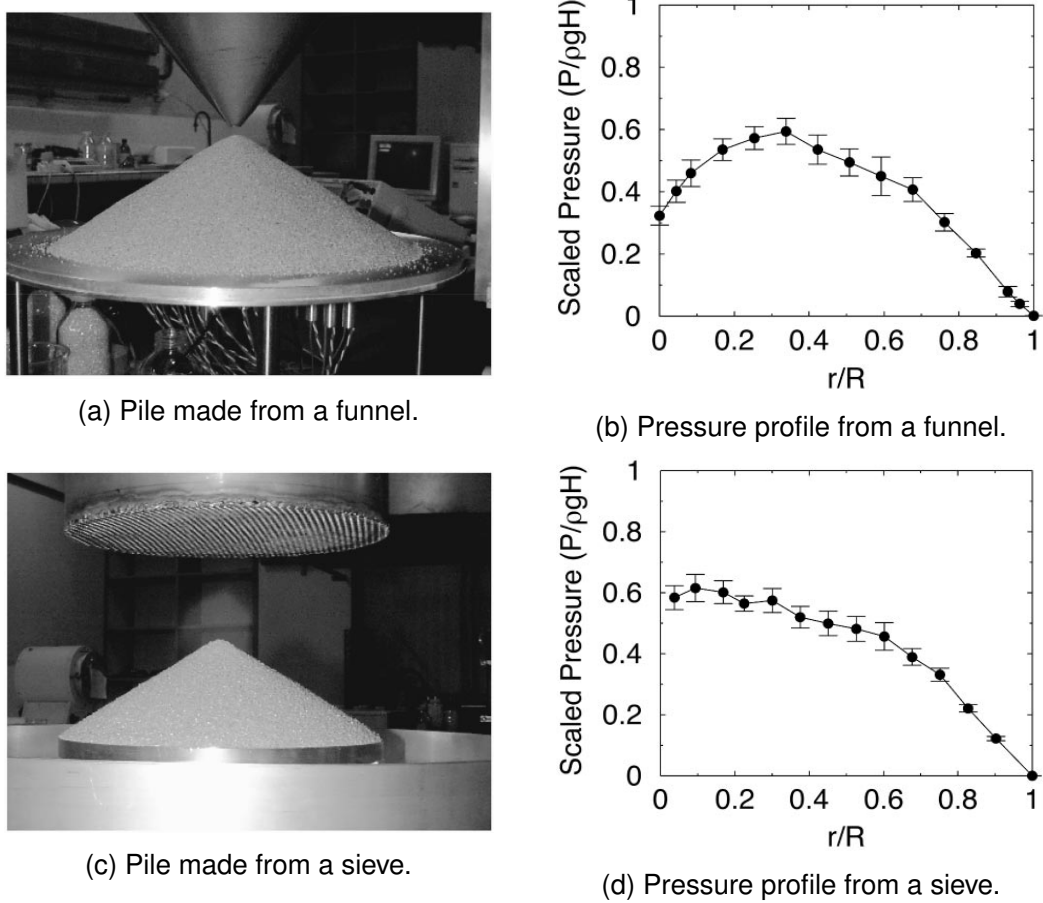


Figure 7 – The preparation of the sand piles reflects on the pressures measured at the bottom of the pile. In the Panels 7a and 7b the deposition from the funnel creates a pressure profile that peaks outside the center of the pile, while in the Panels 7c and 7d the deposition from the sieve creates a pressure profile that has a plateau and decays on the edges. Figures taken from [33].

the table radius r/R , while in the table deposition made from the sieve presents pressure as a kind of plateau between the center of the table and 0.25 of the radius r/R , with the maximum close to the center.

A study by Atman *et al.* [37] shows that different preparation histories of granular materials result in different response functions. As an example, Figure 8 shows two different responses, comparing different geometries of grains: circular and pentagonal. This means that when a localized force is applied over a granular assembly composed by organized assemblies, like the circular grains configuration shown in Panel 8a, the distribution caused by this force, spreads concentrated in two diagonals; while the localized force is applied over a disordered granular assembly, like this pentagonal grains configuration shown in Panel 8b, the distribution caused by this force, spreads more uniformly and deeper than the case applied to organized assembly. The response function of this example is the measurement of the stress after applying the load subtracted from the same preparation before applying the load.

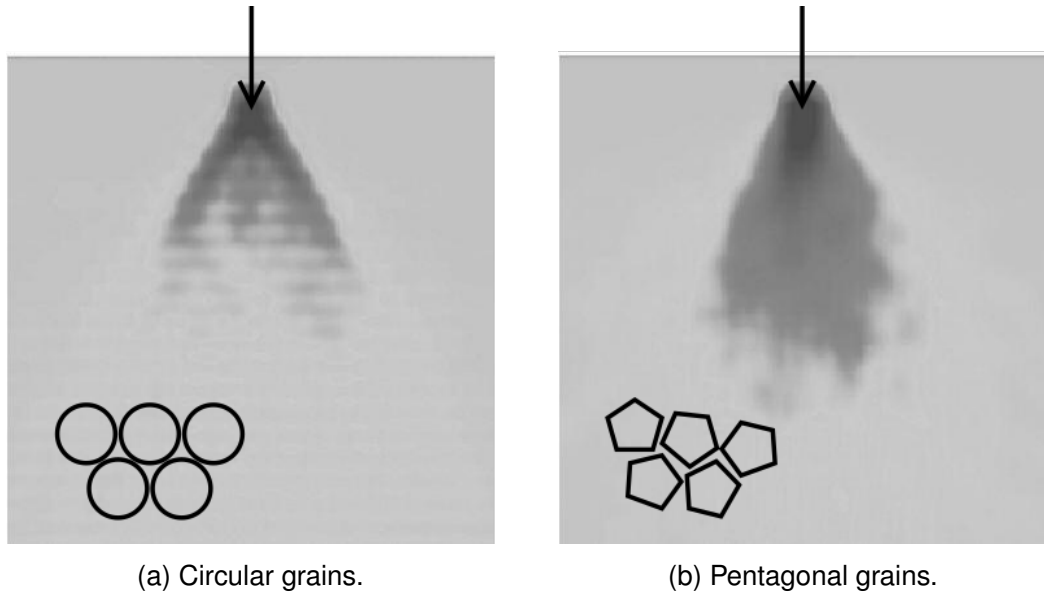


Figure 8 – Different granular systems exhibit different response functions. The main difference between these systems is that Panel 8a has higher organization and circular grains, while Panel 8b has higher disorder and pentagonal grains. Figures taken from [37].

Response function is the response of a system based on different times of the same system, when an input is applied on this different times, then the difference of the states results in the response of this input [3].

One rich property that many researches studied [14, 38, 44, 45, 46] is the jamming effect. Jamming or clogging, is the effect that dense granular materials suffer when a load is applied and these grains do not move. The consequence is that arch may form to hold the material, as in figure 6, but also a cavity may appear if an object is dragged from the inside, like figure 9.

Looking at the scales of granular materials, five separated scales are modeled, according to Radjai *et al.* [48], as shown in Figure 10. From now on, when referred to micro-scale, we are talking about dynamics or measures that accounts the effects on contacts or in particles, like rheological models of grains and inter-particle forces. Meso-scale are the structure of packing, like chain forces, local packing fraction and coordination number. Coordination number is the number of grains in contact with one single grain. Macroscale is related to the effects on the material and the process, like the stress tensor of the agglomerate and the continuum description of granular materials [48].

When a wet confined granular material is under pressure, one can see that the liquid shrinks into the material. This phenomena may be contra-intuitive, since when a liquid is squeezed, it is expelled from the container. If the liquid is mixed with granular material, like sand and sea water on a beach, when someone steps on the sand, the surface near the feet becomes dry. This effect was reported by Reynolds [49].

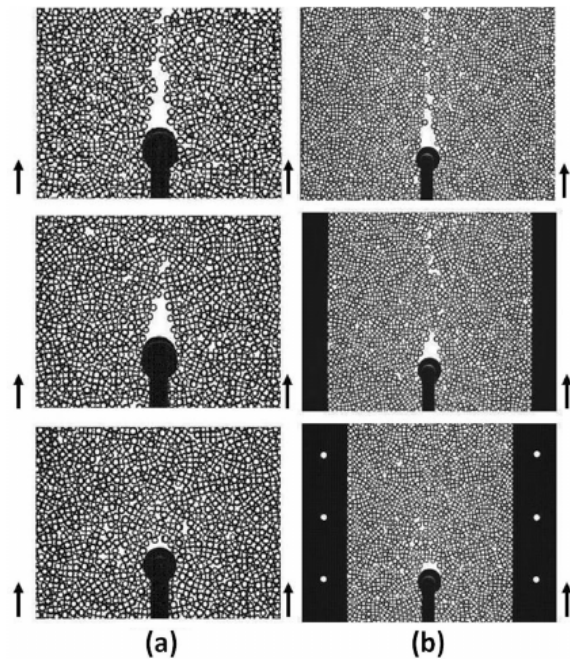


Figure 9 – The cavity behind the intruder varies according to the packing fraction. The packing fraction is increased in the left panels, from top to bottom as follows: $\phi = 0.8050$, $\phi = 0.8208$ and $\phi = 0.8262$, and they have width equals 13.475 times the intruder diameter. The right panels have packing fraction $\phi = 0.8035$ and widths, from top to bottom, equals 10.9, 8.5 and 6.9 times the intruder diameter. Figure taken from [47].

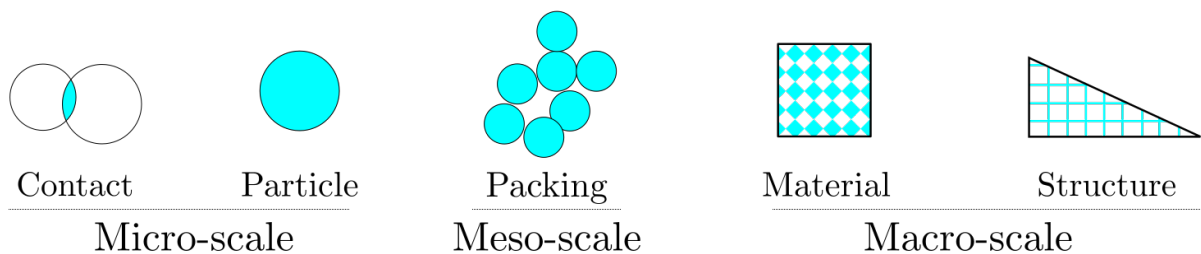


Figure 10 – Scales present in granular measures and effects. The smaller ones are in the contact scale, like contact forces while the higher ones are in landscape scale, like mountains and tectonic formation. Figure adapted from [48].

In the next chapter, we will describe the equations and procedures to carry out simulations of granular materials, taking account the contact model to simulate dry granular systems.

3 Discrete Element Method - DEM

Numerical simulations are widely used to study granular systems, which play an important role in complementing experimental information, which further enhances the understanding of granular physics phenomena. A justification to the use of numerical simulations is the precise control of the input parameters of the simulations and the level of complexity about the object of study. Another advantage is the ease extraction of data, from the grain scale, such as force chains, up to the system scale, such as material shear, showing possible emerging properties and their causes.

The technique to simulate of granular materials that we use in this work is a DEM known in the literature as Molecular Dynamics (MD). The method consists of numerically solving the Newton's laws of motion. An advantage of this method is that any force that can describe the interaction with the elements is accepted in this method.

The technique described in the reference [10] uses the formalisms of analytical mechanics through the interaction potentials between agents, whether Lagrangian or Hamiltonian potentials, to establish the forces acting on each agent. The disadvantage of this type of description is that dissipative forces may not appear, since the description of forces is directly related to potentials. Formally, the system must obey the set of Equations described by the Lagrangian function of the system:

$$\mathcal{L} = \mathcal{T} - \mathcal{V}, \quad (2a)$$

$$\sum_k \left[\frac{d}{dt} \left(\frac{\partial \mathcal{L}}{\partial \dot{q}_k} \right) - \left(\frac{\partial \mathcal{L}}{\partial q_k} \right) \right] = 0, \quad (2b)$$

$$\vec{F}_i = \nabla \mathcal{L} = -\nabla \mathcal{V}, \quad (2c)$$

where \mathcal{L} represents the Lagrangian function that governs the dynamics of the system, \mathcal{T} the kinetic energy, \mathcal{V} the potential energy, k the number of generalized coordinates of the system, q_k the generalized coordinates, \dot{q}_k the generalized velocities, \vec{F}_i the force exerted on the particle i originated by the gradient of the potential \mathcal{V} .

Other references [50, 6, 14, 23, 38, 40, 41, 42, 51, 52, 53, 54, 55] use the model directly from the acting forces about each element.

3.1 Equations of motion

To carry out the simulation, the set of Equations 3 must be satisfied, which takes into account Newton's laws of motion. Thus, there is information on the agents' states as a

function of time.

$$Translational \begin{cases} \vec{r}_i(t) = \vec{r}_i(0) + \int_0^t \vec{v}_i(t) dt, \\ \vec{v}_i(t) = \vec{v}_i(0) + \int_0^t \vec{a}_i(t) dt, \\ \vec{a}_i(t) = \sum_j \frac{\vec{F}_{i,j}(t)}{m_i}, \end{cases} \quad (3a)$$

$$Rotational \begin{cases} \theta_i^k(t) = \theta_i^k(0) + \int_0^t \vec{\omega}_i^k(t) dt, \\ \vec{\omega}_i^k(t) = \vec{\omega}_i^k(0) + \int_0^t \vec{a}_i^k(t) dt, \\ \vec{a}_i^k(t) = I_i^{k-1} \sum_j \vec{\tau}_{i,j}^k(t), \end{cases} \quad (3d)$$

$$(3e) \quad (3f)$$

where i is the i -th particle of the system, $\vec{r}_i(t)$ is the position vector of the center of mass of the body i at the instant of time t , $\vec{v}_i(t)$ or $\vec{r}_i(t)$ is the velocity vector of the center of mass of the body, $\vec{a}_i(t)$ or $\vec{v}_i(t)$ or $\vec{r}_i(t)$ is the vector of accelerations of the center of mass of the body, $\vec{F}_{i,j}(t)$ is the component of the force that the center of mass of the body suffers from interacting with another body or field j , m_i is the body mass, $\theta_i^k(t)$ is the basis of the body rotation coordinates expressed in the system's k basis, $\vec{\omega}_i^k(t)$ is the pseudovector of angular velocities of the body expressed on the basis k of the system, $\vec{a}_i^k(t)$ is the pseudovector of angular accelerations of the body, I_i^{k-1} is the inverse of the inertia tensor of the body and $\vec{\tau}_{i,j}^k(t)$ is the torque vector that the body suffers from interacting with another body or field. Remembering that the relationship between torque and the force that causes it can be described by the Equation 4:

$$\vec{\tau}_{i,j}(t) = \vec{\chi}_{i,j}(t) \times \vec{F}_{i,j}(t), \quad (4)$$

where the vector $\vec{\tau}_{i,j}(t)$ is the cross product of the vector $\vec{\chi}_{i,j}(t)$, which connects the center of mass of the particle i to the point of application of the force, and the vector $\vec{F}_{i,j}(t)$, the vector of the force caused by interacting with another body or field j . The Equations 3c and 3f express Newton's second law.

The formulation described by the set of Equations 3 covers spaces in 1D, 2D and 3D, but this thesis focuses only on the formulation of 2D systems.

3.1.1 Force model

The forces present in the systems modeled in this Chapter include the contact forces between agents, which belong to the rheological model of grains and the gravitational force. The interaction forces between grain and fluid is described in Chapter 6.

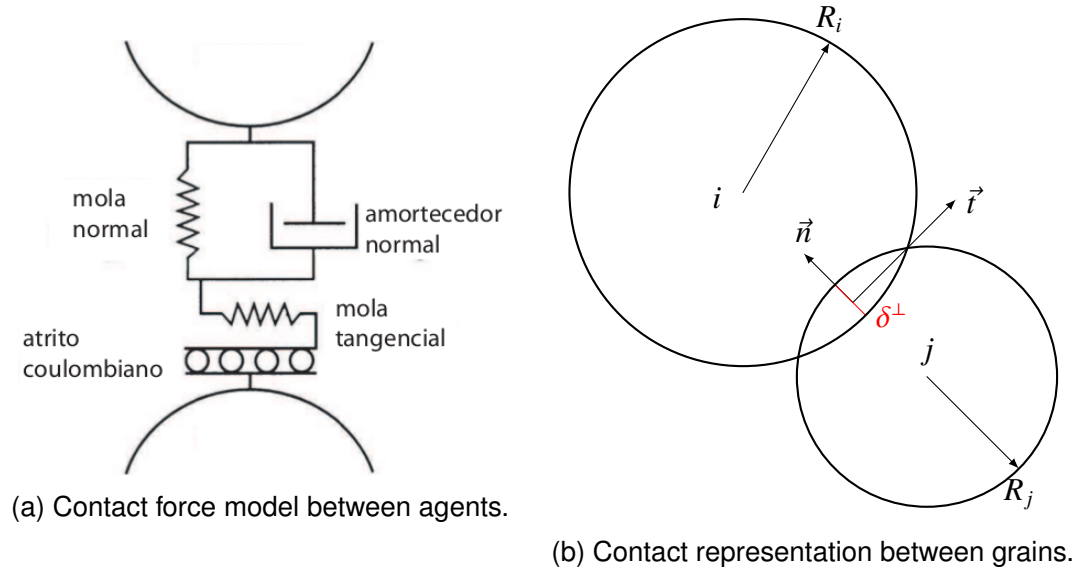


Figure 11 – Force model and representation between two circular grains. Figures taken from [50].

3.1.1.1 Rheological model of grains

The rheological model of the contact between grains we used to simulate granular materials was the rheological model proposed by Kelvin-Voigt [56, 57]. Kelvin-Voigt rheology models the contact force between two grains by a spring and a damper in parallel in the normal direction of contact, as exemplified in Figure 11. The spring portion represents the elastic contribution of the material, related to the Young's modulus, while the damper has the function of dissipate the energy in the inelastic collision between the grains. Additionally, a spring-like element is inserted in the tangential direction. A model proposed in [14] adds a damper-like element in parallel to the tangential spring, modeling the rolling resistance. We chose to use circular geometry for the grains. Because of the circular geometry, all angular momentum variation is caused by torque due to tangential force.

A peculiarity of DEM is that it allows interpenetration between the grains. Therefore, in this model there is no deformation in the contact between two bodies. The maximum interpenetration we allow in our model is controlled by the material's hardness parameter and we impose a maximum penetration of 0.5% of the radius.

To determine the value of the interpenetration, δ , in circular geometry, the Equation 5:

$$\delta_{i,j}^{\perp} = (R_i + R_j - |\vec{r}_j - \vec{r}_i|) \mathcal{H}(R_i + R_j - |\vec{r}_j - \vec{r}_i|), \quad (5)$$

where $\delta_{i,j}^{\perp}$ is the value of the interpenetration between the grains i and j , R_i is the radius of the body i , R_j is the radius of the body j , \vec{r}_i is the position vector of the center of the body i , \vec{r}_j is the position vector of the center of the body j and \mathcal{H} is the Heaviside step function. So, when the distance between the bodies is greater than the sum of the radii, the bodies will not be in contact and the Heaviside step function indicates that the interpenetration

between the grains is null. If the distance between the bodies is lesser than the sum of the radii, the bodies will be in contact and the Heaviside step function indicates that there is interpenetration between grains, by its value being equals to one.

With grains being in contact, the direct consequence of the interpenetration is the appearance of an elastic repulsive force, and the force depends on the interpenetration function δ^\perp . The force expression can be calculated by the Equation 6:

$$\vec{F}_{i,j}^{el} = -k_n (\delta_{i,j}^\perp)^{\frac{D}{2}} \hat{n}_{i,j}, \quad (6)$$

where $\vec{F}_{i,j}^{el}$ is the elastic force that the body j causes to the body i when they come in contact, k_n is the constant related to the elasticity of the material in the direction of contact, $\delta_{i,j}^\perp$ is the interpenetration between the bodies i and j , D is the dimension of the system (in this case, $D = 2$) and $\hat{n}_{i,j}$ is the normal direction of the contact [50, 14, 58]. One can write a potential for this elastic force as: $\mathcal{V} = \frac{1}{2} k_n (\delta_{i,j}^\perp)^2$.

Associated with the elastic force, the damping force is also present. As it is a dissipative force, a potential cannot be associated with the damping force. Most of the energy loss of granular materials is in collision. The Equation 7 describes its behavior:

$$\vec{F}_{i,j}^{am} = -\gamma (\vec{v}_{i,j} \cdot \hat{n}_{i,j}) \hat{n}_{i,j}, \quad (7)$$

where $\vec{F}_{i,j}^{am}$ is the damping force that the body j causes to the body i when they come in contact, γ is the damping constant related to the inelastic collision, $\vec{v}_{i,j}$ is the relative velocity between the centers of mass of bodies i and j and $\hat{n}_{i,j}$ is the normal contact direction [50, 14, 55].

The damping constant is directly linked to the restitution coefficient and can be used equivalently through the transformation shown in the set of Equations 8. Some authors use the restitution coefficient in simulations, such as [23, 51, 55]. In this thesis we will use the damping constant.

$$\epsilon = \exp\left(\frac{-\pi}{\sqrt{\frac{4k_n m}{\gamma^2} - 1}}\right), \quad (8a)$$

$$\gamma = \sqrt{\frac{4k_n m}{\left(\frac{\pi}{\ln(\epsilon)}\right)^2 + 1}}, \quad (8b)$$

where ϵ is the restitution coefficient, γ is the damping constant, k_n is the constant related to the elasticity of the material in the direction of contact and m is the reduced mass $m = \frac{m_i m_j}{m_i + m_j}$.

The friction force is also present in the simulation model. As the surfaces are in contact, there will be a frictional force between them if they tend to move each other. In particular, due to the circular geometry, friction forces will only act in the tangential direction.

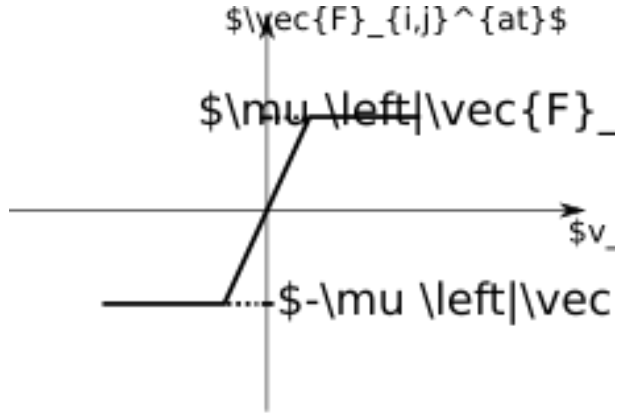


Figure 12 – Friction versus relative velocity between contact. Figure taken from [14].

The relative velocity between the contact point of the bodies is given by the Equation 9 below:

$$\delta_{i,j}^{\parallel} = \vec{v}_{ij} \cdot \hat{t}_{ij} - R_i \omega_i - R_j \omega_j, \quad (9)$$

where $\delta_{i,j}^{\parallel}$ is the relative velocity of the contact point of the bodies i and j , \vec{v}_{ij} is the relative velocity of the centers of mass of the bodies i and j , \hat{t}_{ij} is the tangential vector to the contact surfaces of the bodies i and j , R_i is the radius of the body i , R_j is the radius of the body j , ω_i is the angular velocity of the body i and ω_j is the angular velocity of the body j .

For the tangential force, it is necessary to know the relative displacement of the contact point, as given by the equation 9, applied in the system of Equations 10, which models the friction force with saturation, and is given by:

$$\vec{F}_{i,j}^{at} = \begin{cases} - \int_{t_0}^{t_f} k_t \delta_{i,j}^{\parallel} \hat{t}_{ij} dt, & \text{if } k_t |\delta_{i,j}^{\parallel}| \leq \mu |\vec{F}_{i,j}^n| \quad (\text{Static friction}) \\ - \frac{\delta_{i,j}^{\parallel}}{|\delta_{i,j}^{\parallel}|} \mu |\vec{F}_{i,j}^n| \hat{t}_{ij} & \text{if } k_t |\delta_{i,j}^{\parallel}| > \mu |\vec{F}_{i,j}^n| \quad (\text{Kinetic friction}) \end{cases}, \quad (10)$$

where $\vec{F}_{i,j}^{at}$ is the friction force between the bodies i and j , k_t is the elastic constant of the material in the tangential direction, $\delta_{i,j}^{\parallel}$ is the relative velocity between the contact point of the bodies i and j , \hat{t}_{ij} is the tangential vector to contact surfaces of bodies i and j , μ is the friction coefficient between the surfaces of bodies i and j and $\vec{F}_{i,j}^n = \vec{F}_{i,j}^{el} + \vec{F}_{i,j}^{am}$ is the force normal to the surfaces of bodies i and j .

We chose to model static and dynamic friction to be a single value for simplicity, presented the friction coefficient μ . Figure 12 describe the Coulomb friction we are using in the simulations.

3.1.1.2 The external force: Gravity

For this model, the gravitational influence is approximated by a constant, since the simulation does not take into account that the influence of the bodies' mass is very small, if

compared to the mass of the planet where the simulation is located, as well as the variation of height of the simulated system is very small and is close to the surface of the planet when compared to the radius of the planet. For convenience, we normalize gravity as a unit value.

3.1.2 Temporal discretization

For the computational simulation of solid bodies, the kinematics equations must be rewritten as Taylor series expansions, and we chose the interpolating the velocity equation system by the algorithm known as Velocity Verlet [59, 10]. The equations of motion discretized in time, as a function of the time step Δt , become as in the set of equations 11:

$$\vec{r}_i^{n+1} = \vec{r}_i^n + \vec{v}_i^n \Delta t + \frac{\vec{a}_i^n}{2} (\Delta t)^2, \quad (11a)$$

$$Translacional \left\{ \begin{array}{l} \vec{v}_i^{n+1} = \vec{v}_i^n + \frac{\vec{a}_i^n + \vec{a}_i^{n+1}}{2} \Delta t, \\ \vec{a}_i^{n+1} = \frac{\sum_j \vec{F}_{i,j}^{n+1} + \sum \vec{F}_{i,ext}^{n+1}}{m_i}, \end{array} \right. \quad (11b)$$

$$(11c)$$

$$\theta_i^{n+1} = \theta_i^n + \vec{\omega}_i^n \Delta t + \frac{\vec{\alpha}_i^n}{2} (\Delta t)^2, \quad (11d)$$

$$Rotacional \left\{ \begin{array}{l} \vec{\omega}_i^{n+1} = \vec{\omega}_i^n + \frac{\vec{\alpha}_i^n + \vec{\alpha}_i^{n+1}}{2} \Delta t, \\ \vec{\alpha}_i^{n+1} = I_i^{-1} \sum_j \vec{\tau}_{i,j}^n, \end{array} \right. \quad (11e) \quad (11f)$$

where i is the index of the moving body, j is the index of the body in contact with the body i , n is the time step, \vec{r} is the position of the body, \vec{v} is the velocity of the body, \vec{a} is the acceleration of the body, Δt is the size of the time step, $\vec{F}_{i,j}$ is the contact force between the bodies i and j , \vec{F}_{ext} are the external forces, such as gravity, m is the mass of the body, θ is the angular position of the body, $\vec{\omega}$ is the angular velocity of the body, $\vec{\alpha}$ is the angular acceleration of the body, $\vec{\tau}$ is the torque on the body, I is the moment of inertia of the body.

The set of Equations 11 is written for the 2D system, since there is only one degree of freedom for the rotation, and consequently all equations are written as a function of a single parameter. The velocity approximation as the weighting between the accelerations in the current and future instants of time is the key to the minimization of the imprecision generated by the discretization [10].

3.2 Algorithm

In addition to the equations that govern the system, a series of procedures must be carried out so that the simulation can take place. Each of these steps are essential for the simulation to take place, and are dependent on each other. The Algorithm 1 determines the

routines for executing the simulation. We use the 3rd order Gear Predictor-Corrector with the Velocity Verlet to perform the simulations [10].

Algorithm 1: Given the input of the problem, such as initial positions of bodies, velocities and accelerations, the algorithm assembles a list of bodies that are neighbors delimited by a certain region, then predicts the position and velocity of the bodies at the next instant of time, looks for the contacts that were formed with the prediction, calculates the forces between each body in contact and includes the external forces, and corrects the velocity and acceleration predictions for each body. Thus a DEM step is constructed. Algorithm taken from [50].

```

Input :initial simulation data setup
Output :response and simulation measurements over time
while not reached the stop condition of the simulation do
    if it is time to List the Neighbors then
        | List the Neighbors;
    end
    Predictor;
    Detect Contacts;
    Force Calculation;
    Corrector;
end
```

The algorithm stopping conditions depend on the purpose of the simulation. Some examples, such as static pile stability, energy fluctuations, breaking of force chains, average system velocity, number of time steps, among several other measurable parameters within the simulation can become the stopping criteria of the simulation. In this thesis, we use the number of simulation time steps as the main stopping criterion.

We will briefly discuss each of the routines Algorithm 1. For more details, the references [50, 10, 55] have further explanations about the routines, with examples and detailed algorithms.

3.2.1 Neighbors

Although not the simplest form of the Neighbor-Finding algorithm, it is the most efficient, and is described in [50]. It consists of creating a list of all bodies that belong to a certain region of possible interaction. Creating the list minimizes the number of comparisons during execution, which provides the highest computational performance. The article "Methods of parallel computation applied on granular simulations"[60] reveals the differences between some methods of creating lists of interacting bodies. This article was written during the preparation of this thesis project and is in the Appendix A. The Algorithm 2 refers to the creation of a list of bodies that have the possibility of interacting with each other.

Algorithm 2: Algorithm for creating the list of neighbors. Algorithm taken from [50].

Input: body position

Output: neighbor list

Divide the space in regions;

foreach body **do**

Insert the body in the list of the region it belongs to;

Insert the body into adjacent lists of the region it belongs to;

end

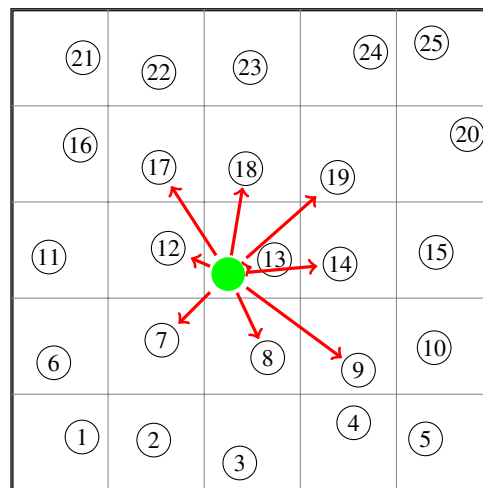


Figure 13 – The neighbour search in Algorithm 2 occurs between bodies with their immediate adjacent neighborhood region. Figure taken from [50].

The figure 13 shows the regions that the marked body should be listed. For more details, see the references [50, 10].

3.2.2 Predictor

The prediction routine updates the positions and velocities of the bodies, allowing all forces to be calculated based on the new values. In the set of Equations 11, equations involving terms with index n are updated in this routine. The 3 algorithm shows the structure of the prediction routine.

Algorithm 3: Prediction routine for state variables of bodies. Algorithm taken from [50].

Input :positions, velocities, accelerations and the time step Δt

Output :positions, part of the velocities

forall bodies **do**

Calculate new postions;

Predict new velocities;

end

3.2.3 Detect contacts

The contact detection routine uses the list of neighbors generated by the Algorithm 2 to check whether the listed body/neighbor pair has interpenetration, described in equation 5, and then generates a new list of bodies that interpenetrate each other to be used in the Algorithm 5. The Algorithm 4 describes this operation.

Algorithm 4: Detect contacts routine. Algorithm taken from [50].

```

Input : Neighbor list
Output : Contact list
forall neighbor bodies do
    | Calculate the Interpenetration  $\delta_{i,j}$  between bodies  $i$  and  $j$ ;
    | if  $\delta_{i,j} > 0$  then
    |   | Insert the pair  $i$  and  $j$  in the contact list;
    | end
end
```

3.2.4 Force calculation

The routine to calculate the forces uses the contact list generated by the Algorithm 4 to calculate the contact forces between the bodies, such as elastic forces (Equation 6), damping forces (Equation 7) and friction forces (Equation 10). In addition to contact forces, bodies are subjected to gravitational force. The Algorithm 5 contains the execution of the calculation of the forces.

3.2.5 Corrector

The correction routine updates the speeds and accelerations of the bodies. The forces calculated in the force calculation are used here to perform the Velocity Verlet and determine the velocities and accelerations for the next time step. In the set of Equations 11, the equations involving terms with index $n + 1$ are updated in this routine. The Algorithm 6 shows the structure of the correction routine.

3.3 Important parameters

Due to the presented force model, some parameters are important for the simulations. As they are governed by difference equations as a function of the temporal parameter, some criteria must be obeyed for the simulation to be stable. One of the parameters is the time constant Δt , which in our simulations has a direct relationship with the oscillation period of the spring mass model (Kelvin-Voigt rheology), given by $\Delta t = \zeta \sqrt{m_{min}/k_n}$, where ζ is an adjustment value, m_{min} is the smallest mass of the system, and k_n is the spring constant. The

Algorithm 5: In this routine, the resultant forces are calculated for each body. The force \vec{N} is the normal force, contribution of the elastic force \vec{F}^{el} and the damping force \vec{F}^{dam} (Equations 6 and 7), F^d is the rolling force of one body on the other, which must be compared with the maximum static friction force μN . Algorithm taken from [50].

```

Input :positions, velocities and contact list
Output :acting forces and torques in the bodies
foreach body do
    Apply gravity force;
    foreach body in the contact list do
        Calculate the normal forces  $\vec{N}$ ;
        Calculate the rolling forces  $F^d$ ;
        if  $|F^d| < \mu|\vec{N}|$  then
             $\vec{F}^{at+} = \vec{F}^d\hat{t}$ ;
        else
             $\vec{F}^{at+} = \mu\text{sign}(\vec{F}^d)N\hat{t}$ ;
        end
        Calculate torque;
    end
end

```

Algorithm 6: Correction routine for state variables of bodies. Algorithm taken from [50].

```

Input :acting forces and torques in the bodies and the time step  $\Delta t$ 
Output :positions, velocities and accelerations to the next time step
foreach body do
    Calculate accelerations;
    Correct velocities;
end

```

factors that stabilize the simulations, they must have $\zeta < 1/10$ [50, 14, 10]. In this thesis we will use the factor of 1/10 for non-vibrated systems and 1/100 for vibrated systems.

Another important parameter is the damping factor γ , or the restitution coefficient ϵ . Due to the dissipative nature of granular materials, $\epsilon \approx 0$, which approximates $\gamma \approx 2\sqrt{k_n m_{min}}$, because we will have critical regimes in the spring mass equation when we use the smallest mass of the two bodies, and for all others, the damping will be subcritical [53, 51].

We model the walls for the BNE problem as smooth walls. The technique we use is to create a virtual body that has only the fixed component that it does a boundary, while it is free to move in the other direction, coinciding to be in the closest position of the free bodies.

In the next chapter we will describe the Brazil nut Effect (BNE) and how we set up the simulation that leads to this effect.

4 Brazil Nut Effect (BNE)

Historically, the phenomenon known as BNE was identified in Brazil nut exports, which were taken in containers on ships leaving Brazil, and whenever they arrived at their destination, it was observed that the largest nuts were at the top. Initially it was thought that Brazilian traders arranged the nuts so that the largest were on top and the smaller and broken ones at the bottom. After investigation, it was verified that the larger nuts rise due to the vibration that the containers suffered during transport [14].

The BNE occurs when grains of different sizes segregate, causing larger grains segregate from smaller ones. The segregation effect can be seen when a system is shaken, or a shear cycle is imposed [4]. This phenomenon is associated with the granular phase of the system. In a solid-like granular system, the larger grain is static. With agitation, the system changes to a liquid state, allowing the movement of grains in the system [61]. The movement of the material occurs in convection currents that form close to the walls, or with the ratchet effect [62, 63, 64, 65], both cases allow small grains fill the space previously occupied by the larger grain, rising the larger grain. Figure 18 shows the evolution of the convection currents in a confined media. Once smaller grains collectively move to fill the void left by larger grains, smaller grains impede their downward motion; these correlations are at the basis of the observed size segregation. The ratchet effect is the granular solid-like behavior in below larger grains and the granular liquid-like behavior, where larger grains can move. The ratchet effect is also related to the Reynolds dilatancy, since the stress increases and the granular configuration changes.

One of the firsts attempts to explain the BNE was made by Rosato *et al.* [61] using Monte Carlo simulations and inspired many works to classify the roles of the parameters. As an example of the larger grain rising with respect to time, Figure 15.

The most important number used in the BNE studies is the dimensionless accele-



Figure 14 – Evolution of the vibrated bed. Top Panels are without intruder, while bottom Panels are with an intruder. Black and yellow layers are made of mustard grains. Figure taken from [63].

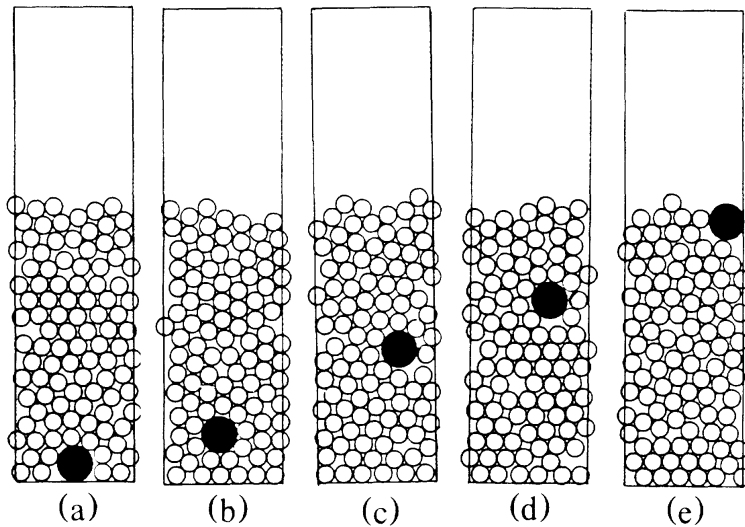


Figure 15 – Temporal evolution of shaken system of particles with periodic boundary conditions using Monte Carlo simulation. Initial configuration in Panel (a) and equally time spaced from Panels (a) to (e). Figure taken from [61].

ration, shown in the equation 12. The dimensionless number is a comparison between the maximum amplitude of the vibrational acceleration and gravity.

$$\Gamma = \frac{A\omega^2}{g}, \quad (12)$$

where Γ a dimensionless number that compares shaken acceleration with gravity, A is the system amplitude of the vibration, ω is the frequency of vibration, and g is the value of gravity. When $\Gamma > 1$, then the intruder can rise, since the ascending part of the oscillation rises the magnitude of the chain forces in the media, but when the system is descending the lighter grains occupies the void space left by the bead, causing the ratchet effect. If $\Gamma < 1$, then the intruder is not able to move, since chain forces stays there. This is the basic explanation, but not all cases work like it, as we see in some of our simulations, in Chapter 5.

An experimental problem is proposed in [64], like we study in Chapter 5. In their experiment a metallic bead is placed at bottom and then agitated. They use a cylinder silo and spherical grains with size ratio between intruder and media of 3, and Γ varies from 2.6 to 3.4, which leads the bead to rise over the media. There is a collapse of the curves involving the intruder position, the amplitude of the vibration A and the oscillation period ω like in figure 16. What we could find in our simulations is that frictionless walls also cause the bead to rise through convection currents, and the ascent ratio is similar with and without friction on the walls, see Figure 27.

The BNE is also influenced by the fluid that surrounds the media. In some cases, the air is relevant in the convection currents, and then leading to segregation, while vacuum leads to mixing [66, 64]. A more viscous fluid than air, like water, changes the regime of ascension of the bead, and the main mechanism that explains it is not the drag it self but the

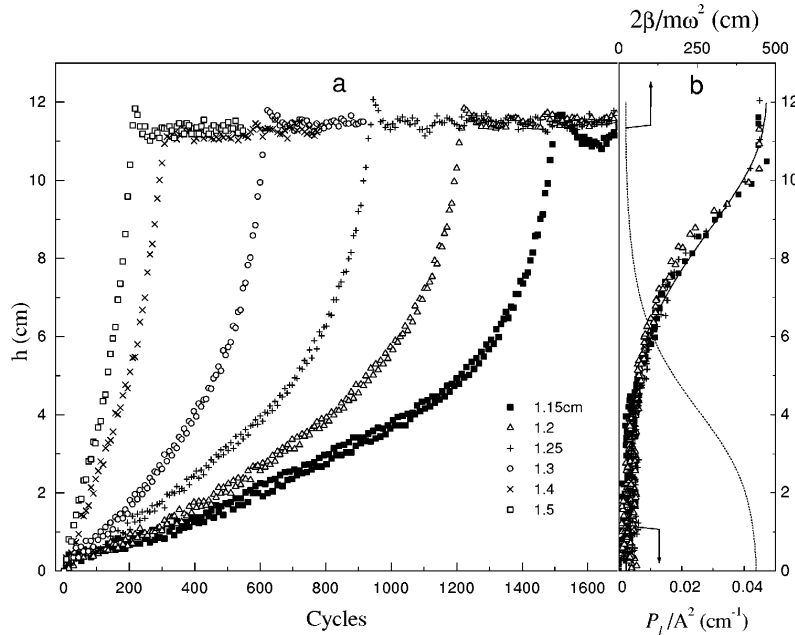


Figure 16 – Evolution of the bead in an agitated media within a cylinder silo. Panel (a) shows the height of the intruder versus time, while Panel (b) shows the collapse of the curves. Figure taken from [64].

enhance of the ratcheting effect [65].

Several phase diagrams were observed for some of the BNE parameters. The two main variables usually analysed are the ratio of the diameters of grains and the ratio of densities of grains, as shown in Figure 17. Another BNE phase diagram proposed by [63] takes into account the dimensionless acceleration Γ and the vibration threshold velocity $v_c = A\omega$.

Another correlated phenomena to BNE is the Reverse BNE (RBNE), in which the bead instead of rises it sinks. Many works enhanced the characterization of BNE and RBNE, in theoretical field, experimental results and numerical simulations [67, 68, 69, 70, 71, 72, 73, 74, 75, 76]. Some of these diagrams are presented here in Figures 19, 21 and 20.

Recently the Reference [77] experimentally shows that in a mixture of irregular ellipsoidal shape firstly reorient vertically, but without changing significantly their height; secondly, the grains rise upwards, and while doing so, they still tend to stay vertically aligned; and finally, when the grains reach the top, they tend to realign horizontally on the surface.

If the intruder of the media has a non uniform distribution geometry, like a polar particle, inserted in a layer of circular grains, and when the media is agitated, the intruder starts to "self-propel" at the direction it is oriented [78]. This is another property that non uniform shaken granular exhibit, reorienting the position or "propelling-itself".

Next Chapter, we describe the results of our BNE simulations using the techniques presented in Chapter 3.

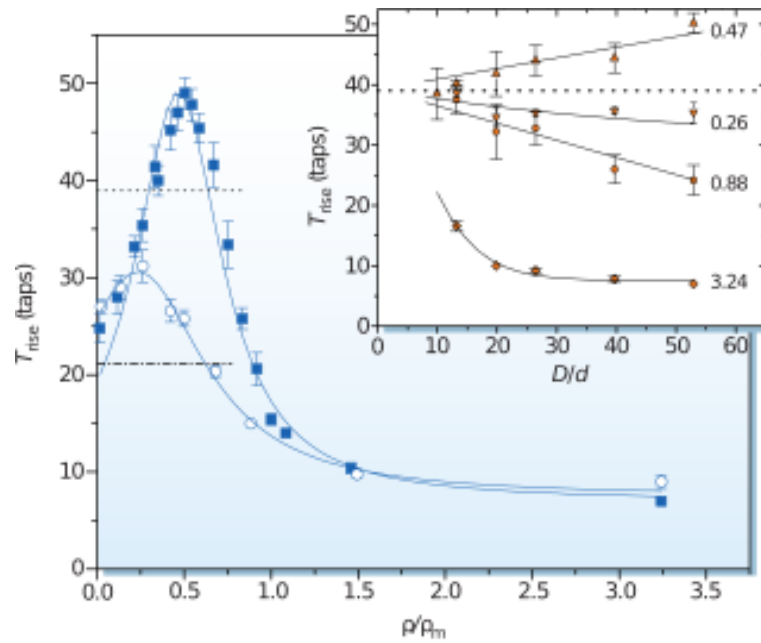


Figure 17 – BNE dependence on density and size ratio. The ascent time T_{rise} in the main Panel versus density rate, with size ratio of 5.08 between intruder and grains with different atmospheric pressures: 1 atm. in squares (■) and 90 torr in circles (○). The ascent time T_{rise} versus the size ratio for different density ratios: 0.44, 0.48, 0.88 and 3.1. Figure taken from [66].

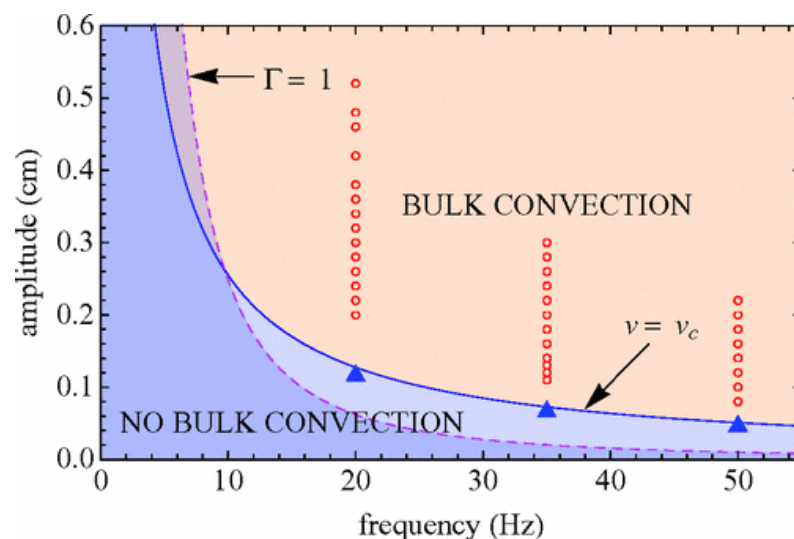


Figure 18 – BNE dependence on the dimensionless acceleration Γ and a critical velocity v_c . Values of $\Gamma < 1$ makes the intruder not rise, but also a $v < A\omega$. Figure taken from [63].

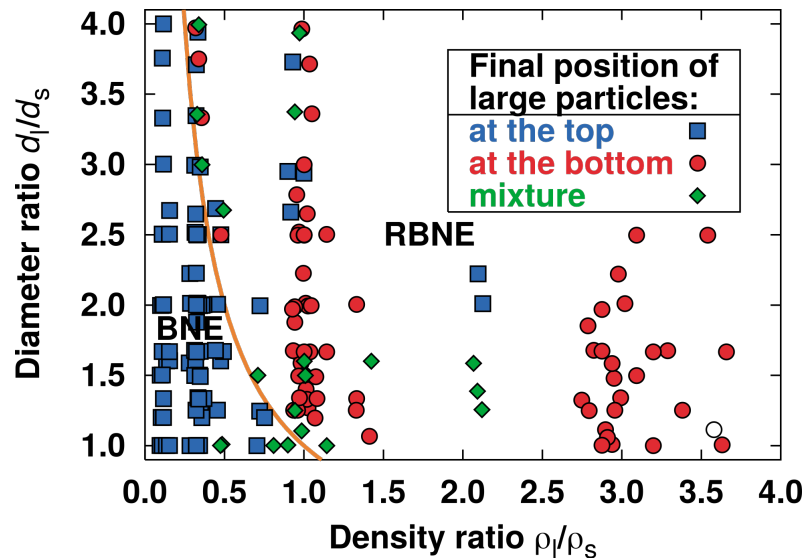


Figure 19 – BNE and RBNE dependence on the density ratio and the size ratio in vibrated base. The diagram shows the regime where beads rises in blue (■) causing the BNE, sinks in red (■) and is mixed in green (■). Figure taken from [73].

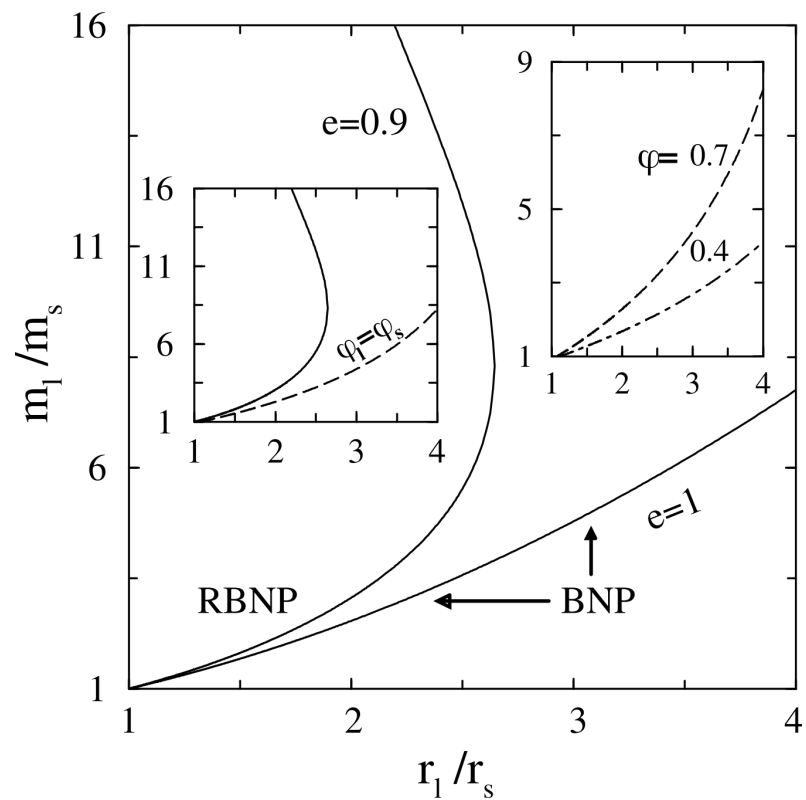


Figure 20 – BNE and RBNE dependence on the density ratio and the size ratio in vibrated base. The diagram shows the BNE-RBNE regime extracted from analytical equations of the forces in the system. e is the restitution coefficient, ϕ is the packing fraction, ϕ_l is the portion of the packing fraction related to the intruders, ϕ_s is the packing fraction of the other grains. Left inset: phase diagram with $e = 0.9$, $\phi_l/\phi_s = 10^{-8}$ (solid curve) and $\phi_l/\phi_s = 1$ (dashed curve). Right inset: phase diagram with $e = 0.9$, $\phi_l/\phi_s = 1$, $\phi = 0.7$ (dashed curve) and $\phi = 0.4$ (dot-dashed curve). Figure taken from [74].

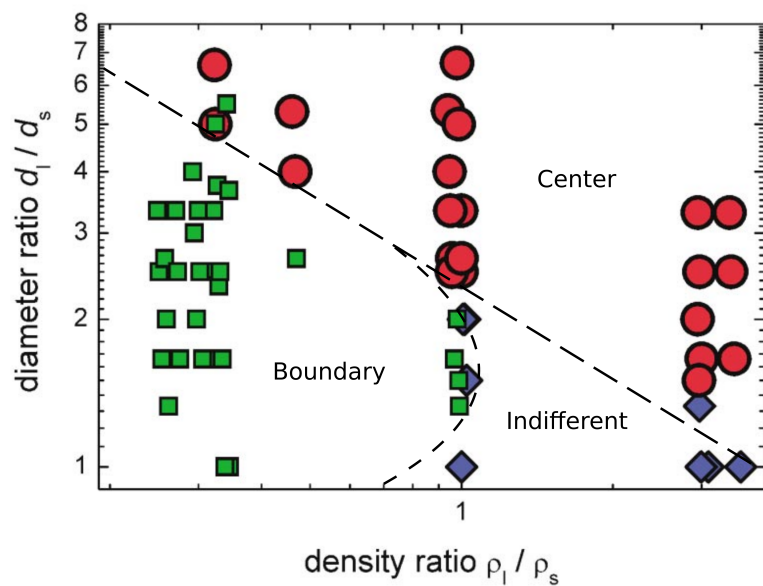


Figure 21 – BNE and RBNE dependence on the density ratio and the size ratio in swirling base. The diagram shows the regime where beads segregates in red (●), aggregates in green (■) and is indifferent in blue (◆). Figure taken from [67].

5 Result Analysis and Discussion - BNE

In this Chapter we will present the results obtained from BNE simulations. These results were published in Reference [79], also present in Appendix A.1. The parameters we used to simulate the system is 2500 grains, with average diameter $d = 1 \pm 2.5\%$, with uniform distribution, the intruder diameter $D = 2.5d$. Grains and intruder density $\rho = 4/\pi$, leading the average mass $m = 1$, the spring constant in the normal direction $k_n = 1000$ and the spring constant in the tangential direction $k_t = 750$, the critical damping coefficient $\gamma = 2\sqrt{m_r k_n}$, $m_r = \frac{m_i m_j}{m_i + m_j}$, the friction coefficient $\mu = 0.5$ between grain-grain contact, grain-intruder contact, grain-wall intruder contact and intruder-wall contact. The time step $dt = \frac{1}{100} \sqrt{\frac{m_r}{k_n}}$, the width $w = 37.5d$, the gravity acceleration $g = 1$. Any different parameter used is described properly in each corresponding Figure and in the text. As an example, Figure 22.

Initially, we studied the system with bottom and sidewalls, forming a box. In these simulations, we observed convection currents close to the walls. This convection currents are the main contribution to the rise of the intruder. The sequential position of the intruder in a single example is shown in Figure 23. The Figures 24, 25, 26, 27 and 29 show ascent profiles of the intruder.

We saw that denser intruders rise more slowly than less dense intruders for all Γ . For this frequency, we saw the contrary predicted in the BNE, the denser would rise faster than the less dense. This effect may be a peculiar behavior for this frequency, or the density range we test. We also notice that the convection current is stronger the less dense the intruder is. As expected, the higher the Γ the faster the ascent rate.

When frictionless walls (flw) are in play, we saw that convection decreases, causing a slower ascent rate, compared to fw. Figure 27 shows the intruder rise in a flw system, in opposition to the explanation in the Reference [64]. For flw, we saw that $\Gamma = 0.85$ was not able to rise, while fw rises with slow ascent rate.

When comparing the rise times of fw (figure 24) with flw (figure 27), we notice that the rise time is larger, and the system that has less agitation than gravity does not rise, showing that one of the factors that matter for the BNE are the convection currents formed close to the walls and the convection currents are enhanced by fw.

We define the ascent rate as the difference between the initial position of the intruder to its highest position, then divide this difference by the time it takes to rise. Then we plot the ascent rate versus shaken frequency for each Γ .

When no friction is present on the system, the intruder sinks to the bottom, inde-

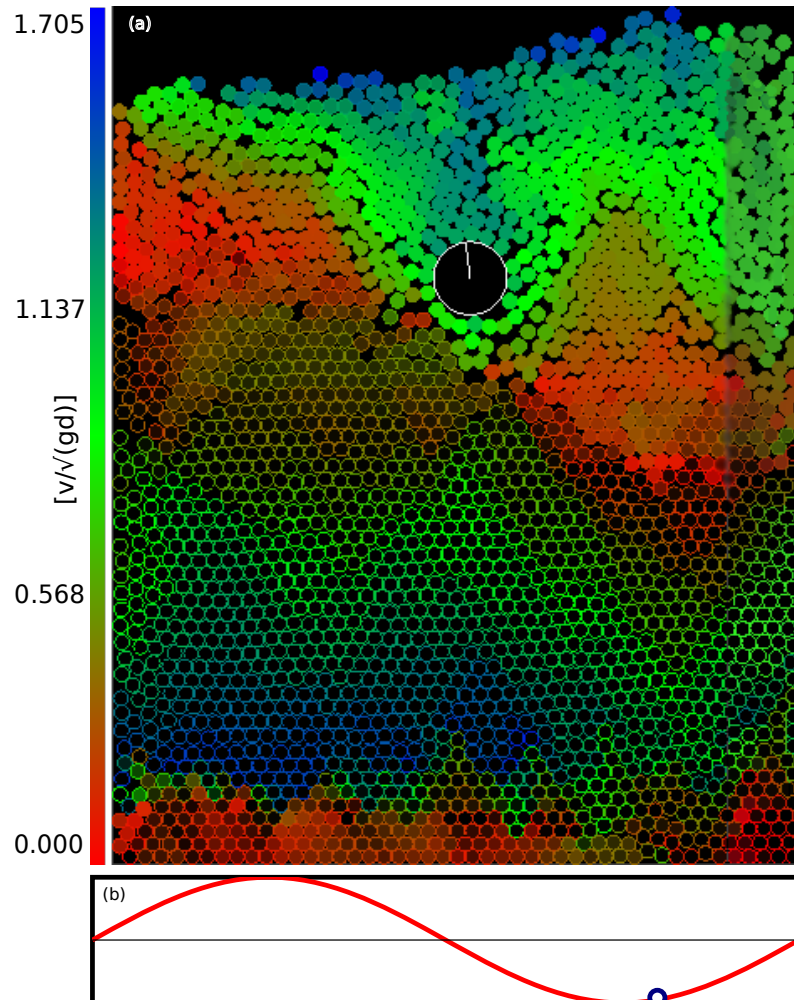


Figure 22 – In panel (a), a snapshot of the system lateral walls. Grains are represented by discs: hollow discs (\circ) are moving downward (with gravity) while filled ones (\bullet) are moving upward (against gravity). Color level shown at left side indicates the magnitude of the speed: red indicates no movement while blue indicates the maximum value for the speed. It is worth noting the inertia of the intruder accelerating the grains above him (bluish grains). It is also possible to observe the transition between the grains rising and falling in the reddish region around the intruder, a characteristic responsible for the granular ratchet effect. While the intruder easily displaces the grains on the way up, he is unable to move the grains that descend due to the steric exclusion. In panel (b) a sinusoidal displacement imposed to the substrate. This snapshot was taken after the minimum of the oscillation of the substrate, marked as a blue dot in this plot. Figure also present in [79].

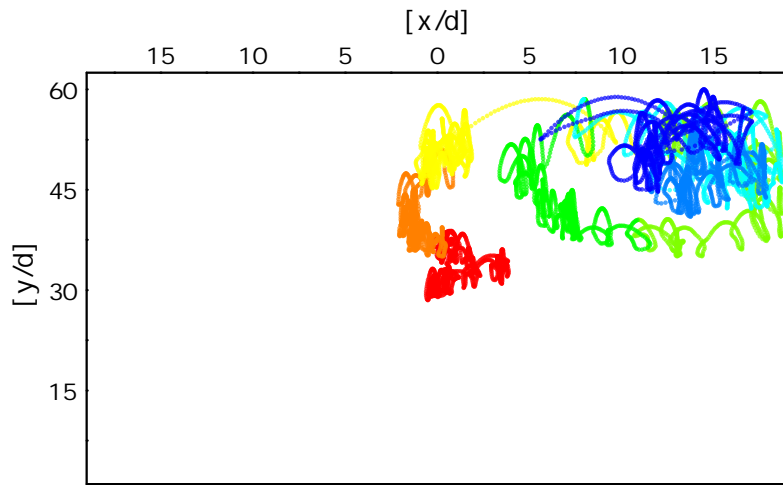


Figure 23 – Sequential positions of the intruder (x, y) taken at constant time intervals ($0.316 \sqrt{d/g}$), for a system with lateral frictional walls (fw). The shaken frequency $\omega = 0.256 \sqrt{d/g}$. $y = 0$ indicates the box floor and the unities are in unities of the mean grain diameter. The change in colors indicates the time elapsed in the simulation, the red corresponds to the beginning of the simulation and the blue to the end.

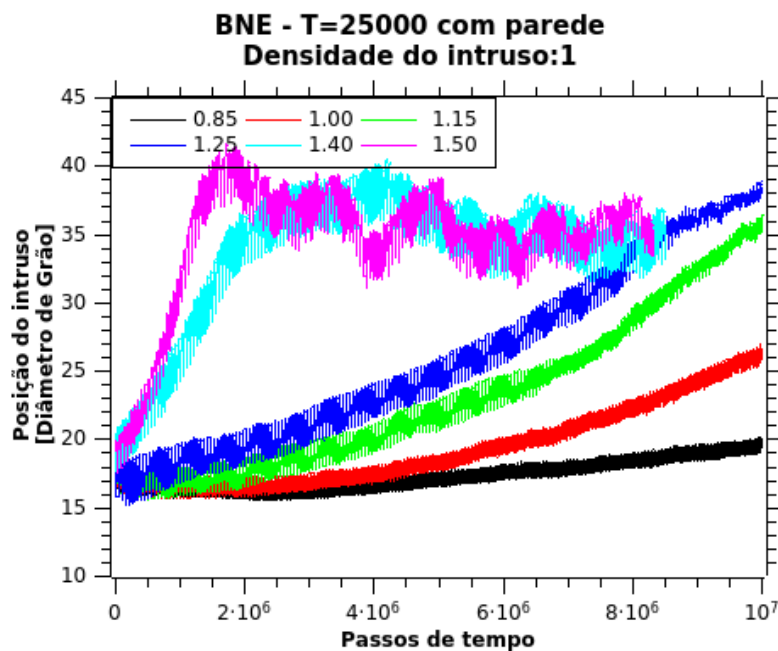


Figure 24 – Time series for intruder horizontal position at different Γ for system with frictional walls (fw). The density $\rho_I/\rho_g = 1$, with ρ_I the density of the intruder and ρ_g the density of the media. Simulations run until $\dots \sqrt{d/g}$. Figure also present in [79].

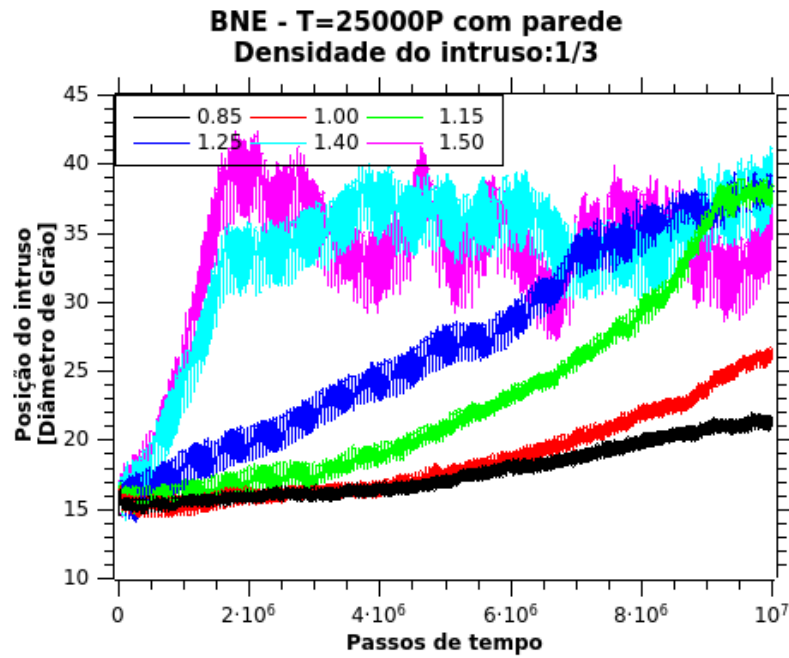


Figure 25 – Time series for intruder horizontal position at different Γ for system with frictional walls (fw). The density $\rho_I/\rho_g = 1/3$, with ρ_I the density of the intruder and ρ_g the density of the media. Simulations run until ... $\sqrt{d/g}$.

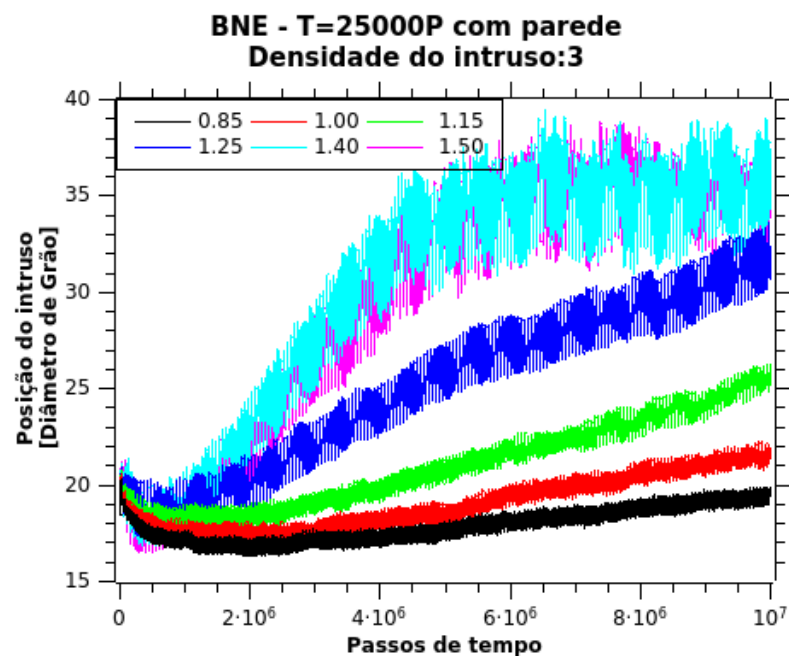


Figure 26 – Time series for intruder horizontal position at different Γ for system with frictional walls (fw). The density $\rho_I/\rho_g = 3$, with ρ_I the density of the intruder and ρ_g the density of the media. Simulations run until ... $\sqrt{d/g}$.

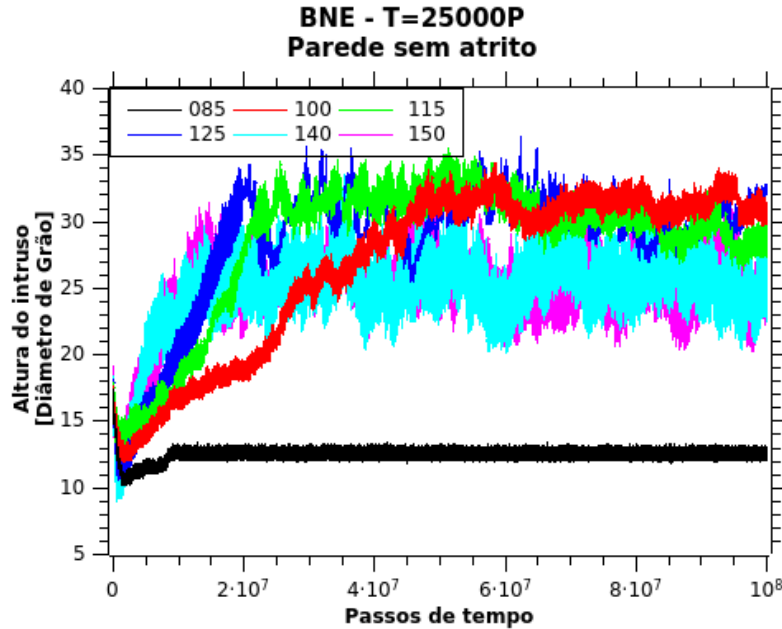


Figure 27 – Time series for intruder horizontal position at different Γ for system with fw. The density $\rho_I/\rho_g = 1$, with ρ_I the density of the intruder and ρ_g the density of the media.

pendently from the amplitude of the vibration. Figure 29 exhibits the height of the intruder in frictionless system. As expected, no friction on the system causes no BNE, and the simulations we have performed shows that the intruder sinks to bottom. We are not going to count this fact as a RBNE, since only friction has changed.

If instead of having sidewalls, we replace them with a periodic boundary condition (pbc), we could have the intruder crossing from one side to another, something impossible to do with walls, but also we expect to do not have the sidewalls effect, like convection currents. As an example of the intruder position through time, Figure 30. A difference between fw and pbc is the fact that the intruder can follow the convection current in fw and sink a little bit, while in pbc it does not sink in the media.

The as an example of pbc intruder ascent temporal profile, Figure 31. Two differences are present here, if we compare fw and pbc: the ascent time of the intruder for each Γ and the shaken frequency. At the same frequency applied to the fw, the pbc did not rise at all. The response is shown in Figure 32.

In Figure 31, we see that accelerations less than gravity do not cause the intruder to ascend, while accelerations close to gravity have a slow, jumping ascent. Because there are no sidewalls, convection currents do not form in the system, which causes the intruder to reach the top and not descend any further.

Figure 32 shows us that the ascent rate changes with the applied frequency, and as sudden the intruder ascent to the top, we propose that the behavior of the BNE in pbc could be modelled as a resonant system, since that dependency on ω is expected for a typical

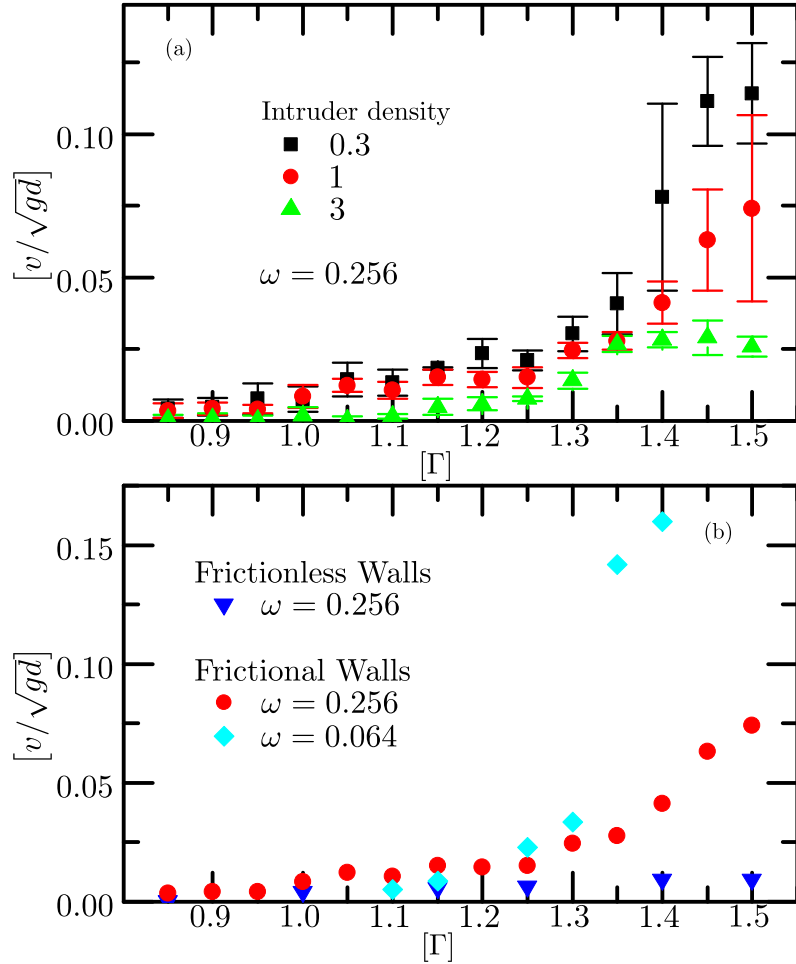


Figure 28 – In (a), the simulation was set to fw, width of $37.5d$, shaken frequency of $0.256\sqrt{g/d}$, 2500 grains, and we have varied the intruder density, compared to the medium. In (b), a comparison between fw and flw and a change in frequency. Figure also present in [79].

resonant system. Then, in analogy, the system behaves like a forced damped harmonic oscillator, with the response in the element that dissipates energy. The equation of a linear damped harmonic oscillator is:

$$\frac{d^2y}{dt^2} + 2\zeta\omega_0 \frac{dy}{dt} + \omega_0^2 y = \Gamma \sin(\omega t), \quad (13)$$

where ω_0 is the natural frequency of the system, ζ is the damping ratio, a parameter of the fitting function. The solution to this equation can be written in several forms depending on the element over which is measured the response. Considering the resonant system in analogy to a mass-spring-damper system, if we measure the transfer function over the damper element, which represents the ascent rate of the intruder, the solution for the gain reads:

$$G(\omega) = \frac{2\zeta\omega_0\omega}{\sqrt{(2\zeta\omega_0\omega)^2 + (\omega_0^2 - \omega^2)^2}}, \quad (14)$$

that we have used to fit the data in Figure 32. Note the bell shape of the fitting curves, analogous to the sharpness curve for the amplitude magnitude typical in traditional resonance

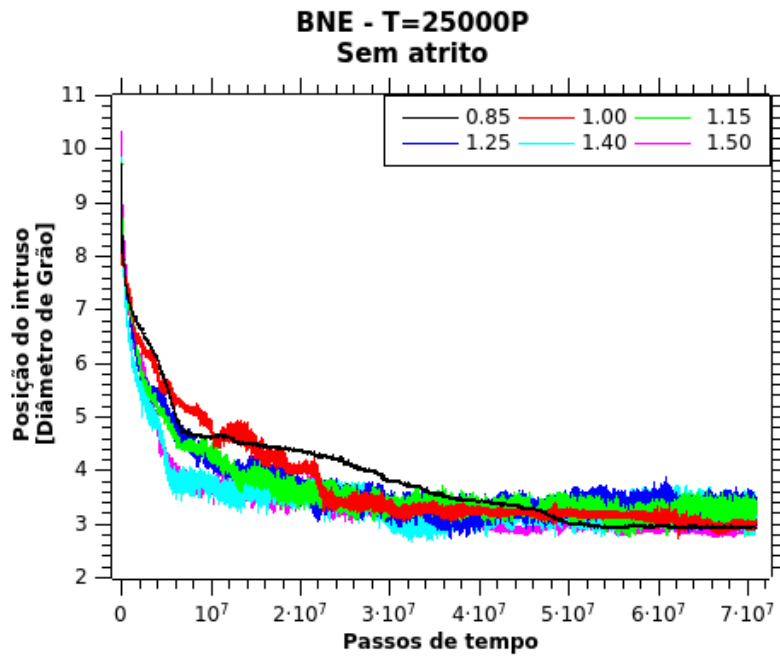


Figure 29 – Time series for the intruder's fall in no friction system. Independent of Γ , the intruder sinks to the bottom.

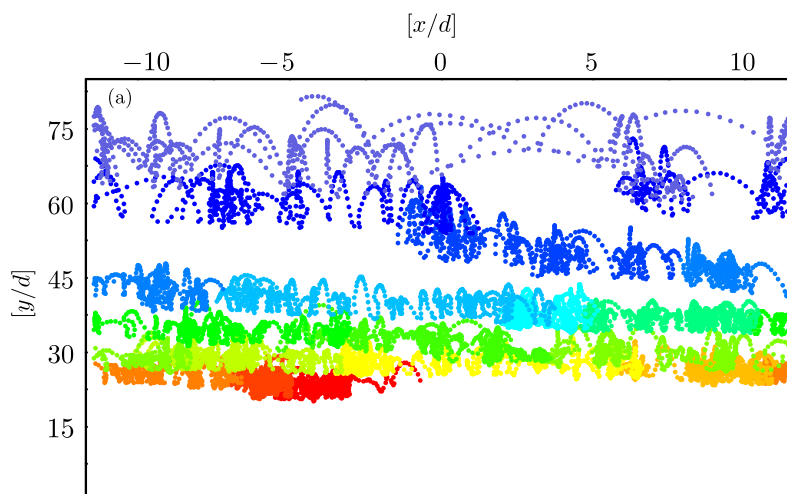


Figure 30 – Sequential positions of the intruder (x, y) taken at constant time intervals ($0.316 \sqrt{d/g}$), for a system with pbc. The shaken frequency $\omega = 0.213 \sqrt{d/g}$. $y = 0$ indicates the box floor and the unities are in unities of the mean grain diameter. The change in colors indicates the time elapsed in the simulation, the red corresponds to the beginning of the simulation and the blue to the end. The width of the pbc in this sequential positions is $w = 25d$. Figure also present in [79].

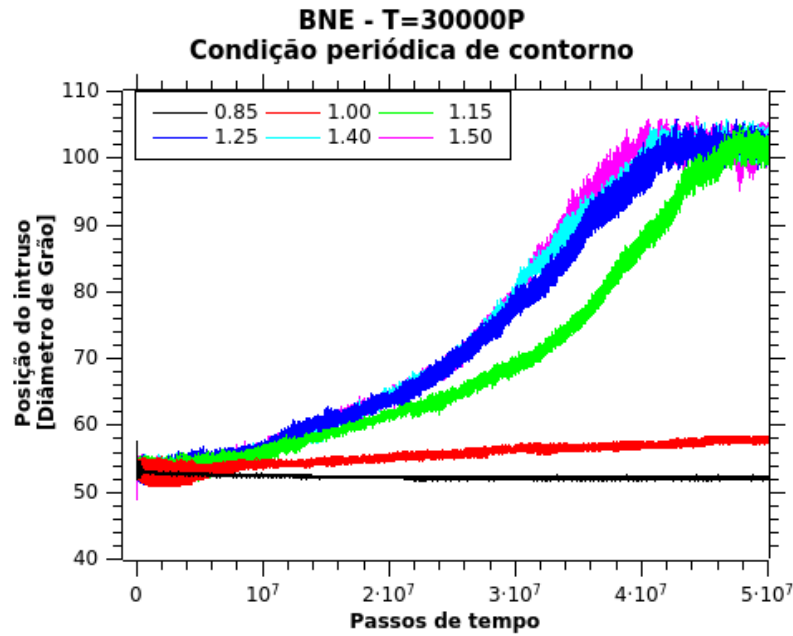


Figure 31 – Time series for intruder horizontal position at different Γ for system with pbc.
The density $\rho_I/\rho_g = 1$, with ρ_I the density of the intruder and ρ_g the density of the media. The value of $\omega = 0.213$. Figure also present in [79].

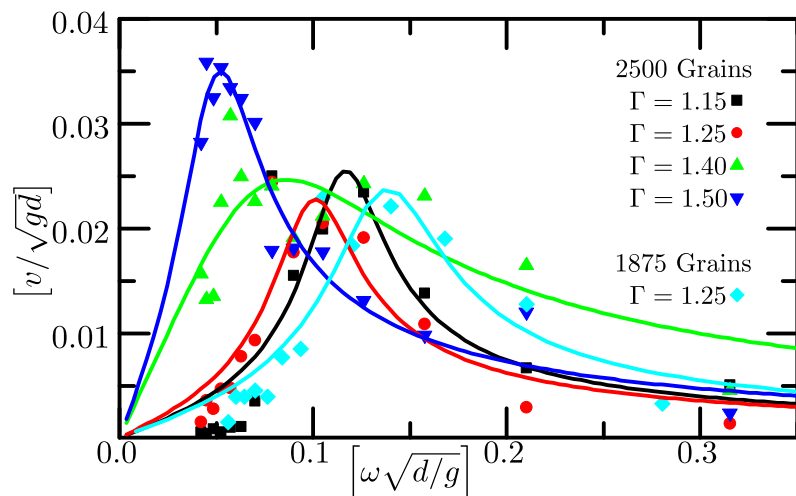


Figure 32 – Intruder ascent rate v curves for various normalized external accelerations Γ , for the pbc case. $\Gamma = 1.15$ and 2500 grains is in ■, $\Gamma = 1.25$ and 2500 grains is in ●, $\Gamma = 1.40$ and 2500 grains is in ▲, $\Gamma = 1.50$ and 2500 grains is in ▼, $\Gamma = 1.25$ and 1875 grains is in ◆, all with $37.5d$ wide. Figure also present in [79].

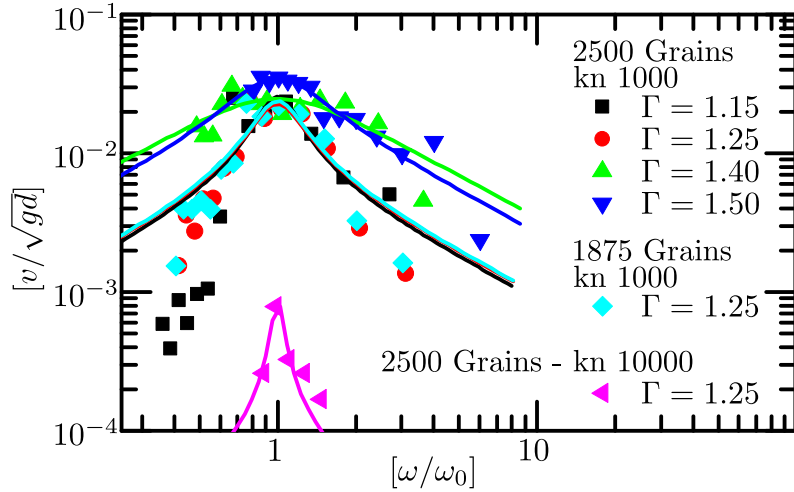


Figure 33 – Collapse of the measured values. The data points are collapsed for all simulations with pbc. The fit can cover the ascent rate for different parameters, like stiffness k_n , normalized acceleration Γ , and the column above the intruder h . Figure also present in [79].

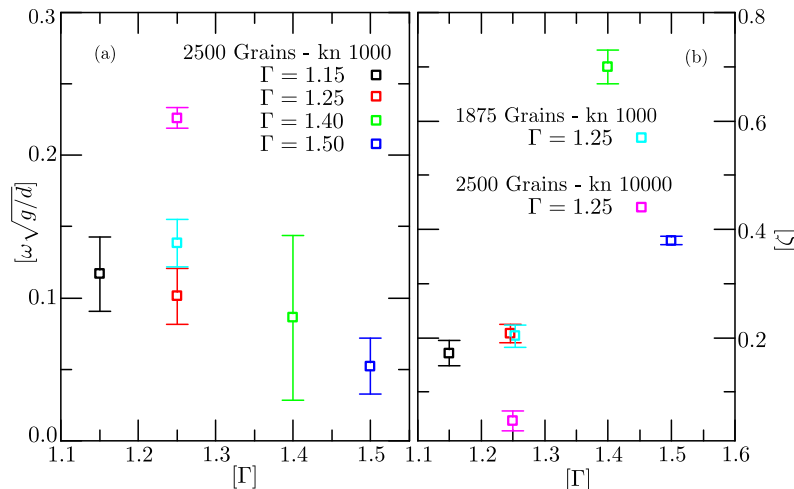


Figure 34 – Fit of the parameters of using Equation (14). In (a), the fitted natural frequency ω_0 shows little dependence with Γ . In (b), the dissipation parameter shows agreement within the error bars to a constant value. Figure also present in [79].

analysis. We use the fact that pbc systems does not have convection current, and the main effect to ascent the intruder is the ratchet effect.

The data could be collapsed around the fitted parameter ω_0 and results in the curve shown in Figure 33. The fitting parameters are shown in Figure 34. Even harder grains obeys this trend. The dynamics of the resonance does not follow exactly the linear approximation, as we can observe in log-log scale, but near the peak the adjust is good.

The damping effect ζ in the fit does not relate to the damping factor γ (or restitution coefficient ϵ) of the grains contact, once the γ is critical and would lead to dissipation of energy enough to resonance does not happen in the contact interaction. A further investigation into this system linking force balance or energy balance to the proposed resonance is needed.

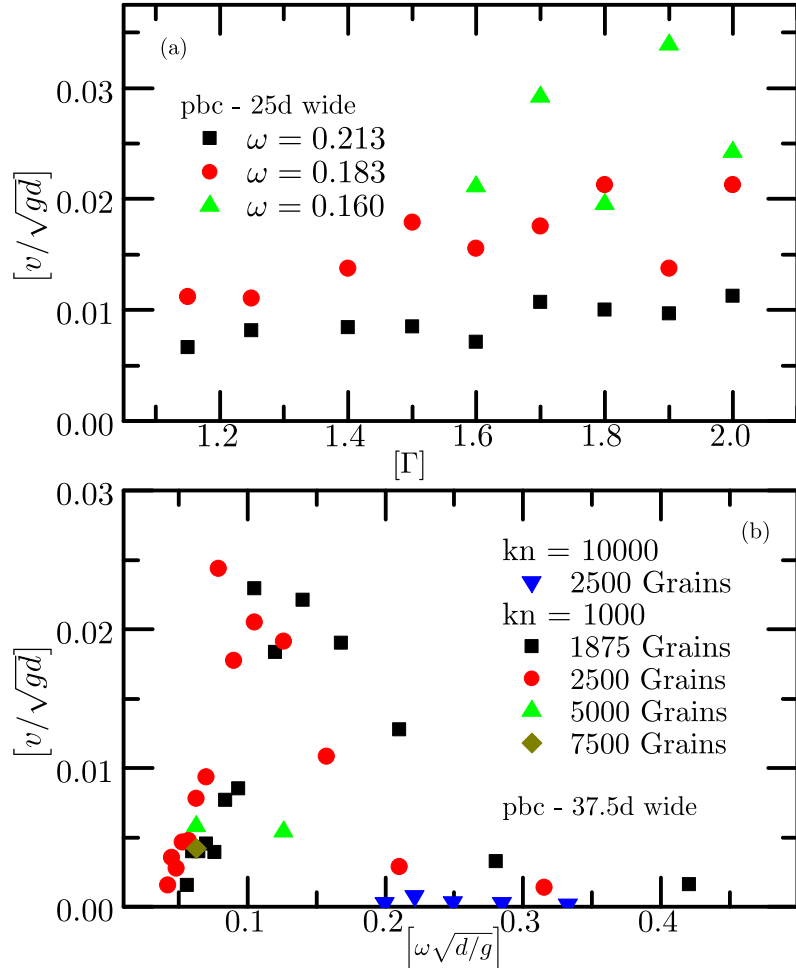


Figure 35 – In (a), 25d wide in pbc. Increase Γ leads to increase ascent rate. In (b) 37.5 wide in pbc. Figure also present in [79].

We propose a scale in the frequency $\omega \propto \sqrt{k_n^3}/h$ while the ascent rate $v \propto \frac{d}{hg} \left(\sqrt{\frac{k_n/m}{\Gamma}} \right)^3$, where k_n is the stiffness of the grains, h is the difference between the top layer of grains and the intruder position, d is the grain diameter, g is the gravity, m is the mass of the grains, and Γ is the dimensionless shaken acceleration compared to the gravity.

And at least comparison in Figure 35, another exploration on the parameters: width of $25d$ and different number of grains in width of $37.5d$, all in pbc.

To reinforce the idea of the resonance, we analyse the fluctuation properties of the ratchet effect using Large Deviation Function (LDF) [78, 13]. We quantify the fluctuations of the ascent rate distribution of the intruder measuring the normalized W_τ as:

$$W_\tau(t) = \frac{1}{\tau} \int_t^{t+\tau} \frac{v(t')}{\langle v \rangle} dt' , \quad (15)$$

where $v(t)$ is the intruder vertical velocity at time t and $\langle \cdot \rangle$ denotes the average over $[0, t + \tau]$. Next, we have calculated $P(W_\tau)$, the density probability function of W_τ , and obtained the RF at the limit

$$RF(W_\tau) = - \lim_{\tau \rightarrow \infty} \frac{1}{\tau} \ln P(W_\tau) . \quad (16)$$

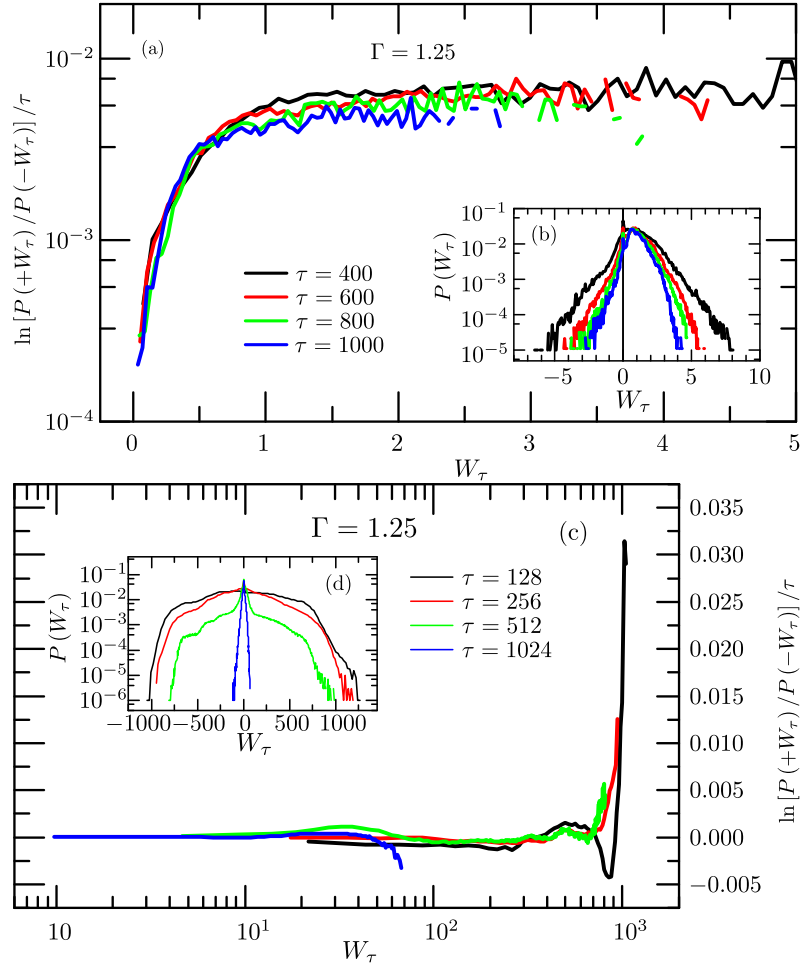


Figure 36 – Inset: $P(W_\tau)$ for $\Gamma = 1.25$ and several values of τ as shown in the legends, for both systems: with frictional walls at left and pbc at right. Main panels: collapse of the RF function calculated for $\Gamma = 1.25$, and several values of τ . Data collapse was performed by dividing the ratio between upward and downward probabilities by the integration time τ . For the range of integration times considered, a remarkable collapse is observed. The frictional walls case is shown at left and pbc at right panel. Observe that distributions for pbc are much more symmetric than those for fw, which lean strongly to the positive side. Figure also present in [79].

We could collapse the curves for long range integration times, when we can see the BNE regime acting in the system. The short time integration did not collapse, once the predominant dynamic is the external oscillation. Figure 36 shows the LDF in fw and pbc. When fw are in play, the asymmetry between falling and rising is pronounced, shown with the metric $P(W_\tau)$ in Figure 36(b). On the other hand, when pbc is consider, the asymmetry of upward and downward is only observed on a high value of τ , Figure 36(d). The RF reaches its value in small W_τ for fw, Figure 36(a), while only long values of W_τ exhibit larger jumps in pbc.

Next Chapter we describe the techniques to simulate the fluid.

6 Methodology - CFD

In this Chapter we describe the model we chose to simulate the fluid, the hypotheses and approximations, the discretization of equations, some methods to solve them, the algorithm and the results of the fluid. We chose to simulate a Finite Difference Method (FDM) with an Eulerian¹ method.

6.1 The fluid model

The general equation that governs the system is the Navier-Stokes equations, which is the application of Newton's second law to specific mass in continuous media and the application of the conservation laws of mass and momentum [11, 12]. For the equation of mass conservation, we have the Equation 17:

$$\frac{\partial \rho^f}{\partial t} + \vec{\nabla} \cdot (\rho \vec{u}^f) = 0, \quad (17)$$

where ρ^f is the fluid density, and \vec{u}^f is the fluid velocity.

The Equation 18 describes the momentum conservation as:

$$\frac{\partial}{\partial t} (\rho^f \vec{u}^f) + \vec{\nabla} \cdot (\rho^f \vec{u}^f \otimes \vec{u}^f) = \bar{\sigma} + p_{ext}, \quad (18)$$

where ρ^f is the fluid density, \vec{u}^f is the fluid velocity, $\bar{\sigma}$ is the fluid stress tensor (pressure p and viscosity τ terms) and p_{ext} is the external pressure, or the body pressure like gravity or drag forces induced by presence of grains.

In formulating the momentum conservation, there is internally the mass conservation, and if we write the terms of the equation making the inner products and the derivatives, we have the Equation:

$$\rho^f \frac{\partial \vec{u}^f}{\partial t} + \rho^f (\vec{u}^f \cdot \vec{\nabla}) \vec{u}^f = \vec{\nabla} \cdot \bar{\sigma} + p_{ext}, \quad (19)$$

where ρ^f is the fluid density, \vec{u}^f is the fluid velocity, $\bar{\sigma}$ is the fluid stress tensor (pressure p and viscosity τ terms) and p_{ext} is the body pressure. The fluid stress tensor $\bar{\sigma}$ is written in 2D like:

$$\bar{\sigma} = \begin{pmatrix} \sigma_{xx} & \tau_{xz} \\ \tau_{zx} & \sigma_{zz} \end{pmatrix}, \quad (20)$$

¹ Eulerian method: a fixed mesh in space with the representative flow evolves in time. The reference point is in the position space.

Lagrangian method: a fixed mesh that moves with the frame and represents the flow in time. The reference point is in the velocity space.

Lattice Boltzmann method: a fixed lattice is set to represent the collision and streaming in time.

where $\bar{\bar{\sigma}}$ is the fluid stress tensor, σ_{xx} and σ_{zz} are the pressure components in the x and z directions, respectively, and the fluid pressure is $p = -\frac{1}{2}(\sigma_{xx} + \sigma_{zz})$, while the shear components are τ_{xz} and τ_{zx} .

The equations above describe most of the fluids, but other enclosures must be done to determine which technique is going to be applied, since the Navier-Stokes equations are not analytically solvable yet and in some cases we have more variables than equations. With this hint in mind, we decided to model the fluid as an incompressible Newtonian fluid. Additionally, we consider that there is no circulation of the fluid in the direction of the gravity (the fluid flows only in x direction), have periodic boundary condition (pbc) in x direction (what happens in the left boundary is exactly same condition to the right boundary) and is constant in the x direction, setting a quasi-1D fluid flow, that changes in the z direction, but only flows in x . The pbc implies in some simplifications on Equations 17, 18 e 19. Automatically, to the Equation 17, the incompressible Newtonian fluid approach leads to any variation in the fluid density ρ^f to be null, so $\frac{\partial \rho^f}{\partial t} = 0$, and if this part is null, then $\vec{\nabla} \cdot (\rho \vec{u}^f) = 0$ is so, and as $\frac{\partial u_z^f}{\partial z} = 0$, $\frac{\partial u_x^f}{\partial x}$ is also null, and it contributes to the assumption that the fluid should be the same in x direction. Also the shear stress $\tau_{xz} = \tau_{zx}$ is symmetric. The component of the pressure $\sigma_{xx} = 0$, due to the pbc, in Equation 19. With all this simplification, we have the total shear stress written as:

$$\vec{\nabla} \cdot \bar{\bar{\sigma}} = \frac{\partial \tau}{\partial z} \hat{x} - \frac{\partial p}{\partial z} \hat{z} \quad (21)$$

where $\bar{\bar{\sigma}}$ is the stress tensor of the fluid, τ is the shear flow component, p is the pressure of the fluid (which has only component in z direction), \hat{x} is the flow direction and \hat{z} is the gravity direction.

An important measure is the fluid strain rate, given by:

$$\dot{\gamma}_{xz} = \frac{1}{2} \left(\frac{\partial u_x}{\partial z} + \frac{\partial u_z}{\partial x} \right), \quad (22)$$

where $\dot{\gamma}_{xz}$ and $\dot{\gamma}_{zx}$ are the components of the strain rate tensor, u_x is the fluid velocity in the flow direction and u_z is the fluid velocity in the direction of gravity.

In this approach, the shear flow controls some characteristics of the fluid, such as the transition from laminar to turbulent approach. The following equation relates the shear and the strain rate:

$$\tau = \rho^f (\nu + \nu_t) \dot{\gamma}, \quad (23)$$

where τ is the shear flow, ρ^f is the fluid density, ν is the intrinsic viscosity of the fluid, ν_t is the contribution of the turbulent model, in terms of viscosity, and $\dot{\gamma}$ is the strain rate. To model a Newtonian fluid, the turbulent part must be null.

Appling the assumed hypothesis about the fluid in the Navier-Stokes equations

(Equation 19), the following system according to the flow direction (x) and gravity (z):

$$\left\{ \begin{array}{l} \rho^f \frac{\partial u_x^f}{\partial t} = \frac{\partial \tau}{\partial z} \\ 0 = -\frac{\partial \sigma_{zz}}{\partial z} + \rho^f g \end{array} \right. \quad \begin{array}{l} : \hat{x}, \\ : \hat{z}, \end{array} \quad (24a)$$

where ρ^f is the fluid density, u_x^f is the velocity in the flow direction, τ is the shear stress, σ_{zz} is the stress component in the direction of the gravity and g is the value of the gravity acceleration.

As expected, the change of pressure depends on gravity and fluid density. Integrating Equation 24b, the pressure is:

$$\sigma_{zz} = \rho^f g z. \quad (25)$$

For the fluid strain rate, applying fluid considerations results in:

$$\dot{\gamma}_{xy} = \frac{\partial u_x}{\partial z}, \quad (26)$$

where $\dot{\gamma}_{xy}$ is the strain rate tensor component, u_x is the fluid velocity in the flow direction and z is the gravity direction.

Now, lets analyse the regimes of the fluid: viscous steady-state and viscous transient.

6.1.1 Viscous steady-state regime

For the viscous regime, all turbulence vanishes, than only viscosity plays a role in the shear. To find a steady-state than, the variation in time must be zero, or:

$$\frac{\partial u}{\partial t} = 0, \quad (27)$$

meaning that:

$$\frac{\partial \tau}{\partial z} = 0, \quad (28)$$

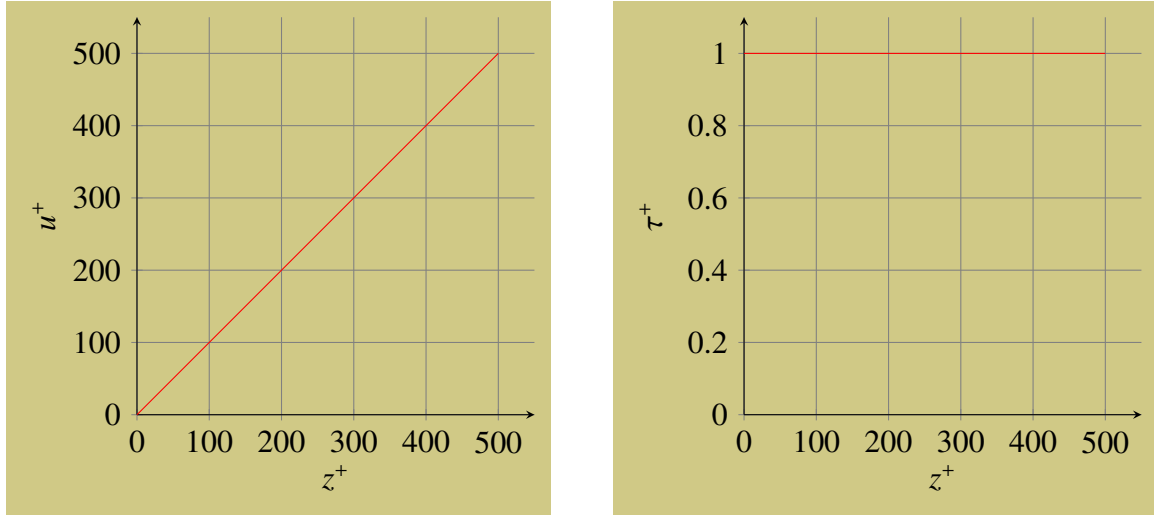
and if the variation on τ is independent of the time and space, in this special case of no turbulence, we can write equation 73 in function of the variation of the velocity over the space as:

$$\frac{\partial u}{\partial z} = \frac{\tau}{\rho \nu}, \quad (29)$$

with $\tau = \rho u_*^2$ imposed on top (u_* been the characteristic velocity of the imposed shear), and it is constant everywhere. Integrating equation and applying the bottom boundary condition, $u = 0$, we get:

$$u^+ = z^+, \quad (30)$$

with $u^+ = u/u_*$ and $z^+ = zu_*/\nu$.



(a) Normalized velocity of viscous steady-state profile.
(b) Normalized shear of viscous steady-state profile.

Figure 37 – Velocity and shear steady-state profiles for the viscous fluid. With viscosity, the response of the velocity profile tends to be a line, and the steady-state makes the shear profile a constant.

As we are not limited by an upper boundary, the fluid has an infinity characteristic length in the steady-state regime.

So then, we now know the exact solution in the steady-state for the viscous fluid. The fluid velocity profile and the fluid shear profile must follow as in figure 37. As said before, the shear profile is constant everywhere, and the velocity profile is a line.

6.1.2 Viscous transient regime

Having the stationary solution in hands, we can think if there is a possibility to describe the transient regime of the equation 24a. This is a linear partial differential equation: the diffusion equation. Equation 31 is the general solution² with the boundary conditions and generic initial velocity profile $u_0(z)$.

$$u^+ = z^+ + \frac{2}{h} \sum_{n=1}^{\infty} \left\{ \int_0^h \left[\frac{u_0(\zeta)}{u_*} - \frac{u_*}{v} \zeta \right] \sin \left(\pi \frac{2n-1}{2h} \zeta \right) d\zeta \right. \\ \left. \sin \left(\pi \frac{2n-1}{2h} z \right) e^{-\left(\pi \frac{2n-1}{2h} \right)^2 vt} \right\}, \quad (31)$$

where z^+ is the normalized steady-state solution, $u_0(\zeta)/u_*$ is the normalized initial velocity profile that covers all the domain between 0 and h , h is the height where we impose the shear to propagate through all of the system, and the integral is the transformation of the function transient into the Fourier coefficients.

² For more details, Attachments A have the whole calculation to get in the solution we got. It is also described in [80], Chapter 10.

The first difference here appears in delimiting an height h at the top. With it, we know that time to change from the initial condition to the stationary regime is dependent of h^2 , so, higher we impose shear, greater is the time to converge to the final solution. If $h \rightarrow \infty$, also the time to converge goes to infinity. It also plays a role in the modes of the Fourier solution.

Looking at the presented solution in equation 31, we can see that it decays with an exponential in time, obeying the differential partial equation 24a according through time, and it is oscillates with an infinite sum of sin in function of space, which is the solution for differential equation of second order in the same equation 24a.

For the initial condition, we choose the one stationary regime with imposed shear as $\tau = \rho(u_* - \Delta u_*)^2$, and then $u_0(z) = (u_* - \Delta u_*)^2 z / \nu$. In terms of Fourier coefficients, it is like:

$$-\frac{8}{\pi^2} h^+ \epsilon (2 - \epsilon) \frac{(-1)^{n-1}}{(2n-1)^2}, \quad (32)$$

that is linear, because $u_0(z) = z(u_* - \Delta u_*)^2 / \nu$ is linear in z . Then, with this, the solution become as following:

$$\begin{aligned} u^+ &= z^+ - \frac{8}{\pi^2} h^+ \epsilon (2 - \epsilon) \\ &\sum_{n=1}^{\infty} \left[\frac{(-1)^{n-1}}{(2n-1)^2} \sin\left(\pi \frac{2n-1}{2h} z\right) e^{-(\pi \frac{2n-1}{2h})^2 \nu t} \right] \end{aligned} \quad (33)$$

If we get the the Fourier mode with higher amplitude and slowest response in equation 33, than we can write the velocity as the function:

$$u^+ = \left[z^+ - \frac{8}{\pi^2} h^+ \epsilon (2 - \epsilon) \sin\left(\frac{\pi}{2h} z\right) e^{-(\frac{\pi}{2h})^2 \nu t} \right] \quad (34)$$

Also, the shear have a temporal evolution, since it is function of the velocity. If we take the derivative of the velocity in function of the space, we can extract the function of shear in time and in space. The 1st Fourier mode of the shear evolves as:

$$\tau^+ = \left[1 - \frac{4}{\pi} \epsilon (2 - \epsilon) \cos\left(\frac{\pi}{2h} z\right) e^{-(\frac{\pi}{2h})^2 \nu t} \right] \quad (35)$$

So, if $\epsilon \ll 1$, then the steady-states are close each other, and the linearization around Δu_* simplifies the transition between two steady states close each other. The reason to get the first Fourier mode is to determine the temporal dominant behavior over the equation.

Than, with the linear approximation described in Equations 34 and 35, we can see the temporal evolution of the profiles in Figures 39 and 38.

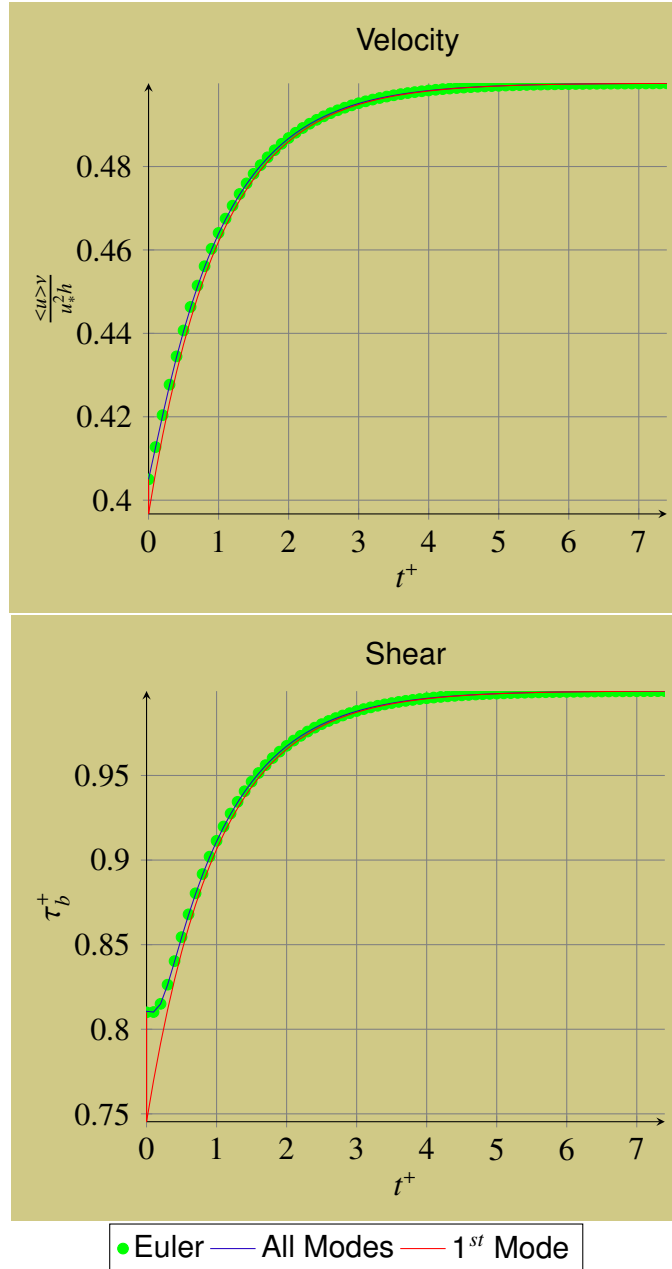
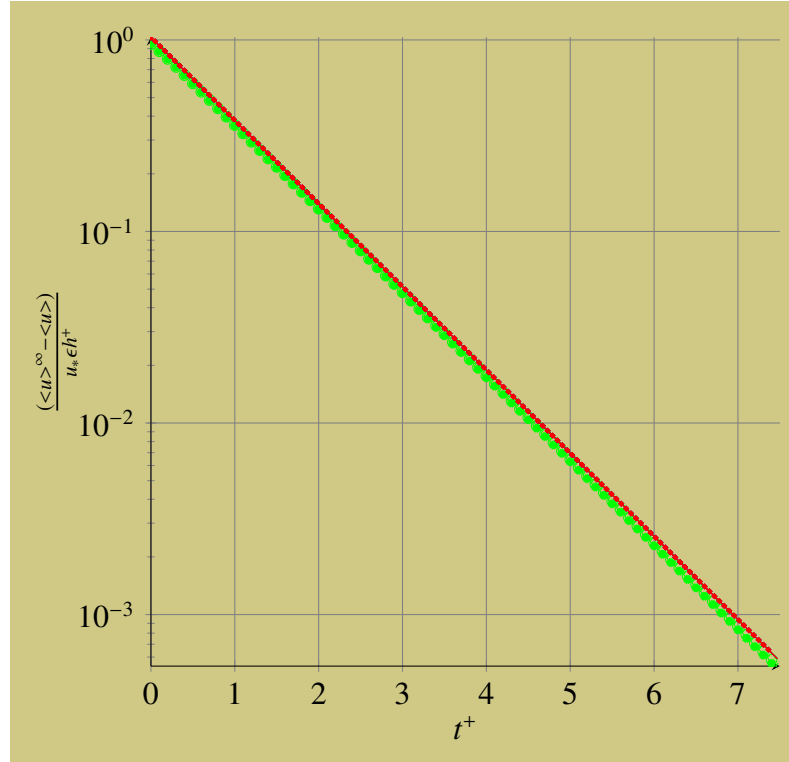
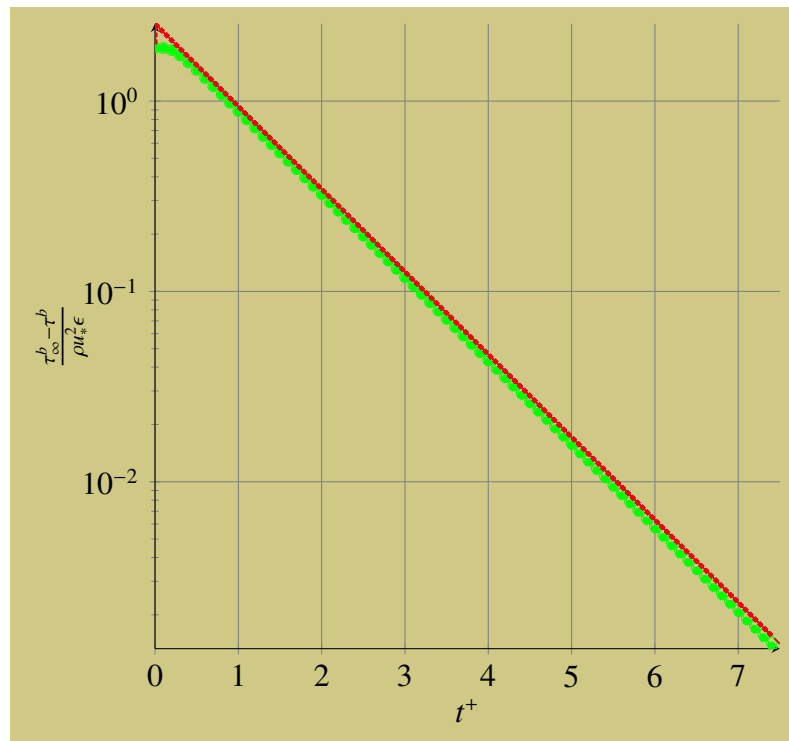


Figure 38 – Temporal evolution of the mean velocity and shear at bottom through time with height $h = 25$ and $\Delta u_* = 0.1u_*$. The curves matches as expected, an exponential decay, from one given point to the asymptotic. Higher modes than the 1st Fourier mode contributes heavily in the beginning but decay fast, and for the main behavior, the 1st Fourier mode gives a good approximation of the temporal evolution. Here we introduce a curve created by the discretization of the equations, that is going to be discuss in section 6.2.1.

Looking at the response on figure 38, one can see that it evolves like an exponential, but to be sure, the best way is to put the variables in semi-log scale. Figure 39 shows the response without the stationary value, focusing the nature of the transition regime.



(a) Normalized mean velocity. In green we have Euler discretization method, in blue we have all Fourier modes and in red we have 1st Fourier mode of viscous transient-state subtracted the stationary regime. For the Fourier modes we have $h = 10$ dotted, $h = 25$ lined and $h = 100$ dashed with $\Delta u_*/u_*$ varying from 10^{-1} to 10^{-3} .



(b) Normalized shear of the bottom layer. In green we have Euler discretization method, in blue we have all Fourier modes and in red we have 1st Fourier mode of viscous transient-state subtracted the stationary regime. For the Fourier modes we have $h = 10$ dotted, $h = 25$ lined and $h = 100$ dashed with $\Delta u_*/u_*$ varying from 10^{-1} to 10^{-3} .

Figure 39 – Normalized velocity and shear stress evolution of viscous transient-state profile through time. All curves collapses at the same one, showing that there is only one behavior that domains the response: the exponential decay. Indeed, as we have expected from the equation in time to go from one stationary regime to the next time regime for a new stationary.

It is also important to look at the approximation of the Fourier's 1st mode in velocity \mathcal{U}_1 in comparison with the original function, that in this case is a line (equation 30) for velocity, and is a constant for shear. Equation 36 contains the first mode linearized in Δu_* and figure 40 has the visual comparison between approximation of the 1st mode and the full solution.

$$\mathcal{U}_1 = -\frac{u_*^2}{\nu} \frac{\Delta u_*}{u_*} h \frac{16}{\pi^2} \sin\left(\frac{\pi}{2h} z\right) \quad (36)$$

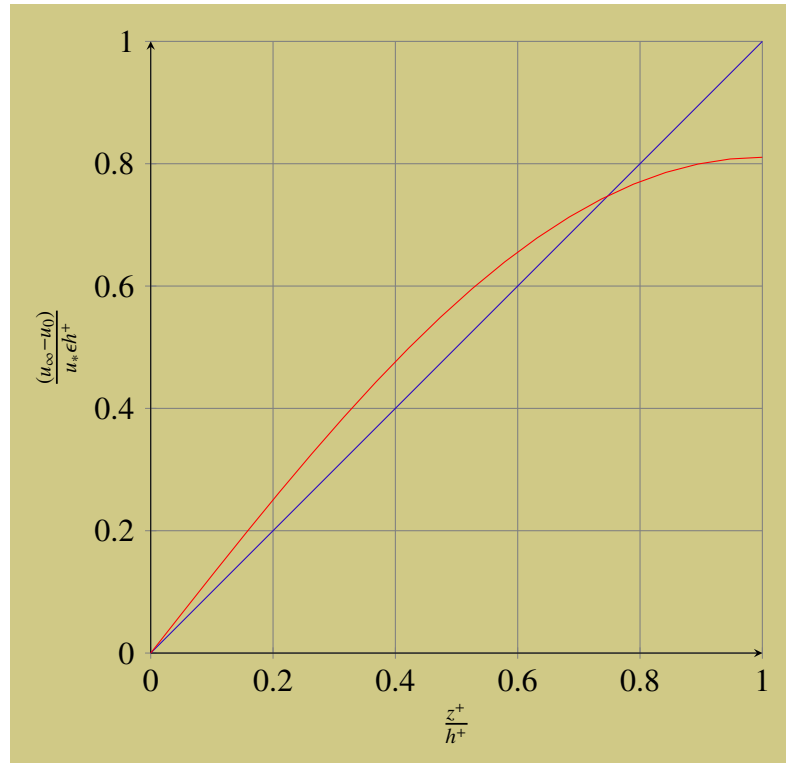


Figure 40 – Amplitude of the first Fourier mode in comparison with full solution. In red, the initial amplitude of the first Fourier mode, in blue the initial amplitude of the all modes.

With the description of the viscous transient regime described and approximated to the first Fourier mode and linearised around the ratio $\Delta u_*/u_*$, now it is time to introduce the turbulence term and see how it evolves in time.

For the stationary turbulent model, using Prandtl turbulent model, the Reference [81] and see the Appendix C.

6.2 Force model - Fluid forces

The forces modelled in this thesis include the contact forces between agents (Chapter 3, which belong to the rheological model of grains), the interaction forces between grain and fluid, and the gravitational force.

The force that the fluid exerts on the grains can be understood as a contribution from different models and cases. A more detailed formulation of each portion of forces that the fluid exerts on each body is described by the equation:

$$\vec{F}_i^{Fluid} = \vec{F}_i^{Arch} + \vec{F}_i^{Drag} + \vec{F}_i^{Magnus} + \vec{F}_i^{Lift} + \vec{F}_i^{AddedMass} + \vec{F}_i^{Basset}, \quad (37)$$

where \vec{F}_i^{Fluid} is the total forces contribution that the fluid exerts on the grain i , \vec{F}_i^{Arch} is the Archimedes' force that acts on the grain i , \vec{F}_i^{Drag} is the drag force on the grain i , \vec{F}_i^{Magnus} is the Magnus' force on the grain i , \vec{F}_i^{Lift} is the lift force on the grain i , $\vec{F}_i^{AddedMass}$ is the added mass force on the grain i and \vec{F}_i^{Basset} is the Basset's force on grain i . As a simplification of the model, we will use only Archimedes' and fluid drag forces [12, 81, 82].

Archimedes' force can be written as in the equation 38, while the drag force can be written as in the equation 39:

$$\vec{F}_i^{Arch} = \frac{\pi}{6} d_i^3 \vec{\nabla} \cdot \vec{\sigma}, \quad (38)$$

where \vec{F}_i^{Arch} is the Archimedes' force on grain i , d_i is the diameter of the grain i and $\vec{\nabla} \cdot \vec{\sigma}$ is the divergent of the fluid stress tensor $\vec{\sigma}$, and:

$$\vec{F}_i^{Drag} = \frac{\pi}{8} \rho_f d_i^2 C_d(\mathcal{R}_u) |\vec{u}_f - \vec{v}_i| (\vec{u}_f - \vec{v}_i), \quad (39)$$

where \vec{F}_i^{Drag} is the drag force on grain i , ρ_f is the fluid density, d_i is the diameter of the grain i , $C_d(\mathcal{R}_u)$ is the drag coefficient based on the body Galileo number, described by Equation 40, \vec{u}_f is the fluid velocity, \vec{v}_i is the grain velocity [81].

$$C_d(\mathcal{R}_u) = \left(\sqrt{C_d^\infty} + \sqrt{\frac{\mathcal{R}_u^c}{\mathcal{R}_u}} \right)^2 \quad (40)$$

where $C_d(\mathcal{R}_u)$ is the drag coefficient based on the body Galileo number, $C_d^\infty \approx 0.5$ is the drag coefficient in the turbulent limit ($\mathcal{R}_u \rightarrow \infty$), $\mathcal{R}_u^c \approx 24$ is the body transition Galileo number, in which the drag coefficient becomes almost constant, and Equation 41 relates the body Galileo number to the parameters of the system:

$$\mathcal{R}_u = \frac{d_i}{\nu} |\vec{u}_f - \vec{v}_i| \quad (41)$$

where d_i is the diameter of the grain i , ν_{tot} is the dynamic viscosity of the system ($\nu + \nu_t$), \vec{u}_f is the fluid velocity and \vec{v}_i is the velocity of the grain i .

With these equations, grain and fluid exchange motion. By third Newton's law, grains exert body forces on the fluid, and fluid reacts with fluid forces on the grains.

6.2.1 Temporal discretization

To numerically solve the fluid equations, a mesh is constructed in z direction, and average it in the x direction each time step. This average make the system to be smoother,

but at same time it gives the probability to have particles' properties in function of z . This smoothness makes the solution more stable to interact the fluid with the grains and update both of them. The first way to think in the discrete equations is the explicit³ form. Then Equations 24a and 29 becomes:

$$\left\{ \begin{array}{l} U_{xk}^{n+1} = U_{xk}^n + \frac{\Delta t}{\rho^f \Delta z} [\tau_k^n - \tau_{k-1}^n] - \frac{\Delta t}{\rho^f} \frac{\phi_k^n}{1 - \phi_k^n} f_{xk}^n, \\ \tau_k^n = \rho^f [\nu] \left(\frac{U_{xk-1}^n - U_{xk}^n}{\Delta z} \right), \end{array} \right. \quad (42a)$$

$$\left\{ \begin{array}{l} U_{xk}^{n+1} = U_{xk}^n + \frac{\Delta t}{\rho^f \Delta z} [\tau_k^n - \tau_{k-1}^n] - \frac{\Delta t}{\rho^f} \frac{\phi_k^n}{1 - \phi_k^n} f_{xk}^n, \\ \tau_k^n = \rho^f [\nu] \left(\frac{U_{xk-1}^n - U_{xk}^n}{\Delta z} \right), \end{array} \right. \quad (42b)$$

where k is the fluid spatial discretization index, n is the time step, U_{xk}^{n+1} is the fluid flow velocity in height $k\Delta z$ and time $(n+1)\Delta t$, U_{xk}^n is the fluid flow velocity in height $k\Delta z$ and time $n\Delta t$, Δz is the fluid meshing space, Δt is the time step interval, ρ^f is the fluid density, ϕ is the packing fraction that solid part occupies, τ is fluid shear, f_x is the force per volume in the x direction that grains exert on the fluid, ν is the fluid viscosity. The stability condition must be obeyed:

$$\frac{2\Delta t}{(\Delta z)^2} < 1 \quad (43a)$$

$$\frac{2\Delta t \cdot SystemSize}{(\Delta z)^2} < 1 \quad (43b)$$

, if there is no grains to exert body force on the fluid, otherwise the stability must be much more rigorous, once numerical errors are amplified due to discretization [83, 84, 85, 86].

But as the explicit form of the equation is unstable, we can rewrite it in the implicit⁴ form:

$$U_{xk}^n - \frac{\Delta t}{\rho^f} \frac{\phi_k^n}{1 - \phi_k^n} f_{xk}^n = -\frac{\Delta t \nu}{(\Delta z)^2} U_{xk-1}^{n+1} \left(1 + 2 \frac{\Delta t \nu}{(\Delta z)^2} \right) U_{xk}^{n+1} - \frac{\Delta t \nu}{(\Delta z)^2} U_{xk+1}^{n+1}, \quad (44)$$

where k is the fluid spatial discretization index, n is the time step, U_{xk}^{n+1} is the fluid flow velocity in height $k\Delta z$ and time $(n+1)\Delta t$, U_{xk}^n is the fluid flow velocity in height $k\Delta z$ and time $n\Delta t$, Δz is the fluid meshing space, Δt is the time step interval, ρ^f is the fluid density, ϕ is the packing fraction that solid part occupies, τ is fluid shear, f_x is the force per volume in the x direction that grains exert on the fluid, ν is the fluid viscosity. But as we can inspect, it is not possible to direct extract the result from this equation, since we have a temporal dependency. The lucky part of it is that this equation can be written in a linear matrix form:

$$[Tridiag] \cdot [U_{xk}^{n+1}] = \left[U_{xk}^n - \lambda \frac{\phi}{1 - \phi} f_{xk}^n \right], \quad (45)$$

³ The explicit way of solving a FDM solves the system for the next time step with the original differential equation operations. All discretization is done on the functions of the current time step resulting in the later time step. The disadvantage of this technique is the instability factor of the solution that can occur. The advantage is that the system can always be written by these equations.

⁴ The implicit way of solving a FDM solves the next time step system based on the differential equation roots of the problem. All discretization is done considering the roots that solve the equation. The disadvantage of this technique is the fact that there is not always an algorithm that finds the roots. The advantage is that the stability factor is more permissive.

where $[Tridiag]$ is a tridiagonal matrix and $\lambda = \frac{v\Delta t}{(\Delta z)^2}$. The tridiagonal matrix have principal diagonal equals to $1+2\lambda$ and upper and lower diagonals equals to $-\lambda$. Then the inverse of the matrix is applied both sides, and the temporal solution is extracted. To make faster calculations, we use Thomas algorithm (Algorithm 10) to invert the matrix and extract the product to the vector $U - \lambda \frac{\phi}{1-\phi} f$.

6.3 Algorithm

Also a series of procedures must be carried out to reach the goal to simulate grain and fluid. As we have discussed in Chapter 3, the simulation of the grain phase should be done, but now taking into the account the fluid force equations into the force calculation routine. The temporal evolution of the fluid phase is adjusted to follow the same time step of the grain phase, and coupling both with the exchange of momentum. The main algorithm that simulates both phases is describe in Algorithm 7, with the introduction of the fluid phase in blue.

Algorithm 7: Given the input of the problem, such as initial positions of bodies, velocities and accelerations, the algorithm assembles a list of bodies that are neighbors delimited by a certain region, then predicts the position and velocity of the bodies at the next instant of time, looks for the contacts that were formed with the prediction, calculates the forces between each body in contact and includes the external forces, and corrects the velocity and acceleration predictions for each body and calculate the fluid dynamics. Thus a DEM+CFD step is constructed. Algorithm adapted from [50].

```

Input :initial simulation data setup
Output :response and simulation measurements over time
while not reached the stop condition of the simulation do
    if it is time to List the Neighbors then
        | List the Neighbors;
    end
    Predictor;
    Detect Contacts;
    Force Calculation;
    Corrector;
    Update fluid;
end
```

6.3.1 Force calculation

The introduction of the fluid causes additional forces to be calculated in the force calculation routine. The Algorithm 8 introduce the fluid forces on the grains. The insertion of the fluid phase is highlighted in blue.

Algorithm 8: In this routine, the resultant forces are calculated for each body. The force \vec{N} is the normal force, contribution of the elastic force \vec{F}^{el} and the damping force \vec{F}^{dam} (Equations 6, 7), F^d is the rolling force of one body on the other, which must be compared with the maximum static friction force μN . Archimedes' and drag forces are calculated every time step on each grain, according to the Equations 38 and 39. Algorithm adapted from [50].

Input :positions, velocities and contact list
Output :acting forces and torques in the bodies
foreach body **do**
 Apply gravity force;
 foreach body in the contact list **do**
 Calculate the normal forces \vec{N} ;
 Calculate the rolling forces F^d ;
 if $|F^d| < \mu |\vec{N}|$ **then**
 $\vec{F}^{at+} = \vec{F}^d \hat{t}$;
 else
 $\vec{F}^{at+} = \mu \text{sign}(\vec{F}^d) \vec{N} \hat{t}$;
 end
 Calculate torque;
 end
 Calculate drag force ;
 Calculate Archimedes' force ;
end

6.3.2 The fluid

The fluid calculation routine consists of updating the fluid mesh⁵ as a function of the system of Equations 42 and 44. The mesh of this fluid is one-dimensional, since we consider the variation of velocities only in the z direction. Thus, we consider a linear mesh of spacing Δz , where Δz is a fraction of the average grain of the system. For good sampling, we use $\Delta z \approx 0.1d$, where d is the average grain diameter. To calculate the pressure that the fluid exerts on the grain, we use the fraction of the body that belongs to the layer in which it is inserted. The sum of all body fractions in the layer results in the packing fraction.

The explicit way to calculate the fluid is strait forward, just plug in the Equations 42, first the shear, later the velocity, since the velocity is dependent on the shear. The implicit way to calculate the fluid needs the attention to the matrix inversion of the system, and it solves the velocity without depending on the shear, so the shear should be extracted after the velocity results. To inverse the matrix, one can do naïvely, with a computational complexity of $O(n^3)$ or use Thomas' algorithm (Algorithm 10), with a computational complexity $O(n)$, n been the number of points in the mesh.

⁵ The fluid mesh consists of the geometric division of space to perform simulation, and is based on discrete points in space associated with a continuous function. This process is the Finite Discrete Method (FDM) [87].

Algorithm 9: Routine that updates the fluid states for the next time step.

Input :velocity and shear fluid profiles, grains drag and Archimedes' forces, time step Δt and spatial step Δz

Output :variables of the fluid ready to simulate next time step

foreach *body* **do**

- | Calculate body pressure on the fluid;

end

forall *fluid* **do**

- | **if** *explicit* **then**

 - | | Calculate the fluid shear;
 - | | Update the fluid velocity;

- | **else if** *implicit* **then**

 - | | Update the fluid velocity;
 - | | Calculate the fluid shear;

end

Algorithm 10: Thomas algorithm adapted to solve the fluid velocity.

Input :fluid velocity profile, fluid pressures due to presence of grains, time step Δt and space step Δz

Output :fluid state to the next time step

$\lambda \leftarrow v\Delta t/(\Delta z)^2$;

$\alpha_1 \leftarrow 0$;

$\beta_1 \leftarrow 0$;

for $k \leftarrow 2$ to $K-1$ **by** 1 **do**

- | $\alpha_k \leftarrow -\lambda/(1 + 2\lambda + \lambda\alpha_{k-1})$;
- | $\beta_k \leftarrow (U_{xk}^n - \Delta t f_{xk}^n \frac{\phi}{1-\phi}/\rho_f + \lambda\beta_{k-1})/(1 + 2\lambda + \lambda\alpha_{k-1})$;

end

$U_{xK}^{n+1} \leftarrow U_{xK}^n + \Delta t \tau_*(U_{xK-2}^n - U_{xK-3}^n)/\Delta z$;

for $k \leftarrow K-1$ to 2 **by** -1 **do**

- | $U_{xk}^{n+1} \leftarrow \beta_k - \alpha_k U_{xk}^n$;

end

6.4 Important parameters

For the fluid, three dimensionless control parameters are important: the density ratio, described by the Equation 46, the Galileo number, which relates the inertial forces with the viscous forces, described by the Equation 47 and the number of Shields, which relates drag forces to inertial forces, described by the Equation 48 [81].

The following equation describes the density ratio between grain and fluid:

$$\mathcal{D}_R = \frac{\rho^p}{\rho_f}, \quad (46)$$

where \mathcal{D}_R is the density ratio, ρ^p is the grain density and ρ_f is the fluid density.

Fluid height	$z^+ = zu_*/\nu$
Fluid velocity	$u^+ = u/u_*$
Fluid shear stress	$\tau^+ = \tau/\rho u_*^2$
Fluid shear imposed at height h	$h^+ = hu_*/\nu$
Time constant of the fluid	$t^+ = t\pi^2\nu/4h^2$
Imposed shear ratio	$\epsilon = \Delta u_*/u_*$

Table 1 – Table of units normalization related to the fluid.

The second dimensionless fluid control parameter is the Galileo number, given by:

$$\mathcal{G} = \frac{d}{\nu} \sqrt{(\mathcal{D}_R - 1) gd}, \quad (47)$$

where \mathcal{G} is the Galileo number in the grain scale, d is the average grain diameter, ν is the fluid velocity, \mathcal{D}_R is the density ratio and g is the gravity value of the system.

The third dimensionless fluid control parameter is the Shields number:

$$\Theta = \frac{u_*^2}{(\mathcal{D}_R - 1) gd}, \quad (48)$$

where Θ is the Shields number, u_* is the characteristic shear velocity, \mathcal{D}_R is the density ratio, g is the gravity value and d is the average grain diameter.

The Table ?? shows some dimensionless parameters we use in this thesis.

Next Chapter we describe the sediment transport.

7 Transporte de Sedimentos

The sediment transport is the movement of solid particles, carried by a fluid over a distance, flowing in the same direction. The transport is a combination of action of gravity on the system and the fluid forces, mainly the fluid drag force. A vast number of phenomena are related to the fluid transport, such as in industrial processes (when transporting ores through a pipeline), or the transformation of landscapes (in the formation or disappearance of dunes) [1]. The different fluids acts differently, resulting in phenomena like: pluvial erosion, river erosion and silting, all caused by water; and phenomena caused by wind, like dunes and desertification.

The types of transport can be classified as shown in figure 41, in which sediments are removed from one location and deposited in another, in different temporal and spatial scales. A formation can appear on the scale of minutes from a few centimetres high on the bottoms of rivers and oceans, to geological formations thousands of years old and hundreds of kilometres long.

Solid materials can be transported by the following modes: bedload, which is the transport of material rolling over a thin layer of the granular base and occurs when the gravitational force is the most prevalent force in the system [88]. Bedload can occur on the bottom of streams and lakes and on the surface of a land. Saltation is the transport mode of materials that collides with the granular base in jumps, occurring when gravitational and drag forces are the most relevant in the system, and can be seen in rivers and in wind erosive processes. Finally suspension is the transport mode of materials in which the drag forces caused by turbulent fluctuations become the order of magnitude of the grain weight and dominate the dynamics of the system [89]. Suspension may be observed in sandstorms or when sweeping house dust.

Single-phase models are not able to reproduce the physics involved in this problem. Models of granular materials without the presence of fluid do not exhibit the properties of

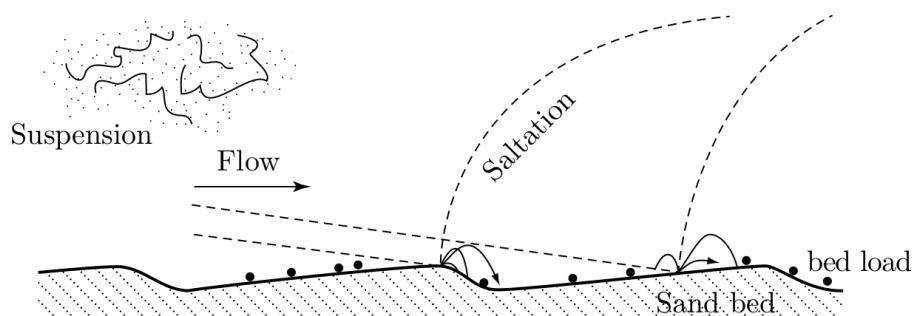


Figure 41 – Schematic diagram of different transport modes. Figure taken from [1].

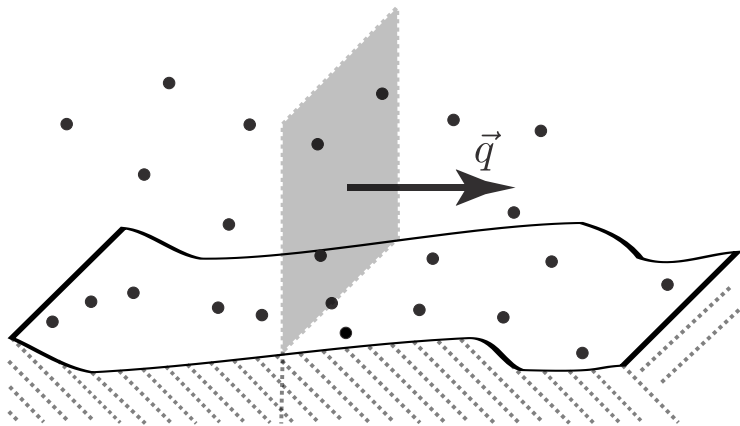


Figure 42 – A schematic of the volumetric flux q . Figure taken from [1].

transport modes such as bedload, saltation and suspension. Likewise, fluid models without sediments are not able to describe the deposition, erosion or even saturation properties. Therefore, it is necessary that the model has the two phases described, sediment and fluid.

Two intrinsic properties of drag are the saturation length scale L_{sat} and the saturation time scale T_{sat} . The saturation length scale quantifies the characteristic distance for the grains to have the maximum density transported by the fluid q_{sat} . The saturation time scale, on the other hand, indicates the characteristic time for the transported material density to decay when the fluid velocity decreases sharply, or for the transported material density to increase when the fluid velocity increases sharply [1]. The main transport governing equation is the Transport Equation, which relates the quantities:

$$T_{\text{sat}} \frac{\partial q}{\partial t} + L_{\text{sat}} \frac{\partial q}{\partial x} = q_{\text{sat}} - q, \quad (49)$$

where T_{sat} is the saturation time that flux takes to adjust, L_{sat} is the saturation length that flux takes to adjust, q_{sat} is the saturated flux, q is the flux, t is the time and x is the direction of the flux.

Aiming at a model capable of reproducing such characteristics, the use of DEM combined with the use of FDM simulate the behavior of grains and fluid, interacting with different approaches to continuous fluid and discrete granular material.

To describe the interactive behavior between fluid and granular material, we will use computer simulations based on the work of Dr. Philippe Claudin [81, 90, 91]. By imposing the initial conditions of the fluid, the time needed for the new regime to reach stationary conditions is measured. The number of grains flowing through the system, in the steady state, provides the saturated volumetric flow q_{sat} , which serves as a parameter for comparing and measuring the saturation time and the saturation length. The process is repeated for each input parameter, thus quantifying the different transitions between modes of transport.

The saturated flux q_{sat} is the main quantity we analyse the sediment transport. It measures the volume of the particles crossing a vertical surface of unit transverse size per

unit time. The definition is as it follows:

$$q_{\text{sat}} = \frac{1}{A\phi_b} \frac{\pi}{6} d^3 \sum_p u^p, \quad (50)$$

where A is the surface area that particles cross, ϕ_b is the packing fraction of the base, d is the average grain diameter and u^p is the grain velocity.

Other two quantities related to the saturated flux is the number of transported grains per unit area n and the mean grain horizontal velocity \bar{u}^p :

$$n = \frac{\left(\sum_p u^p\right)^2}{A \sum_p u^{p2}} \quad (51)$$

$$\bar{u}^p = \sum_p \frac{\sum_p u^{p2}}{\sum_p u^p} \quad (52)$$

and the relation between q_{sat} , n and \bar{u}^p is:

$$q_{\text{sat}} = \frac{1}{\phi_b} \frac{\pi}{6} d^3 n \bar{u}^p. \quad (53)$$

7.1 Threshold

To describe the bedload transportation threshold, we are going to use the same idea from the Book [1]. It consists in writing momentum equations in steady state ($\sum F = 0$) and find the values where they get balanced, for the maximum velocity of the fluid lays the grains in rest. So, the forces that will hold grains statically until moving are given by:

$$m \frac{\partial u_p}{\partial t} = F_{\text{Drag}} + F_{\text{Friction}}, \quad (54)$$

where the acceleration of the particle is $m \frac{\partial u_p}{\partial t} = 0$, due to the steady state regime, F_{Drag} is the drag force, F_{Friction} is the friction force.

$$F_{\text{Drag}} = 3\pi\rho_f \nu d (u_f - u_p), \quad (55)$$

is the drag force onto grains, where ρ_f is the density of the fluid, ν is the viscosity of the fluid, d is the diameter of the grain, u_f is the fluid velocity and u_p is the grains velocity.

$$F_{\text{Friction}} = -\mu_s F_{\text{Gravity}}, \quad (56)$$

is the friction force, and is dependent of the gravity, where μ_s is the static friction coefficient, related to the Coulomb friction.

$$F_{\text{Gravity}} = \frac{\pi}{6} d^3 (\rho_p - \rho_f) g, \quad (57)$$

is the gravity force onto the grains, where ρ_p is the grains density and g is the gravitational acceleration.

And since we know that the fluid shear stress is given by:

$$\tau_f = \rho_f v \frac{\partial u_f}{\partial z}, \quad (58)$$

where τ_f is the fluid shear stress, these equations combined and considering the fact that only the upper half of the particle feels drag force, we have:

$$u_f = \frac{\tau_f}{\rho_f v} \frac{d}{2}. \quad (59)$$

while $u_p = 0$.

Using the Shields number (Equation 48) and manipulating previous equations, when applied drag force is equals to friction force, we can find the threshold by:

$$\Theta_{Th} = \frac{2}{9} \mu_s. \quad (60)$$

7.2 Contribution of moving grains

To introduce the contribution of the moving grains, we are still going to use most of the previous calculation. Still, particles have reached steady state, so $m \frac{\partial u_p}{\partial t} = 0$ is still valid. Considering that grains are moving, we have the balance force:

$$0 = F_{Drag} + F_{Friction} + F_{Grains}, \quad (61)$$

now F_{Grains} is the force due to the moving grains, where it is:

$$F_{Grains} = \frac{\rho_p d^3 u_p \tau_p d^2}{d^2 / \nu}, \quad (62)$$

where $\rho_p d^3 u_p$ is the momentum carried by moving grains, τ_p is the grains shear stress and d^2 / ν is the characteristic time to this viscous contact dynamics.

Looking to the limit just after the threshold, one can get a discontinuity on the grains velocity, and we expect for this behaviour an abrupt change on the friction coefficient, once we change from static regime to moving regime. Then we rewrite equations to include this term:

$$\frac{3}{2} \pi \rho_f v du_p = \frac{3}{2} \pi \rho_f v du_f - \mu_d \frac{\pi}{6} d^3 (\rho_p - \rho_f) g, \quad (63)$$

where μ_d is the new friction coefficient. Then, rewriting $u_p = v_0$ just in the limit after the threshold, we have:

$$v_0 = \frac{2}{9} (\mu_s - \mu_d) v_b, \quad (64)$$

where $v_b = \sqrt{\left(\frac{\rho_p}{\rho_f} - 1\right) gd}$ is the normalised velocity by the grains parameters.

Now, the grains shear stress is:

$$\tau_p \propto n, \quad (65)$$

where n is the number of moving grains by the cross section parallel to the fluid flow divided by the area of this cross section. From previous analysis, we quantify n , \bar{u}_p and q as following:

$$n = a_n (\Theta - \Theta_t) \frac{1}{d^2}, \quad (66a)$$

$$\bar{u}_p = G \frac{\Theta - \Theta_t + u_0}{1 - a_u (\Theta - \Theta_t)} u_b, \quad (66b)$$

$$q_{\text{sat}} = \frac{1}{\phi_b} \frac{\pi}{6} d^3 n \bar{u}_p, \quad (66c)$$

where n is the number of transported grains per unit area, a_n is the adjusted parameter to the data present in Figure 44(d), Θ is the Shields number, Θ_t is the threshold where transportation happens, d is the average grain diameter, \bar{u}^p is the mean grain horizontal velocity, G is the Galileo number, u_0 is the adjusted velocity to the data present in Figure 44(d), a_u is the adjusted parameter to the data present in Figure 44(d), $u_b = \sqrt{\mathcal{D}_R g d}$ is the normalized velocity by the grains parameters, q is the the volume of the particles (at the bed density) crossing a vertical surface of unit transverse size per unit time.

8 Result Analysis and Discussion - Sediment transport: Viscous Bedload

In this Chapter we will present the results obtained from the insertion of the fluid into the granular simulations. Our goal is to simulate the viscous bedload transport mode and extract the time transient T_{sat} and the saturation length L_{sat} . The parameters we used to simulate the system is 10000 grains, with average diameter $d = 1 \pm 20\%$, with uniform distribution. Grains density $\rho^g = 6/\pi$, leading the average mass $m = 1$, the spring constant in the normal direction $k_n = 2500$ and the spring constant in the tangential direction $k_t = 1875$, the restitution coefficient $\epsilon \sim 0.25$ (damping coefficient $\gamma \sim 42\%$ to the critical value), the friction coefficient $\mu = 0.5$ between grain-grain contact. The bottom wall is made of fixed grains and has periodic boundary condition. The time step $dt = \frac{1}{50} \sqrt{\frac{m_r}{k_n}}$, the length $w = 1000d$, the gravity acceleration $g = 1$. The simulations are in a 2D dimensional space (x, z) but we use all parameters as if they are in 3D, and the third component y has average width of $1d$. Grains have spherical geometry. The fluid has the control parameters: density ratio between grains and fluid $\mathcal{D}_R = 2$, Shields number varying from the range $0.05 \leq \Theta \leq 0.5$ equally spaced of 0.05 units, and Galileo number varying from the range $0.01 \leq \mathcal{G} \leq \sqrt{10}$ geometrically spaced of $\sqrt{10}$ units. Viscosity ν is controlled by Galileo number \mathcal{G} (Equation 47) and the characteristic imposed shear velocity u_* is controlled by Shields number Θ (48). The preparation of the grains is done letting the grains fall by gravity, like a rain-like deposition, into the substrate, and after all grains fall, a controlled wind blows inside the grains, moving them into the direction we impose the future fluid profile. The fluid profile is then set to be zero layer by layer, allowing grains to rest, and in the end, the fluid has no motion. This eliminates any residual trace (preparation history) of the rain-like properties. Then the free grains are set to have a height of $10d$ grains, and the grains below this $10d$ column of free grains compounds the base wall. Then the fluid is imposed to have constant shear $\tau = \rho^f u_*^2$ at $10d$ above the granular bed. We set the reference level $0d$ at the granular bed, like in Figure 44 z axis. The fluid evolves from the top to the bed with the time constant as described in Equation 31 ($T = (\frac{4h^2}{\pi^2\nu})$). We wait the fluid reaches the steady-state exchanging momentum with the grains and then we start to measure the profiles, like the ones presented in Figure 44. The steady-state is achieved when the total shear $\tau = \tau^f + \tau^p$ is constant.

8.1 Steady and homogeneous transport

We explore the steady-state by the transport laws described in the set of Equations 66 in Figure 44. To average the quantities we made three different starting samples and run

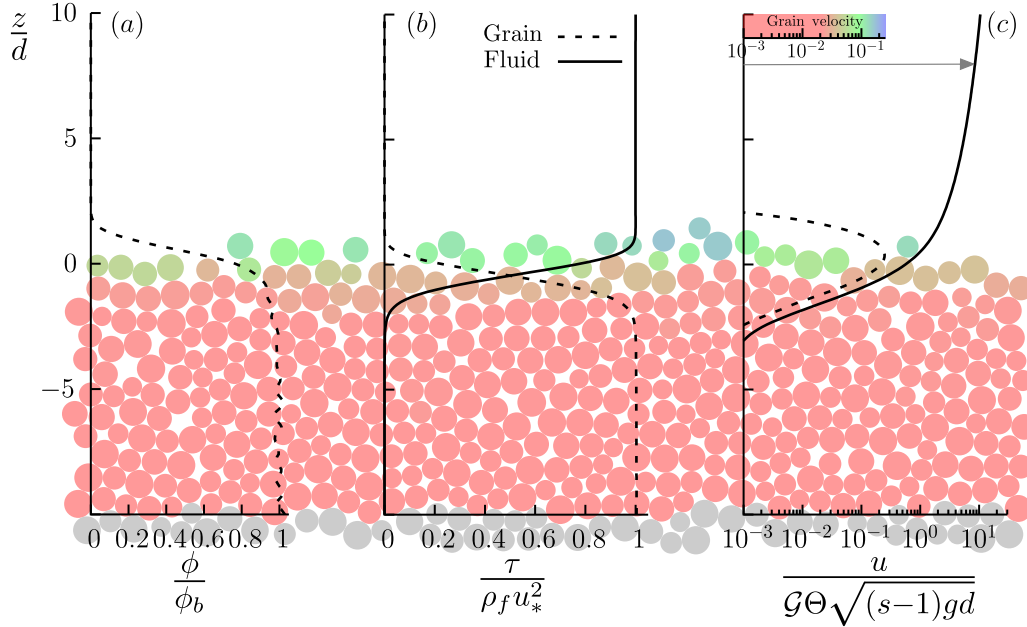


Figure 43 – Schematics of the numerical set-up, with typical vertical (z) profiles of packing fraction (a), shear stress (b) and velocity (c), here all computed with Galileo number $\mathcal{G} = 0.3$ and Shields number $\Theta = 0.3$ in the steady and homogenous case. The full system comprises about 10^4 grains ($1000d$ in length) and has periodic boundary conditions in the horizontal (x) flow direction. (a) Volume fraction ϕ normalised by its value in the bulk of the bed ϕ_b . (b) Shear stress carried by the fluid (solid line) and by the grains (dashed line), normalised by the stress $\rho_f u_*^2$ applied at the top of the fluid. (c) Normalised velocity of the fluid (solid line) and of the grains (dashed line). Flow is from left to right (arrow). On this snapshot, the colour of the grains codes for their instantaneous velocity (inset) – grey grains are the fixed bottom plate.

long time simulations ($10T_{\text{sat}}$) in steady-state. The error bars are shown in figure, except if the associated error is smaller than the symbol.

8.2 Temporal response and saturation time

From Equation 49, with homogeneous wind in the x direction, we simplify the equation, eliminating the factor L_{sat} and any spatial variation for the flux, since $\partial q/\partial x = 0$. Then solving the differential equation, we expect to extract the saturation time T_{sat} from the form:

$$q(t) = q_{\text{sat}} + \delta q_{\text{sat}} e^{-t/T_{\text{sat}}}. \quad (67)$$

After completing the steady-state profiles, we instantly switch the entire fluid profile and measure the temporal transition of the grains to the new fluid profile. We chose to do this instant switch to have a small interference of the fluid, once the transition time for the fluid is related to the viscosity ν and the height h of the imposed shear. The Figure 45 shows

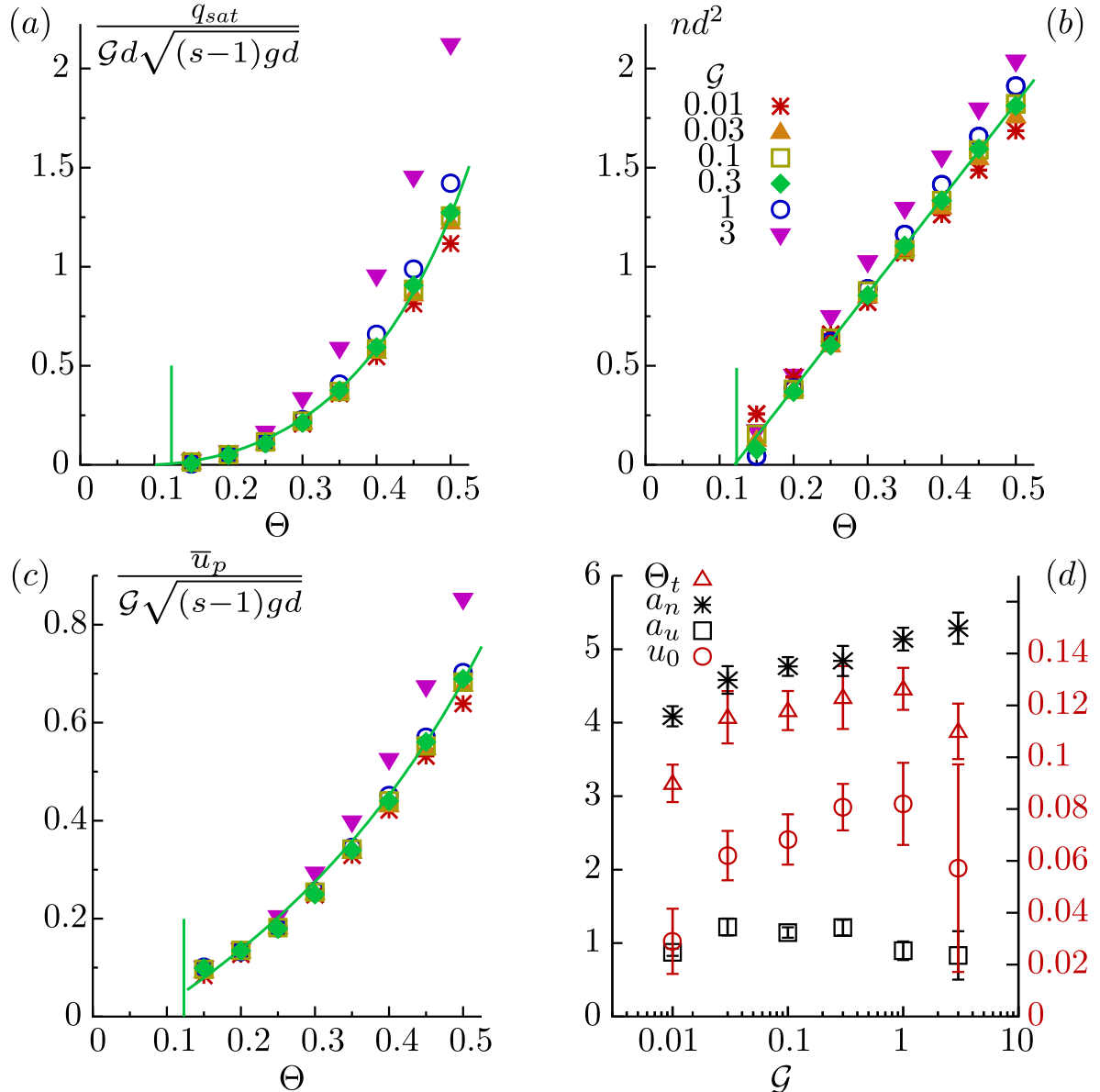


Figure 44 – Transport laws as functions of Θ in the steady and homogenous case: saturated sediment flux q_{sat} (a), moving grain density n (b) and average grain velocity \bar{u}_p (c), plotted in a normalised way to obtain a quasi data collapse. The symbols correspond to different values of \mathcal{G} ranging from 0.01 to 3 (legend). Green solid curves: fit of the data following set of Equations 66, for $\mathcal{G} = 0.3$. Small vertical green line: visualisation of the Shield threshold Θ_t , also for $\mathcal{G} = 0.3$. Panel (d): variation of the fitting parameters with the Galileo number – black (red) symbols associated with left (right) axis.

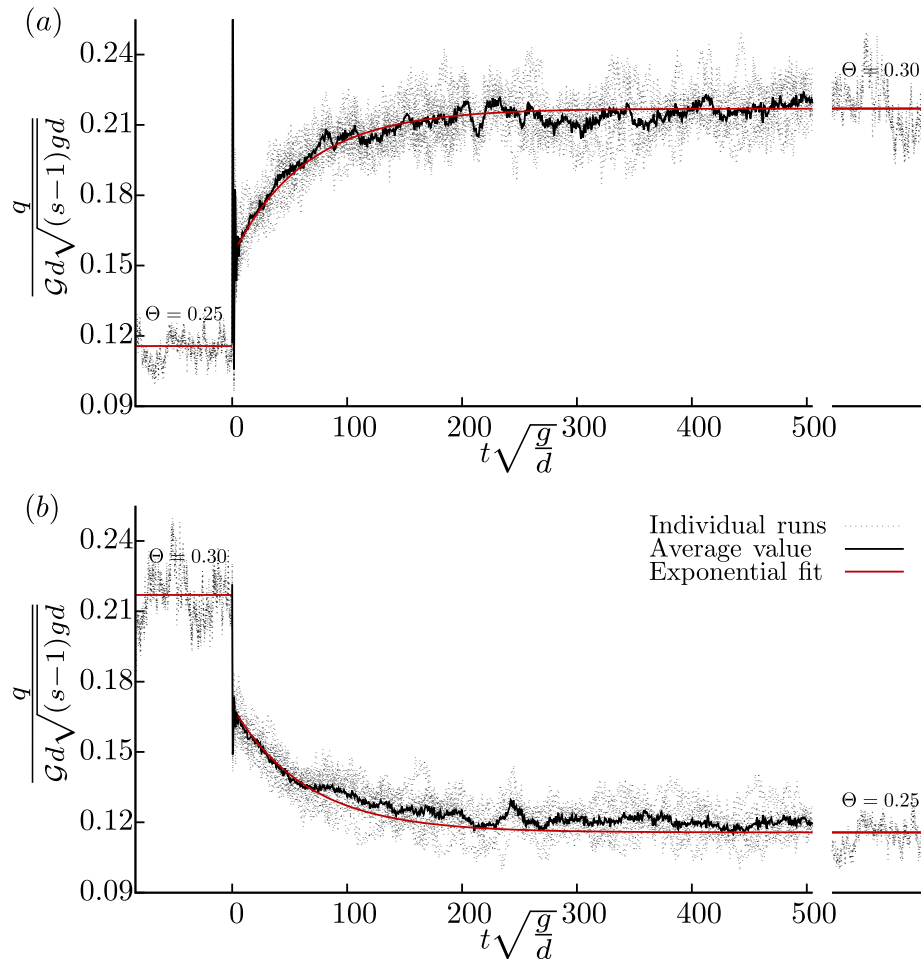


Figure 45 – Time transient of the sediment flux q from one steady state to another, when the Shields number is suddenly increased (a) or decreased (b) by some small amount at $t = 0$. The dash lines show individual runs and the solid lines their ensemble average (legend). Red line: exponential fit to extract the response saturation time, here T_{sat}^q . This example is for $G = 0.3$.

the time transient T_{sat} for Galileo number $G = 0.3$ and the transition from Shields number Θ from 0.25 to 0.3 in Figure 45(a) and the transition from Θ from 0.3 to 0.25 in Figure 45(b).

Gathering the time transient T_{sat} from different Shields number Θ for each Galileo number G we saw that the time transient T_{sat} is invariant with Shields number Θ and inversely proportional to G , as shown in Figure 46(b). The limit of the viscous bedload regime is then expected to be until $G \leq 1$. Measuring the saturation time for q , n and \bar{u}_p are in same order of magnitude. Transitions below to the threshold Θ_t does not happen as grains do not move, while transitions near the threshold is very noisy, with huge errors associated to the measurement.

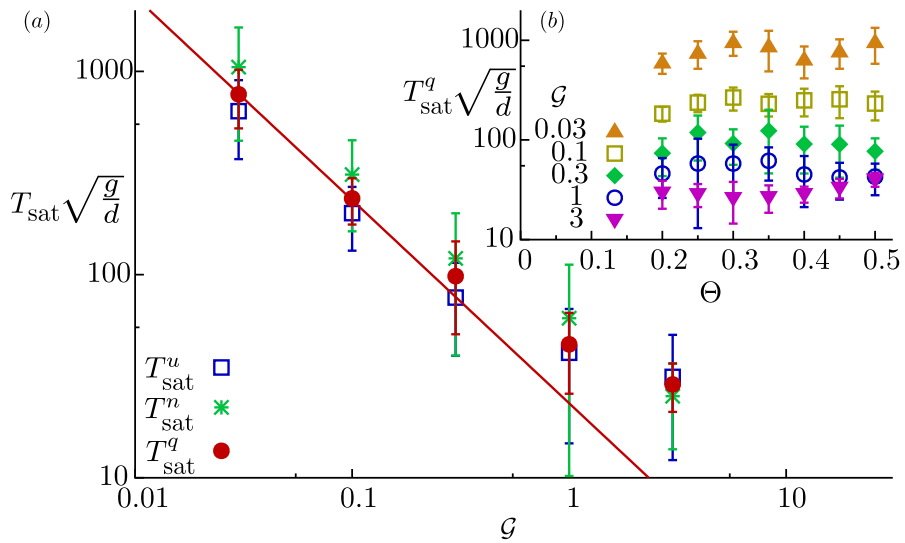


Figure 46 – Variation of the saturation time with the Galileo number. (a) Symbols: T_{sat} associated with the time responses of \bar{u}_p , n and q (legend). Solide red line: inverse law $\propto 1/G$ in this log-log representation. (b) Values of T_{sat}^q for various Θ .

8.3 Spatial perturbation and saturation length

To investigate the spatial relaxation of bedload transport, the idea is to consider a ‘sinusoidal wind’ associated with a spatial modulation of the Shields number: $\Theta(x) = \Theta_0 + \delta\Theta \cos(kx)$. Assuming that $\delta\Theta \ll \Theta_0$, one can linearise the set of Equations 66 with respect to $\delta\Theta$ to obtain a modulated saturated flux:

$$q_{\text{sat}} = q_{\text{sat}}(\Theta_0) \left\{ 1 + \delta\Theta \left[\frac{1}{\Theta_0 - \Theta_t} + \frac{1}{\Theta_0 - \Theta_t + u_0} + \frac{a_u}{1 - a_u(\Theta_0 - \Theta_t)} \right] \cos(kx) \right\}, \quad (68)$$

which is in phase with Shields number. Denoting by ϵ the factor of the cosine in the above expression, the linear response of the actual flux shall take the form

$$q = q_{\text{sat}}(\Theta_0) [1 + \zeta \epsilon \cos(kx - \varphi)]. \quad (69)$$

The relative amplitude ζ and the phase shift φ are related to T_{sat} and L_{sat} through the relaxation equation (49), from which one obtains:

$$T_{\text{sat}} \frac{d\varphi}{dt} = -\frac{1}{\zeta} \sin \varphi + kL_{\text{sat}} \quad \text{and} \quad T_{\text{sat}} \frac{d\zeta}{dt} = -\zeta + \cos \varphi. \quad (70)$$

The integration of these equations give $\zeta(t)$ and $\varphi(t)$ that start linearly with time for $t \ll T_{\text{sat}}$, and then saturate to asymptotic values $\tan \varphi_\infty = kL_{\text{sat}}$ and $\zeta_\infty = \cos \varphi_\infty$ as soon as $t \gtrsim 2T_{\text{sat}}$. Here we will use the measurement of those asymptotic values to deduce the saturation length L_{sat} .

The way to induce this linearisation proposed to achieve the ‘sinusoidal wind’ we turn off the feedback of the grains into the fluid, making the fluid profile fixed according to time,

but modulated in the x direction. The Figure 47 shows the values of L_{sat} . Our main idea is to relate L_{sat} with other parameters, mainly T_{sat} . We could extract the following prediction:

$$L_{\text{sat}} \propto \bar{u}^p T_{\text{sat}}, \quad (71)$$

and the proportionality constant is about 3.7. With this prediction, we can simulate the system to be in quadrature of phase between the imposed wind and the flux response.

Next Chapter we conclude this thesis, and set the open perspectives to continue this work.

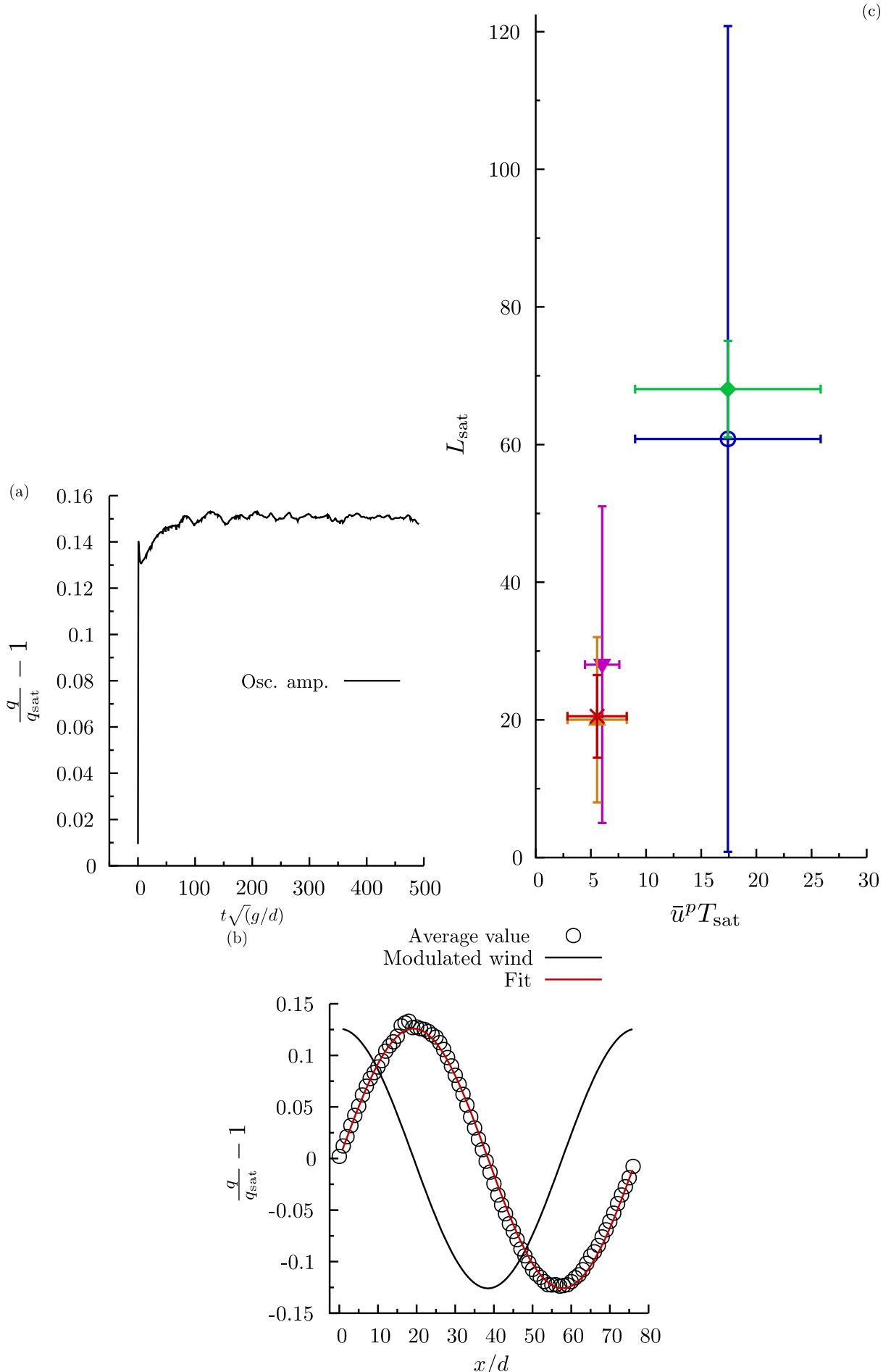


Figure 47 – Example of modulated flux with the imposed wind (a). The amplitude of the modulated response in time: the amplitude takes about $2T_{\text{sat}}$ to accommodate (a) and we extract the temporal cumulated response in (b). Finally, the saturation

9 Conclusions

First of all, we successfully use the DEM technique to simulate dry granular materials and we coupled it with FDM to simulate the transport fluid.

For the BNE simulations we were able to reproduce the intruder's ascent properties with different densities, different vibration amplitudes and different vibration frequencies, noting the importance of frictional walls on convection effect of the system. More than that, we were able to perform the BNE in a system that has a periodic boundary condition and its differences to the closed box system. We characterized the intruder's ascent rate according to the shaken frequency, understanding that the BNE phenomena in this conditions can be interpreted as a resonance effect. An important metric was applied, enhancing our understanding of the BNE phenomena: the LDF.

For the sediment transport, we were able to validate the physical properties that govern the system, matching simulation with movement conservation. We validate the fluid according to the literature and couple grain and fluid so that they interact under the laws of physics. We also extracted and characterized the transport law for viscous bedload regime exploring systematically two parameters: the Galileo number G and the Shields number Θ . Well characterized the steady-state, we moved to the transient regime, exploring the saturation time T_{sat} and further the saturation length L_{sat} . We could deduce constitutive relations from force balance and from dimensionless analysis.

9.1 Future works

At this moment, we are finishing the last simulations to extract the saturation length L_{sat} and preparing the manuscript documenting our results of the viscous bedload transport. We plan to submit this work on the Journal of Fluid Mechanics, detailing all the work we did until now in this subject.

We also plan to analyse the fluctuations in the BNE when the intruder enters in the convection current in problems with fw, and we think in how to explore this problem using the metrics of the energy, relating the BNE with its loss of energy.

Personally, I am planning to improve the numerical technique to simulate 3D granular materials, and extend the CFD also to 3D to analyse dune formations in viscous transportation. The CFD field is vast, but I wish to simulate mesh techniques using Discret Fourier Transform (DFT), since the fast algorithm, Fast Fourier Transform (FFT), is executable in the order of $O(n \log n)$ and seems to be perfectly matching with the granular phase.

Referências

- 1 ANDREOTTI, B.; FORTERRE, Y.; POULIQUEN, O. **Granular media: between fluid and solid.** [S.I.]: Cambridge University Press, 2013. Cited 6 times on pages 1, 5, 6, 55, 56, and 57.
- 2 DURAN, J.; REISINGER, A.; GENNES, P. de. **Sands, Powders, and Grains: An Introduction to the Physics of Granular Materials.** [S.I.]: Springer New York, 1999. (Partially Ordered Systems). ISBN 9780387986562. Cited 3 times on pages 1, 4, and 6.
- 3 HINRICHSEN, H.; WOLF, D. E. **The Physics of Granular Media.** [S.I.]: WILEY-VCH Verlag GmbH, 2004. ISBN 3-527-40373-6. Cited 2 times on pages 1 and 11.
- 4 METHA, A. **Granular Physics.** [S.I.]: Cambridge University Press, 2007. ISBN 13 978-0-521-66078-5. Cited 4 times on pages 1, 6, 8, and 24.
- 5 SATAKE, M.; JENKINS, J. **Micromechanics of Granular Materials: Proceedings of the U.S./Japan Seminar on the Micromechanics of Granular Materials, Sendai-Zao, Japan, October 26-30, 1987.** Elsevier Science, 2013. (Studies in Applied Mechanics). ISBN 9781483290157. Disponível em: <<https://books.google.com.br/books?id=lgUhBQAAQBAJ>>. Cited on page 1.
- 6 TAVARES, A. M. **Simulação de materiais granulares aplicada a transportadores de correia.** Dissertação (Mestrado) — CEFET-MG - Centro Federal de Educação Tecnológica de Minas Gerais, Jan 2017. Cited 2 times on pages 1 and 14.
- 7 JANSSEN, H. A. Versuche über Getreidedruck in Silozellen. **Zeitschr. d. Vereines deutscher Ingenieure**, v. 39, n. 35, p. 1045–1049, 1895. Cited on page 1.
- 8 SPERL, M. Experiments on corn pressure in silo cells. translation and comment of janssen's paper from 1895. **Granular Matter**, v. 8, n. 2, p. 59–65, 2006. Cited on page 1.
- 9 CONIGLIO, A. et al. **Unifying Concepts in Granular Media and Glasses.** London, UK: Elsevier, 2004. ISBN 0 444 51607 7. Cited 2 times on pages 1 and 4.
- 10 ALLEN, M. P.; TILDESLEY, D. J. **Computer Simulation of Liquids.** Reprint. [S.I.]: Oxford University Press, USA, 1989. Paperback. (Oxford science publications). ISBN 0198556454. Cited 6 times on pages 1, 14, 19, 20, 21, and 23.
- 11 E. HULIN J. P., P. L. G.; D., M. C. **Physical Hydrodynamics.** Second. [S.I.]: Oxford, 2015. Cited 2 times on pages 2 and 41.
- 12 KUNDU, P.; COHEN, I.; DOWLING, D. **Fluid Mechanics.** Academic Press, 2012. ISBN 9780123821003. Disponível em: <https://books.google.fr/books?id=iUo_4tsHQYUC>. Cited 3 times on pages 2, 41, and 49.
- 13 VULPIANI, A. et al. **Large Deviations in Physics.** Berlin,Heidelberg: Springer, 2014. Cited 2 times on pages 2 and 39.

- 14 MAGALHÃES, C. F. M. **Engarrafamento e segregação em empilhamentos abertos de grãos.** Tese (Doutorado) — UFMG - Universidade Federal de Minas Gerais, Jul 2013. Cited 9 times on pages 3, 8, 11, 14, 16, 17, 18, 23, and 24.
- 15 CARSON, J. W. Silo failures: case histories and lessons learned. v. 10, p. 153–166, 12 2001. Cited on page 3.
- 16 ROMERO, S. **Authorities Assess Toll of Burst Dam in Brazil.** Rio de Janeiro: The New York Times, Nov 2015. 10 p. <<https://www.nytimes.com/2015/11/06/world/americas/authorities-assess-toll-of-burst-dam-in-brazil.html>>. Cited on page 3.
- 17 NOGUEIRA, D. et al. **Tsunami de lama.** Rio de Janeiro: O Globo, Nov 2015. <<http://memoria.oglobo.globo.com/jornalismo/primeiras-paginas/tsunami-de-lama-18775124>>. Cited on page 3.
- 18 GATINOIS, C. **Catastrophe écologique au Brésil à la suite de la coulée de boue toxique.** São Paulo: Le Monde, Nov 2015. <https://www.lemonde.fr/planete/article/2015/11/17/catastrophe-ecologique-au-bresil-apres-la-coulee-de-boue-toxique_4811803_3244.html>. Cited on page 3.
- 19 DARLINGTON, S. et al. **A mining dam collapsed and buried more than 150 people. Now Brazil is casting an anxious eye on dozens of dams like it.** New York: The New York Times, Feb 2019. <<https://www.nytimes.com/interactive/2019/02/09/world/americas/brazil-dam-collapse.html>>. Cited on page 3.
- 20 MINAS, G. **Barragem da Vale se rompe em Brumadinho, MG.** Belo Horizonte: O Globo, Jan 2019. <<https://g1.globo.com/mg/minas-gerais/noticia/2019/01/25/bombeiros-e-defesa-civil-sao-mobilizados-para-chamada-de-rompimento-de-barragem-em-brumadinho.ghtml>>. Cited on page 3.
- 21 ESCANDE, P. **Rupture du barrage de Brumadinho : « La mine tue encore ».** Paris: Le Monde, Jan 2019. <https://www.lemonde.fr/economie/article/2019/01/29/rupture-du-barrage-de-brumadinho-la-mine-tue-encore_5416071_3234.html>. Cited on page 3.
- 22 HALLIDAY, D.; RESNICK, R. **Fundamentals of Physics.** [S.I.]: John Wiley and Sons, 1970. ISBN 0471344303. Cited on page 4.
- 23 OSTOJIC, S. **Statistical Mechanics of Static Granular Matter.** Tese (Doutorado) — Universiteit van Amsterdam Faculteit der Natuurwetenschappen, Wiskunde en Informatica, Sep 2006. Cited 3 times on pages 4, 14, and 17.
- 24 JAEGER, H. M.; NAGEL, S. R.; BEHRINGER, R. P. Granular solids, liquids, and gases. **Reviews of Modern Physics**, American Physical Society, v. 68, n. 4, p. 1259–1273, out. 1996. Disponível em: <<http://dx.doi.org/10.1103/revmodphys.68.1259>>. Cited on page 5.
- 25 FRETTE, V. et al. Avalanche dynamics in a pile of rice. **Nature**, v. 379, p. 49–52, 1996. Cited on page 7.
- 26 RAMOS, O.; ALTSCHULER, E.; MÅLØY, K. J. Avalanche prediction in a self-organized pile of beads. **Physical Review Letters**, v. 102, p. 078701, 2009. Cited on page 7.
- 27 OTTINO, J. M.; KHAKHAR, D. V. Mixing and segregation of granular materials. **Annual Review of Fluid Mechanics**, v. 32, n. 1, p. 55–91, 2000. Cited on page 7.

- 28 LUMAY, G. et al. Measuring the flowing properties of powders and grains. **Powder Technology**, v. 224, p. 19 – 27, 2012. ISSN 0032-5910. Disponível em: <<http://www.sciencedirect.com/science/article/pii/S0032591012000885>>. Cited on page 7.
- 29 TORDESILLAS, A. et al. Revisiting localized deformation in sand with complex systems. **Proceedings of the Royal Society of London A: Mathematical, Physical and Engineering Sciences**, The Royal Society, v. 469, n. 2152, 2013. ISSN 1364-5021. Cited on page 7.
- 30 SMART, A.; OTTINO, J. M. Granular matter and networks: three related examples. **Soft Matter**, The Royal Society of Chemistry, v. 4, p. 2125–2131, 2008. Cited on page 7.
- 31 ARANSON, I. S.; TSIMRING, L. S. Patterns and collective behavior in granular media: Theoretical concepts. **Rev. Mod. Phys.**, American Physical Society, v. 78, p. 641–692, Jun 2006. Cited on page 7.
- 32 MALLOGGI, F. G. J. **Etudes expérimentales d'avalanches granulaires**. Tese (Doutorado) — Université Paris-Diderot - Paris VII, Apr 2006. Cited on page 7.
- 33 VANEL, L. et al. Memories in sand: Experimental tests of construction history on stress distributions under sandpiles. **Phys. Rev. E**, American Physical Society, v. 60, p. R5040–R5043, Nov 1999. Disponível em: <<http://link.aps.org/doi/10.1103/PhysRevE.60.R5040>>. Cited 3 times on pages 7, 8, and 10.
- 34 LUCK, J.; MEHTA, A. Dynamics at the angle of repose: jamming, bistability, and collapse. **Journal of Statistical Mechanics: Theory and Experiment**, IOP Publishing, v. 2004, n. 10, p. P10015, 2004. Cited on page 7.
- 35 PETERS, J. F. et al. Characterization of force chains in granular material. **Phys. Rev. E**, American Physical Society, v. 72, p. 041307, Oct 2005. Cited on page 8.
- 36 ASTE, T.; MATTEO, T. D.; TORDESILLAS, A. **Granular and Complex Materials**. World Scientific Publishing Company Pte Limited, 2007. (World Scientific lecture notes in complex systems). ISBN 9789812771995. Disponível em: <<https://books.google.com.br/books?id=GhPWAHa4-zoC>>. Cited on page 8.
- 37 ATMAN, A. P. F. et al. Sensitivity of the stress response function to packing preparation. **Journal of Physics: Condensed Matter**, v. 17, n. 24, p. S2391–S2403, 2005. Disponível em: <<http://dx.doi.org/10.1088/0953-8984/17/24/002>>. Cited 4 times on pages 8, 9, 10, and 11.
- 38 MAGALHÃES, F. G. R. **A Study on Granular Hopper Flow via Discrete Element Method Computational Simulations**. Tese (Doutorado) — UFMG - Universidade Federal de Minas Gerais, Fev 2018. Cited 3 times on pages 8, 11, and 14.
- 39 TANG, J. **Investigating Wield Jamming Problem**. 2012. <<http://webhome.phy.duke.edu/~jt41/research.html>>. 17-06-2021. Cited on page 9.
- 40 PAIXÃO, N. M. M. **Formação de Padrões em Sistemas Granulares Confinados**. Dissertação (Mestrado) — CEFET-MG -Centro Federal de Educação Tecnológica de Minas Gerais, Nov 2015. Cited 2 times on pages 8 and 14.

- 41 SILVA, L. O. **Reologia $\mu(I)$ em escoamentos granulares por método de elementos discretos.** Dissertação (Mestrado) — CEFET-MG -Centro Federal de Educação Tecnológica de Minas Gerais, Fev 2020. Cited 2 times on pages 8 and 14.
- 42 OLIVEIRA, F. F. d. **Estudo do comportamento de uma fibra em um meio granular denso.** Dissertação (Mestrado) — CEFET-MG -Centro Federal de Educação Tecnológica de Minas Gerais, Aug 2019. Cited 2 times on pages 8 and 14.
- 43 GOLDENBERG, C.; GOLDHIRSCH, I. Force chains, microelasticity, and macroelasticity. **Phys. Rev. Lett.**, American Physical Society, v. 89, p. 084302, Aug 2002. Cited on page 8.
- 44 BOAVENTURA, E. C. **Geometria computacional aplicada à mecânica de materiais granulares.** Tese (Doutorado) — CEFET-MG -Centro Federal de Educação Tecnológica de Minas Gerais, Aug 2020. Cited on page 11.
- 45 ATMAN, A. P. F. et al. Non-gaussian behavior in jamming/unjamming transition in dense granular materials. **POWDERS AND GRAINS 2013: Proceedings of the 7th International Conference on Micromechanics of Granular Media**, v. 1542, n. 1, p. 381–384, 2013. Cited on page 11.
- 46 CRUZ, F. D. **Friction and jamming in dry granular flows.** Tese (Doutorado) — Ecole des Ponts ParisTech, Dec 2004. Cited on page 11.
- 47 CIXOUS, P. et al. Jamming and unjamming by penetration of a cylindrical intruder inside a 2 dimensional dense and disordered granular medium. **AIP Conference Proceedings**, v. 1145, n. 1, p. 539–542, 2009. Cited on page 12.
- 48 RADJAI, F.; ROUX, J.-N.; DAOUADJI, A. Modeling granular materials: Century-long research across scales. **Journal of Engineering Mechanics**, v. 143, n. 4, p. 04017002, 2017. Cited 2 times on pages 11 and 12.
- 49 REYNOLDS, O. Lvii. on the dilatancy of media composed of rigid particles in contact. with experimental illustrations. **The London, Edinburgh, and Dublin Philosophical Magazine and Journal of Science**, Taylor & Francis, v. 20, n. 127, p. 469–481, 1885. Cited on page 11.
- 50 MARTINS, G. H. B. **Simulação paralela de materiais granulares.** Dissertação (Mestrado) — CEFET-MG - Centro Federal de Educação Tecnológica de Minas Gerais, Set 2015. Cited 10 times on pages 14, 16, 17, 20, 21, 22, 23, 51, 52, and 76.
- 51 LUDING, S. **Models and Simulations of Granular Materials.** Tese (Doutorado) — University of Freiburg, Oct 1994. Cited 3 times on pages 14, 17, and 23.
- 52 MAGALHÃES, C. F. M. **Simulação de materiais granulares.** Dissertação (Mestrado) — UFMG - Universidade Federal de Minas Gerais, Aug 2008. Cited on page 14.
- 53 MEHDI, B. **Comportement rhéologique et effets non-locaux dans les écoulements granulaires denses.** Tese (Doutorado) — Université Paris Diderot, Out 2014. Cited 2 times on pages 14 and 23.
- 54 WASSGREN, C. R. **Vibration of Granular Materials.** Tese (Doutorado) — California Institute of Technology, Jul 1996. Cited on page 14.

- 55 POSCHEL, T. S. T. **Computational Granular Dynamics**. Springer, 2009. Disponível em: <<http://search.barnesandnoble.com/Computational-Granular-Dynamics/Thorsten-Poschel/e/9783540214854>>. Cited 3 times on pages 14, 17, and 20.
- 56 THOMPSON, W. On the elasticity and viscosity of metals. **Proc. Roy. Soc. London**, v. 14, p. 289–297, Jan 1865. Cited on page 16.
- 57 VOIGT, W. Ueber innere reibung fester Körper, insbesondere der metalle. **Annalen der Physik**, v. 283, p. 671–693, 1892. Cited on page 16.
- 58 LANDAU, L. et al. **Theory of Elasticity**. Butterworth-Heinemann, 1986. (Course of theoretical physics). ISBN 9780750626330. Disponível em: <<http://books.google.com.br/books?id=tpY-VkwCkAIC>>. Cited on page 17.
- 59 VERLET, L. Computer "experiments" on classical fluids. i. thermodynamical properties of lennard-jones molecules. **Phys. Rev.**, American Physical Society, v. 159, p. 98–103, Jul 1967. Disponível em: <<http://link.aps.org/doi/10.1103/PhysRev.159.98>>. Cited on page 19.
- 60 MARTINS, G. H. B.; ATMAN, A. P. F. Methods of parallel computation applied on granular simulations. **EPJ Web Conf.**, v. 140, p. 15024, 2017. Cited on page 20.
- 61 ROSATO, A. et al. Why the brazil nuts are on top: Size segregation of particulate matter by shaking. **Phys. Rev. Lett.**, American Physical Society, v. 58, p. 1038–1040, Mar 1987. Cited 2 times on pages 24 and 25.
- 62 ELPERIN, T.; GOLSHTEIN, E. Effects of convection and friction on size segregation in vibrated granular beds. **Physica A**, Elsevier, v. 247, n. 1, p. 67–78, Dec 1997. Cited on page 24.
- 63 HEJMADY, P. et al. Scaling behavior in the convection-driven brazil nut effect. **Phys. Rev. E**, American Physical Society, v. 86, p. 050301, Nov 2012. Disponível em: <<https://link.aps.org/doi/10.1103/PhysRevE.86.050301>>. Cited 3 times on pages 24, 26, and 27.
- 64 NAHMAD-MOLINARI, Y.; CANUL-CHAY, G.; RUIZ-SUÁREZ, J. C. Inertia in the brazil nut problem. **Phys. Rev. E**, American Physical Society, v. 68, p. 041301, Oct 2003. Disponível em: <<https://link.aps.org/doi/10.1103/PhysRevE.68.041301>>. Cited 4 times on pages 24, 25, 26, and 30.
- 65 CLEMENT, C. P. et al. The water-enhanced brazil nut effect. **EPL (Europhysics Letters)**, v. 91, n. 5, p. 54001, 2010. Disponível em: <<http://stacks.iop.org/0295-5075/91/i=5/a=54001>>. Cited 2 times on pages 24 and 26.
- 66 MÖBIUS, M. E. et al. Brazil-nut effect: Size separation of granular particles. **Nature**, Nature Publishing Group, v. 414, n. 6861, p. 270, nov. 2001. ISSN 0028-0836. Disponível em: <<http://dx.doi.org/10.1038/35104697>>. Cited 2 times on pages 25 and 27.
- 67 SCHNAUTZ, T. et al. A horizontal brazil-nut effect and its reverse. **Phys. Rev. Lett.**, American Physical Society, v. 95, p. 028001, Jul 2005. Disponível em: <<https://link.aps.org/doi/10.1103/PhysRevLett.95.028001>>. Cited 2 times on pages 26 and 29.
- 68 GARZÓ, V. Brazil-nut effect versus reverse brazil-nut effect in a moderately dense granular fluid. **Phys. Rev. E**, American Physical Society, v. 78, p. 020301, Aug 2008. Disponível em: <<https://link.aps.org/doi/10.1103/PhysRevE.78.020301>>. Cited on page 26.

- 69 CHUJO, T. et al. Categorization of brazil nut and its reverse under less-convective conditions for microgravity geology. **Royal Astronomical Society**, v. 474, n. 4, p. 4447–4459, 2018. Disponível em: <<https://academic.oup.com/mnras/article/474/4/4447/4683254>>. Cited on page 26.
- 70 BRITO, R.; SOTO, R. Competition of brazil nut effect, buoyancy, and inelasticity induced segregation in a granular mixture. **The European Physical Journal Special Topics**, v. 179, n. 1, p. 207–219, Dec 2009. ISSN 1951-6401. Disponível em: <<https://doi.org/10.1140/epjst/e2010-01204-5>>. Cited on page 26.
- 71 Quinn, P. V. et al. Comment on "reverse Brazil nut problem: Competition between percolation and condensation" (multiple letters). **Phys. Rev. Lett.**, v. 89, n. 18, p. 1, 2002. Disponível em: <<http://dx.doi.org/10.1103/PhysRevLett.89.189603>>. Cited on page 26.
- 72 IDLER, V. et al. Reverse buoyancy in a vibrated granular bed: Computer simulations. **The European Physical Journal E**, v. 35, n. 10, p. 106, Oct 2012. ISSN 1292-895X. Disponível em: <<https://doi.org/10.1140/epje/i2012-12106-x>>. Cited on page 26.
- 73 BREU, A. P. J. et al. Reversing the brazil-nut effect: Competition between percolation and condensation. **Phys. Rev. Lett.**, American Physical Society, v. 90, p. 014302, Jan 2003. Disponível em: <<https://link.aps.org/doi/10.1103/PhysRevLett.90.014302>>. Cited 2 times on pages 26 and 28.
- 74 TRUJILLO, L.; ALAM, M.; HERRMANN, H. J. Segregation in a fluidized binary granular mixture competition between buoyancy and geometric forces. **EPL (Europhysics Letters)**, v. 64, n. 2, p. 190–196, 2003. Disponível em: <<http://iopscience.iop.org/article/10.1209/epl/i2003-00287-1>>. Cited 2 times on pages 26 and 28.
- 75 GUTIÉRREZ, G. et al. Simple model for reverse buoyancy in a vibrated granular system. **EPL (Europhysics Letters)**, IOP Publishing, v. 67, n. 3, p. 369, 2004. Cited on page 26.
- 76 ALAM, M.; TRUJILLO, L.; HERRMANN, H. J. Hydrodynamic theory for reverse brazil nut segregation and the non-monotonic ascension dynamics. **Journal of Statistical Physics**, v. 124, p. 1572–9613, Aug 2006. Cited on page 26.
- 77 GAJJAR, P. et al. Size segregation of irregular granular materials captured by time-resolved 3d imaging. **Scientific Reports**, v. 11, p. 8352–8357, Apr 2021. Cited on page 26.
- 78 KUMAR, N.; RAMASWAMY, S.; SOOD, A. Symmetry properties of the large-deviation function of the velocity of a self-propelled polar particle. **Physical Review Letters**, APS, v. 106, n. 11, p. 118001, Mar 2011. Cited 2 times on pages 26 and 39.
- 79 MARTINS, G. H. B. et al. Large-deviation quantification of boundary conditions on the brazil nut effect. **Phys. Rev. E**, American Physical Society, v. 103, p. 062901, Jun 2021. Cited 9 times on pages 30, 31, 32, 35, 36, 37, 38, 39, and 40.
- 80 BOYCE W.E. E DIPRIMA, R. **Elementary Differential Equations and Boundary Value Problems**. [S.I.]: John Wiley and Sons, 1977. Cited 2 times on pages 44 and 101.
- 81 DURÁN, O.; ANDREOTTI, B.; CLAUDIN, P. Numerical simulation of turbulent sediment transport, from bed load to saltation. **Physics of Fluids**, American Institute of Physics, v. 24, 2012. Cited 6 times on pages 48, 49, 53, 56, 97, and 99.

- 82 MAURIN, R. **Investigation of granular behavior in bedload transport using an Eulerian-Lagrangian model.** Tese (Doutorado) — Université Grenoble Alpes, Dec 2015. Cited 2 times on pages 49 and 97.
- 83 MALISKA, C. **Transferência de calor e mecânica dos fluidos computacional: fundamentos e coordenadas generalizadas.** LTC, 1995. Disponível em: <https://books.google.com.br/books?id=Ifo_MwEACAAJ>. Cited on page 50.
- 84 HAMMING, R. W. **Numerical Methods for Scientists and Engineers (2Nd Ed.).** New York, NY, USA: Dover Publications, Inc., 1986. ISBN 0-486-65241-6. Cited on page 50.
- 85 PRESS, W. H. et al. **Numerical Recipes 3rd Edition: The Art of Scientific Computing.** 3. ed. New York, NY, USA: Cambridge University Press, 2007. ISBN 0521880688, 9780521880688. Cited on page 50.
- 86 MORTON, K. W.; MAYERS, D. F. **Numerical Solution of Partial Differential Equations.** 2. ed. New York, NY, USA: Cambridge University Press, 2005. ISBN 0511111622, 9780511111624. Cited on page 50.
- 87 PATANKAR, S. **Numerical Heat Transfer and Fluid Flow.** Hemisphere Publishing Corporation, 1980. (Electro Skills Series). ISBN 9780070487406. Disponível em: <<https://books.google.com.br/books?id=N2MVAQAAIAAJ>>. Cited on page 52.
- 88 ANDREOTTI, B. et al. Bedforms in a turbulent stream: ripples, chevrons and antidunes. **J. Fluid Mech.**, Cambridge University Press, v. 690, p. 94–128, 2012. Cited on page 55.
- 89 CREED, M. J. et al. A finite volume shock-capturing solver of the fully coupled shallow water-sediment equations. **International Journal for Numerical Methods in Fluids**, Wiley Online Library, 2017. Cited on page 55.
- 90 CHARRU, F.; ANDREOTTI, B.; CLAUDIN, P. Sand ripples and dunes. **Ann. Rev. Fluid Mech.**, Lund University Libraries, v. 45, p. 469–493, 2012. Cited on page 56.
- 91 DURÁN, O.; CLAUDIN, P.; ANDREOTTI, B. Direct numerical simulations of aeolian sand ripples. **PNAS**, v. 111, p. 15665–15668, Nov 2014. Cited on page 56.

APPENDIX

Appendix A – Artigos publicados

A seguir os artigos publicados desde o início desta pesquisa. O primeiro artigo apresentado refere-se a publicação feita sobre este doutoramento, com resultados mistos das técnicas utilizadas na dissertação de mestrado [50] e este projeto de tese. O segundo e terceiro artigos apresentados referem-se a publicações feitas durante a dissertação, mas que expressam as técnicas utilizadas neste projeto de tese.

A.1 *Large-deviation quantification of boundary conditions on the Brazil nut effect*

This paper was published on the Physical Review E, and it is one of the main themes of this thesis, referring to chapter 4.

A.2 *Methods of parallel computation applied on granular simulations*

Este artigo foi publicado no quatrienal do congresso *Powders & Grains 2017*, que é o maior congresso sobre materiais granulares, e que está em sua 8^a edição.

Methods of parallel computation applied on granular simulations

Gustavo H. B. Martins^{1,*} and Alibens P. F. Atman^{1,2,3, **}

¹Programa de Pós-Graduação em Modelagem Matemática e Computacional - PPG-MMC, Centro Federal de Educação Tecnológica de Minas Gerais, CEFET-MG, Av. Amazonas 7675, 30510-000, Belo Horizonte, MG, Brazil.

²Physics and Mathematics Department, Centro Federal de Educação Tecnológica de Minas Gerais, CEFET-MG, Av. Amazonas 7675, 30510-000, Belo Horizonte, MG, Brazil.

³Instituto Nacional de Ciência e Tecnologia de Sistemas Complexos (INCT-SC).

Abstract. Every year, parallel computing has become cheaper and more accessible. As consequence, applications were spreading over all research areas. Granular materials is a promising area for parallel computing. To prove this statement we study the impact of parallel computing in simulations of the BNE (Brazil Nut Effect). This property is due the remarkable arising of an intruder confined to a granular media when vertically shaken against gravity. By means of DEM (Discrete Element Methods) simulations, we study the code performance testing different methods to improve clock time. A comparison between serial and parallel algorithms, using OpenMP® is also shown. The best improvement was obtained by optimizing the function that find contacts using Verlet's cells.

1 Introduction

Granular materials have high relevance in Nature as well in humans activities like in mining, in food industry, in construction technology [3–9]. Basically, granular materials are everywhere, from sand to snow, from iron ore pellets to corn grains, from dust to stones. This ubiquity justify the high importance to know their behavior in order to use and manipulate them under different situations.

Several phenomena displayed by granular materials are quite surprising, and in general is a very difficult task to predict the behavior of a substantial quantity of granular material subjected to external loading, a very common situation. Perform experiments under controlled environment is the most desired approach to acquire knowledge about these systems, but most of time only with a detailed modeling of the system is possible to verify theoretical hypothesis. Thus, it is essential to develop a reliable computational model able to predict and reproduce granular behavior under different situations, and increasing system sizes.

Given the importance and presence of granular materials in the world, simulations offer lots of advantages for testing possible characteristic states, to predict behaviors, to save money in execution of projects, and to help plan next moves in engineering for instance. But some disadvantages may be present also, as the increasing of computation time for large systems sizes. With the increasing number of agents in simulation, higher is the computation

time. Most cases, this increasing relation is quadratic in time because the nature of operations.

To improve simulations, and save time, more than one machine can execute the tasks at same time. Parallelization can solve single parts of the problem separately and get them together as part of the final solution, saving total operation time. Also, many researchers are using parallel computation resources in scientific programs to simulate DEM in particles systems [1, 2]. These DEMs are commonly used to simulate different kind of systems, like dense granular materials.

Is possible to perform parallelization in clusters of pc's or multicore computers, since they have more than one CPU (Central Processing Unit) available, that exchange information between them. In the model we use, some operations can be done separately, each one in one processor. More processors used, generally result in lower total execution time from a given job. The increasing number of cores in processors nowadays has turned this possibility very accessible. Also, GPUs (Graphics Processing Units) are becoming a cheaper option to improve a lot computational power.

Given all these possibilities to improve simulations, we propose to measure different techniques to simulate a paradigmatic example of granular system, the Brazil Nut Effect (BNE), and compare the performance of the algorithms. The BNE is a typical segregation phenomena observed in granular materials, which still have several open issues to be explored by simulations. We present results of BNE with frictional and frictionless walls.

In section 2, the methodology to simulate the system is shown, with different proposals to improve the time spent

*e-mail: gmartins@adm.cefetmg.br

**e-mail: atman@dppg.cefetmg.br

on serial and parallel algorithms, and some results. In section 3, the BNE results using these codes. In section 4, the main conclusions we got from our experiments.

2 Methods to save time in simulations

To simulate granular systems computationally, some models can be used [10]. One of this models considers rigid grains which are allowed to display some degree of interpenetrations, which are used in Kelvin-Voight rheology model, Cundal-Strack elastic contact in normal directions, and Coulomb friction in tangent direction, as shown in figure 1. By this, MD (Molecular Dynamics, that is a DEM) can be used [10–12] to integrate the motion equations of the grains directly from Newtons' laws. By choosing an appropriated time step, several different methods can be used to integrate these equations.

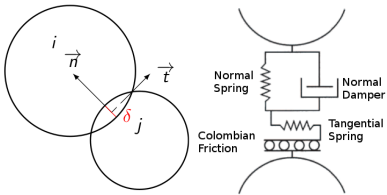


Figure 1. Force model between grain's interactions. i and j are particles that have contact each other. δ is the interpenetration value between the contact ij . n is the direction of the normal contact force. t is the direction of the tangential friction force.

In MD, a predictor-corrector method is used, and its scheme can be seen in Figure 2. The routine *Predict states* solves the kinematic equations over all grains over a single step. The routine *Detect contacts* find grains in contacts each other and store into a list. For the implementation without routine *Set list of neighbors*, *Detect contacts* look for all possible pair of grains for contacts, at every time step, and requires two loops over all grains. Otherwise, *Detect contacts* focus the search to the list of neighbor grains, and require one loop over the neighbor list. Both cases, it is produced a list of contacts, with the predicted states. The routine *Calculate forces* calculate the contact forces and also gravitational, requiring one loop over all particles and one loop over the list of contacts. The routine *Correct predicted states* corrects the predicted states and requires one loop over all particles. If the routine *Set list of neighbors* have Verlet's list implemented, it will search all possible pairs of neighboring grains, and requires two loops over all grains with a given frequency. If the routine *Set list of neighbors* have Verlet's cells implemented, it will search all neighbors grains' dividing the space in regions and look for possobli pair of contact grains only inside a cell and its neighboring cells. It requires one loop over all grains and other over all grains in the cells' neighbors.

To parallelize the simulation, all barriers should be identified to do a proper implementation. The first barrier is a temporal barrier, and happens in simulation each step. This first barrier can't be jumped by the temporal

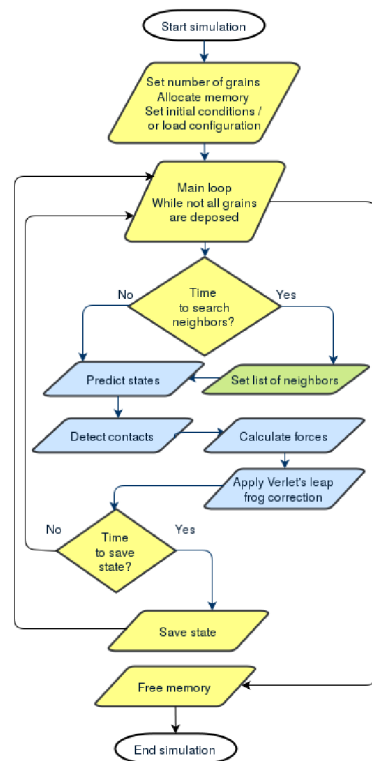


Figure 2. Flowchart of the simulation to simulate granular system using MD. Yellow operations can't be parallelized. Blue operations can be parallelized using CPUs. Green operation is the function that consume most processing, and can be parallelized based onto the type of implementation: *Set list of neighbors* as Verlet's list is the first improvement to reduce time in simulations. *Set list of neighbors* as Verlet's cells is the second improvement to reduce time in simulations.

dependency of the system, as future depends on all past calculation done. Each particle can be treated independently, and at that point, the following routines *Predict states*, *Detect contacts*, *Correct predicted states* and *Set list of neighbors*, using Verlet's list, have no barrier to parallelize, so all loops were done to distribute all calculations to each processor available independently to read and write on memory. In the routine *Set list of neighbors*, using none of Verlet's improvement, the *Set list of neighbors* have no function, once all time steps the contact is calculated inside *Detect contacts*, and no barrier is present in parallelization. If the routine *Set list of neighbors* is using Verlet's cells, one barrier happens to insert grains in the cell it belongs, because to write on one same cell, two processors may try to do at same time. In the routine *Calculate forces* a barrier may happen, depending on implementation. If the 3rd Newton's law is applied on both bodies at same computational sequence when one contact happen, a barrier should be present to prevent memory concurrency by two or more contacts in a particle. This implementation gives an advantage of computation in serial execution that reduces the calculation by half, but a disadvantage in parallel execution by one barrier. The way done here is to calculate the pair of action and reaction separately, in each particle's loop.

The most expansive routine is detect contacts that searches all grains in contact each other, and its computational complexity can be written in function of the number of grains (n), as $O(n^2)$ with Verlet's list, and $O(n \log n)$ with Verlet's cells. Other routines have computational complexity $O(n)$. So, the total complexity of this algorithm can be written as $O(n^2)$ for Verlet's list, and $O(n \log n)$ for Verlet's cells.

2.1 Time spend

The clock time to simulate the system depends on the number of particles, the number of steps the system is simulated, the dynamic of the grains, the number of process running on the machine or cluster, the machine or cluster itself, the method used to implement the solution and many other controllable and uncontrollable variables.

To have an optimized parallel code, one need to know how much time serial functions costs, and their parallelizable portion. The results of time spent by each routine, in seconds, can be found on table 1, table 2 and table 3. The function *Detect contact* is the one which displays best results for application of parallization algorithm. In fact, Verlet's list and Verlet's cells are optimizations for the search algorithm. Both saves computational time and store closer grains into one list. The system do not update the neighbor list all steps of simulation, but only at a given frequency.

Table 1 shown the profile of serial runs of the code with 10^3 grains. For this number of grains, Verlet's cells and Verlet's list have little impact on execution times, but the simple search is the slowest, as expected. Table 2 have the profile of serial running of the code for 10^4 grains, and at this number of grains, Verlet's cells are faster than Verlet's list. Table 3 have the profile of serial running of the code for 10^5 grains, only for Verlet's list and Verlet's cells, because the simplest implementation got no result running after one week with this number of grains, and Verlet's cells are still faster than Verlet's list.

To compare and understand the parallelization, some metrics are defined. One of them is the performance of the system, that is the clock time measured by running that code. Faster codes gives lower results. Our results of performance can be found in figure 3, and for simulations with number of grains higher than 10^3 , Verlet's cells gives best results.

The speedup is the comparison between clock time of execution in serial and the clock time of execution in parallel of same algorithm. It gives the tendency of the parallelization of the code. Best results gives higher curves. Our results of speedup, shown in figure 4, evince that parallelization decreased clock time to perform simulations above than 10^3 particles in the system. We can also conclude that *Detect contacts* without Verlet's implementations and Verlet's list are much more parallelizable than Verlet's list.

The efficiency is the comparison between speedup and the number of processors used. It gives the average utilization of each processor in the algorithm. Best results tends

Table 1. Clock time spent, in seconds, on each routine of serial running of the code for 10^3 grains for 10^3 time steps.

Function	Simplest	List	Cells
Predict states	0.01	0.03	0.03
Detect contact	22.47	0.15	0.18
Calculate forces	0.01	0.01	0.01
Correct states	0.01	0.04	0.02
List of neighbors	--	0.22	0.01

Table 2. Clock time spent, in seconds, on each routine of serial running of the code for 10^4 grains for 10^3 time steps.

Function	Simplest	List	Cells
Predict states	0.27	0.19	0.21
Detect contact	2048	1.98	1.84
Calculate forces	0.09	0.06	0.05
Correct states	0.27	0.34	0.30
List of neighbors	--	23.18	0.05

Table 3. Clock time spent, in seconds, on each routine of serial running of the code for 10^5 grains for 10^3 time steps.

Function	Simplest	List	Cells
Predict states	--	2.93	2.87
Detect contact	--	19.87	19.77
Calculate forces	--	0.93	0.86
Correct states	--	3.87	3.73
List of neighbors	--	2,322.96	0.59

to have value 1, the full use of each processor. Figure 4 shown us that *Detect contacts* without Verlet's implementations and Verlet's list uses more the computational resources at same time than Verlet's cells implementation. For higher number of grains, they occupy more the computational resources, justifying the good use of parallelization with large systems.

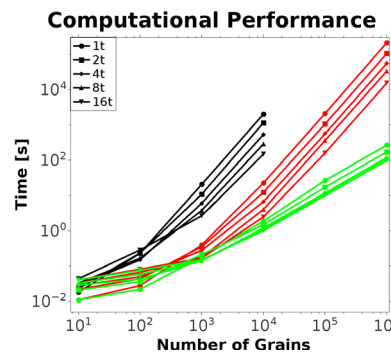


Figure 3. Performance of the system. This compares the results without Verlet's methods (in black), Verlet's list (in red) and Verlet's cells (in green). The number of processors used to simulate varies from 1 to 16, indicated on the legend.

3 Brazil Nut Effect (BNE)

The system has been validated comparing results with the theory of BNE [8, 9, 13, 14]. BNE is a segregation phe-

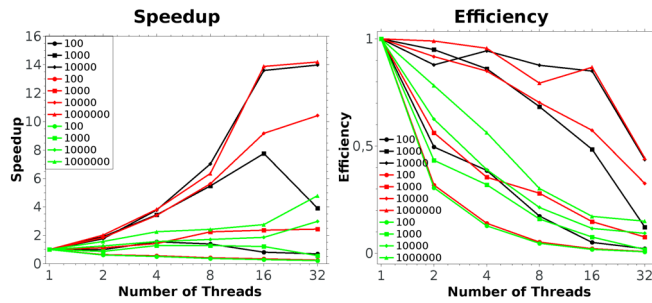


Figure 4. Speedup and Efficiency of the system. This compares the results without Verlet's methods (in black), Verlet's list (in red) and Verlet's cells (in green). The number of grains used to simulate varies from 100 to 1000000, indicated on the legend.

nomena which occurs when a system is shaken and a grain which is larger than the other grains in the media, rises to the surface. Friction is also an important influence to BNE, as can be seen in Figure 5, the larger grain rises in both cases for dimensionless accelerations higher than 1.00, but comparing friction walls with frictionless walls, the intruder with friction walls rises much more than the one without friction.

The parameters of the simulated system were: 2500 grains, uniform polydispersion of the radius of grains around 5%, friction coefficient of 0.5 between grains, and between grains and walls, normal spring stiffness of 1000 adimensional unities [3], tangential spring stiffness of 750 a.u., the radius of the intruder equals 3 times the radius of the larger grains in the media, density of the system equals to π^{-1} in a. u., critical damping coefficient in normal direction, time step of one tenth of the typical colision time for the smallest grains in the system. An imposed sinusoidal force is submitted to the box at 2500 a.u. and the dimensionless acceleration, $\Gamma = A\omega^2/g$, is varying between 0.85 to 1.5.

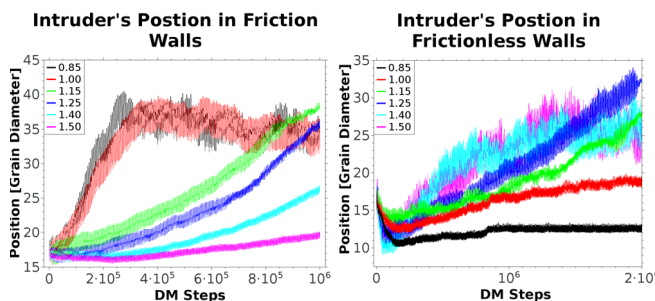


Figure 5. BNE with different amplitudes on the vibration. At left, grains have friction with walls. At right, walls have no friction.

4 Conclusions

We have presented the performance of serial and parallel MD code to simulate granular systems, with 3 different

implementations on the computational function that costs most. The implementation that shown best performance was Verlet's cells, and parallelization present higher gain with increasing number of grains. The BNE simulations evince that intruder's ascension is faster and get higher stationary positions when friction is present at grains and walls.

Acknowledgements

We thanks to CEFET-MG that gives us materials and conditions to develop our research. Special thanks to CEFET-MG, FAPEMIG, CAPES and CNPq for funding the research.

References

- [1] Radeke, Charles A. and Glasser, Benjamin J. and Khinast, Johannes G., *Chemical Engineering Science* **65**, 6435-6442 (2010).
- [2] Cruz-Hidalgo, Raúl and Kanzaki, T. and Alonso-Marroquin, F. and Luding, S., *Powders and Grains 2013 AIP Conference Proceedings* **1542**, 169-172 (2013).
- [3] Atman, A. P. F. and Claudin, P. and Combe, G., *Computer Physics Communications* **180**, 612–615 (2009).
- [4] Andreotti, B. and Forterre Y. and Pouliquen O., *Granular Media: Between Fluid and Solid* (Cambridge University Press, São Paulo, 2013).
- [5] Atman, A. P. F. and Claudin, P. and Combe, G. and Martins, G. H. B., *Granular Matter* **16** 193-201 (2014).
- [6] J. Duran, A. Reisinger, and P. de Gennes, *Sands, Powders, and Grains: An Introduction to the Physics of Granular Materials* (Springer, New York, 1999).
- [7] Atman, A. P. F. and Kolb, E. and Combe, G. and Paiva, H. A. and Martins, G. H. B., *Powders and Grains 2013 AIP Conference Proceedings* **1542**, 381-384 (2013).
- [8] Mehta, A., *Granular Physics* (Cambridge University Press, São Paulo, 2007).
- [9] Herrmann, H. and Hovi J. and Luding S., *Physics of Dry Granular Media* (Springer, Netherlands, 2013).
- [10] Pöschel, T. and Schwager, T., *Computational Granular Dynamics: Models and Algorithms* (Springer, Berlin Heidelberg, 2005).
- [11] Allen, M. P. and Tildesley, D. J., *Computer Simulation of Liquids* (Clarendon Press, Oxford, 1991).
- [12] Hedman, Fredrik, *Algorithms for Molecular Dynamics Simulations* (Institutionen för fysikalisk kemi, oorganisk kemi och strukturkemi, 2006).
- [13] Gutiérrez, G. and Pozo, O. and Reyes, L. I. and Drake, J. F. and Ott, E. and others, *Europhysics Letters* **67**, 369-372 (2004).
- [14] Brito, R. and Soto, R., *The European Physical Journal Special Topics* **179**, 207-219 (2009).

A.3 *Mechanical properties of inclined frictional granular layers*

Este artigo foi publicado na *Granular Matter*, uma das maiores revistas sobre material granular e é uma revista A2 segundo a classificação *qualis* da CAPES e possui fator de impacto de 1,762.

Mechanical properties of inclined frictional granular layers

A. P. F. Atman · P. Claudin · G. Combe ·
G. H. B. Martins

Received: 8 July 2013 / Published online: 29 January 2014
© Springer-Verlag Berlin Heidelberg 2014

Abstract We investigate the mechanical properties of inclined frictional granular layers prepared with different protocols by means of DEM numerical simulations. We perform an orthotropic elastic analysis of the stress response to a localized overload at the layer surface for several substrate tilt angles. The distance to the unjamming transition is controlled by the tilt angle α with respect to the critical angle α_c . We find that the shear modulus of the system decreases with α , but tends to a finite value as $\alpha \rightarrow \alpha_c$. We also study the behaviour of various microscopic quantities with α , and show in particular the evolution of the contact orientation with respect to the orthotropic axes and that of the distribution of the friction mobilisation at contact.

Keywords Granular systems · Elasticity · Jamming · DEM simulations

A. P. F. Atman

Departamento de Física e Matemática and National Institute of Science and Technology for Complex Systems, Centro Federal de Educação Tecnológica de Minas Gerais (CEFET-MG), Av. Amazonas 7675, Belo Horizonte, MG 30510-000, Brazil
e-mail: atman@dppg.cefetmg.br

P. Claudin (✉)

Laboratoire de Physique et Mécanique des Milieux Hétérogènes (PMMH), Univ. Paris Diderot, UMR 7636 CNRS, ESPCI, Univ. P. et M. Curie, 10 rue Vauquelin, 75231 Paris Cedex 05, France
e-mail: claudin@pmmh.espci.fr

G. Combe

UJF-Grenoble 1, Grenoble-INP, CNRS UMR 5521, 3SR Lab., B.P. 53, 38041 Grenoble Cedex 09, France
e-mail: gael.combe@ujf-grenoble.fr

G. H. B. Martins

Departamento de Física e Matemática, Centro Federal de Educação Tecnológica de Minas Gerais (CEFET-MG), Av. Amazonas 7675, Belo Horizonte, MG 30510-000, Brazil

1 Introduction

The nature of the jamming transition in granular systems has been investigated during the last decade, see recent reviews [29, 45]. Many studies have focused on frictionless discs or spheres, typically controlled in volume fraction ϕ or in pressure P [30, 32, 33], showing that the jamming transition is critical (scaling exponents, diverging length scale) [14, 32, 46] and related to isostaticity [1–3, 31, 32, 37, 44]. As the system loses its mechanical rigidity at the transition, its shear modulus G is found to vanish as a power law with respect to the distance to jamming $\phi - \phi_c$, where ϕ_c is the critical volume fraction. The properties of frictional granular packings have also been investigated, see e.g. [40], but, in this context of elastic properties close to jamming, most of the studies have considered homogeneous systems under isotropic pressure [1–3, 11, 22, 23, 39, 42, 47]. In the frictional case, the Liu-Nagel jamming concept [27, 28] must be revised [9]. In particular, jamming and isostatic points do not coincide any more [45], and one thus can expect a finite shear modulus at the transition.

In this paper, we consider static layers of frictional grains under gravity, by means of two-dimensional discrete element simulations (standard Molecular Dynamics [36]), and investigate their mechanical properties through the analysis of their stress response to a localized overload \mathbf{F}_0 at the layer surface, a technique particularly developed by and dear to R.P. Behringer, see e.g. [5, 16]. Expanding the work published in [8], we present here the detailed analysis of layers prepared with three different protocols. The outline is as follows. We first describe the numerical system, its preparation and the computation of the stress response. In the next section, we present an orthotropic elastic analysis of the stress profiles, and detail the fitting procedure. Then, a section is

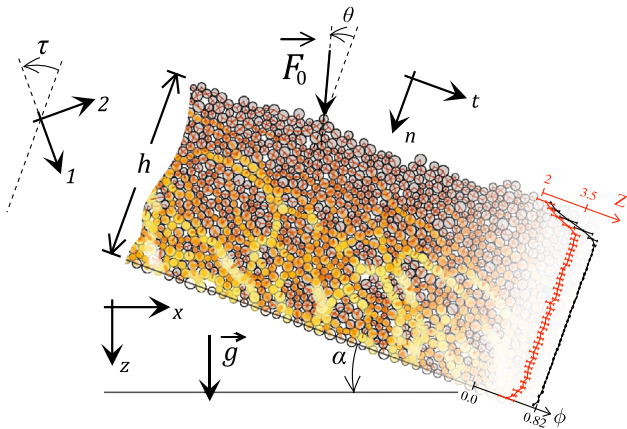


Fig. 1 System set-up and notations. x is the horizontal axis. z is the vertical one, along which acts gravity \mathbf{g} . The granular layer (here GG preparation), of average thickness h , is inclined at an angle α with respect to horizontal. t and n are the axis respectively tangential and normal to the layer. A localized force \mathbf{F}_0 , which makes an angle θ with respect to n , is applied on a grain close to the surface of the layer. The stress responses σ_{nn} and σ_{tn} to this overload are measured at the bottom of the layer (fixed grains in white). Axis $(1, 2)$, making an angle τ with respect to (n, t) , are those of the orthotropic elastic analysis. Black line volume fraction profile $\phi(n)$. Red line coordination number profile $Z(n)$. These are for the GG preparation. *Orangish colors* on grains: force chains (color figure online)

devoted to the measure and the interpretation of the microscopic data. Finally, conclusions and perspectives are drawn.

2 Numerical simulations

2.1 Numerical model and set-up

The numerical model is that described in [5, 18], with $N=3,600$ polydisperse frictional discs coupled, when overlapping, by normal and tangential linear springs, tangential forces being limited by the Coulomb condition with a friction coefficient $\mu = 0.5$. The typical thickness of the layer is $h \simeq 23$ grain diameters, i.e. a system aspect ratio around $1/6$. The layers are prepared at a *fixed* angle α with respect to the horizontal (see Fig. 1 for notations), and unjamming is approached as α is close to α_c , the critical value above which static layers cannot be equilibrated at that angle and always flow. Note that this unjamming point α_c is close in spirit to the situation of a jammed solid sheared up to its yield-stress [24]. It is also close, but different, to progressively tilted granular layers, which eventually loose their mechanical stability, see e.g., [21, 43].

In our simulations, the volume fraction in the layer is fairly uniform all through the layer depth (see Fig. 1) and roughly independent on the inclination angle. The control parameter for the jamming/unjamming transition is then the sole angle α . This situation is therefore qualitatively different to the homogeneous configurations submitted to isotropic pres-

sure cited above, and is effectively closer to an experimental set-up. No external pressure applied to the topmost layer of particles, i.e. the pressure in the system is due solely to the gravitational force acting on the particles themselves.

2.2 Three preparation protocols

Three different system preparations have been carried out: a grain-by-grain (GG), a rain-like (RL) and an avalanched (AV) deposition of the particles on a rough substrate consisting of fixed but size-distributed particles, inclined at the desired angle α . In the GG protocol, grains are added to the layer one after the other, with no initial velocity, at random t -positions and in contact with those already deposited. The time lag between two successive drops is sufficiently large to ensure the relaxation of the system before the next deposit. As for the RL preparation, all N grains are initially put at regular ‘flying’ positions above the bed, with no contact between the particles and no velocity. Then gravity is switched on, and they all fall down like a rain. Finally, for the AV preparation, we start from an initial steady and homogeneous flow running at a large inclination, then abruptly set the angle to the desired value of α and reduce the kinetic energy of the whole system. The layer is prepared when all grains have eventually reached static equilibrium (see [5] for more details).

Above a certain inclination α_c , these preparation procedures do not converge towards a static layer—the grains do not stop moving. The ‘solid-liquid’ transition occurs rather abruptly, over a typical inclination range $\Delta\alpha \simeq 0.5^\circ$ where only part of the simulations converge. This allows for a value of this critical angle defined at this precision. For both GG and AV preparations, we get $\alpha_c \simeq 20.8^\circ$. We have not studied systematically enough the RL preparation for inclinations around 20° to determine its critical angle with a good precision. However, we expect RL and AV data to be very similar close to α_c as in both cases the grains flow down the slope over long distances—typically several times the system size—before stopping, so that the initial configuration is effectively forgotten.

These three preparations mainly differ in their contact orientation (see Fig. 5). Their volume fractions does not vary much from $\alpha = 0^\circ$ to α_c . Typical values are $\phi \simeq 0.82$ for GG and $\phi \simeq 0.81$ for RL and AV. These are slightly larger than—or similar to—the critical value, estimated in our system at $\phi_c \simeq 0.81$ [12, 34, 39].

2.3 Stress response profiles

Once a layer is deposited, stabilized in an equilibrium state, an additional force \mathbf{F}_0 is applied on a grain close to the free surface, and a new equilibrium state is reached. Taking the difference between the states after and before the overload, one can compute the contact forces in response to \mathbf{F}_0 . Intro-

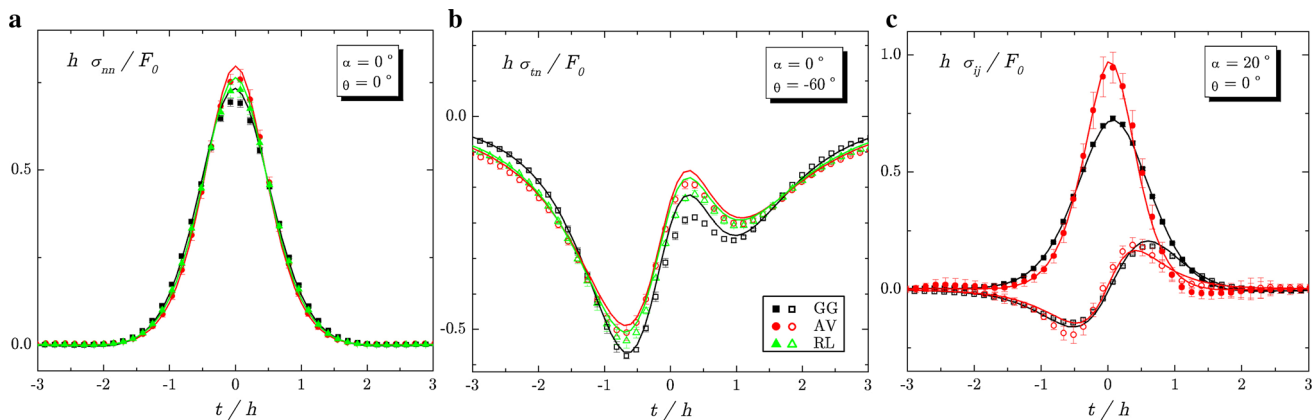


Fig. 2 Stress profiles for the different preparations. The layer inclination α and the overload angle θ are indicated in legend for each panel. Symbols numerical data (filled symbols σ_{nn} , empty symbols σ_{tn} , color

code see legend). Lines elastic fits (see Table 1 for the corresponding values of the fitting parameters) (color figure online)

Table 1 Values of the elastic parameters corresponding to the fits displayed in Fig. 2

$\alpha(^{\circ})$	Prep.	G/E_1	E_2/E_1	ν_{21}	$\tau(^{\circ})$
0	GG	0.403	0.80	0.20	93
	RL	0.303	0.69	0.23	93
	AV	0.275	0.71	0.26	91
20	GG	0.262	0.49	0.17	66
	AV	0.248	0.93	0.27	94

ducing a coarse graining length w , the corresponding stress response can be determined. Taking w of the order of few mean grain diameters (here $w = 6\langle d \rangle$) as well as an ensemble averaging of the data (here, for each tilt angle α , we average over 120–150 independent force loads, distributed on typically 10 layers in total), make the stress profiles quantitatively comparable to a continuum theory [18], such as elasticity, as discussed below. The amplitude of the overload was kept constant for all simulations: $F_0 = 1.0\langle m \rangle g$, where $\langle m \rangle$ is the average mass of the grains. This value is sufficiently small to ensure a linear [6, 7] and reversible response of the system for all values of α , including close to α_c .

Some examples of stress bottom profiles $\sigma_{nn}(t)$ and $\sigma_{tn}(t)$ are displayed in Fig. 2 for different values of the inclination α and of the angle θ that the overload force makes with the normal direction (see Fig. 1). Note that, as we deal with linear elasticity, the stresses can be rescaled by F_0/h . The normal stress data σ_{nn} show classical bell-shaped profiles, which do not differ much for all three preparations when the layer is horizontal ($\alpha = 0$) and the overload vertical ($\theta = 0$), see panel (a). However, one can distinguish between the preparations, especially GG from the two others, looking at the shear stress profiles σ_{tn} in response to a non-normal overload force ($\theta = -60^{\circ}$), see panel (b). The difference between GG and AV profiles is enhanced for the data at an inclination close to α_c , see panel (c).

3 Orthotropic elastic analysis

Experimental and numerical works have shown that the linear stress response of granular systems to a point force is well described by (possibly anisotropic) elasticity [4, 5, 17, 19, 20, 26, 38]. In this section, we introduce the framework of orthotropic elasticity, with which numerical response profiles such as those displayed in Fig. 2 can be fitted. The details of the computation of elastic response are available in “Appendix”.

3.1 Orthotropic elasticity

Orthotropic elasticity is characterized by a stiff axis (here labelled 1) and a soft one (labelled 2), associated to two Young moduli E_1 and $E_2 < E_1$, and to two Poisson coefficients ν_{12} and ν_{21} (note that, for symmetry reasons, $\nu_{12}/E_1 = \nu_{21}/E_2$). There is also a shear modulus G involved in the corresponding relation between stress and strain tensor components (Eq. 4). A last parameter of this modeling is the angle τ that the axes (1, 2) make with (n, t) (see Fig. 1).

Orthotropic stress responses to a point force \mathbf{F}_0 have been analytically computed in [35] for a semi-infinite medium ($h \rightarrow \infty$). For a given τ , they only depend on two combinations of the elastic parameters, noted R and T , (Eq. 14). For an elastic slab of finite layer thickness h , a semi-analytical integration, following the computation performed in [38] for isotropic elasticity, must be done (see “Appendix”). Rough bottom boundary conditions (zero displacement) are imposed. Besides the coefficients R and T , these bottom conditions involve a Poisson coefficient, say ν_{21} , so that, in total, five dimensionless numbers (τ , R , T , ν_{21} and θ) must be specified to produce the normalized bottom stress responses $\sigma_{ij}h/F_0$ as functions of the reduced tangential coordinate t/h .

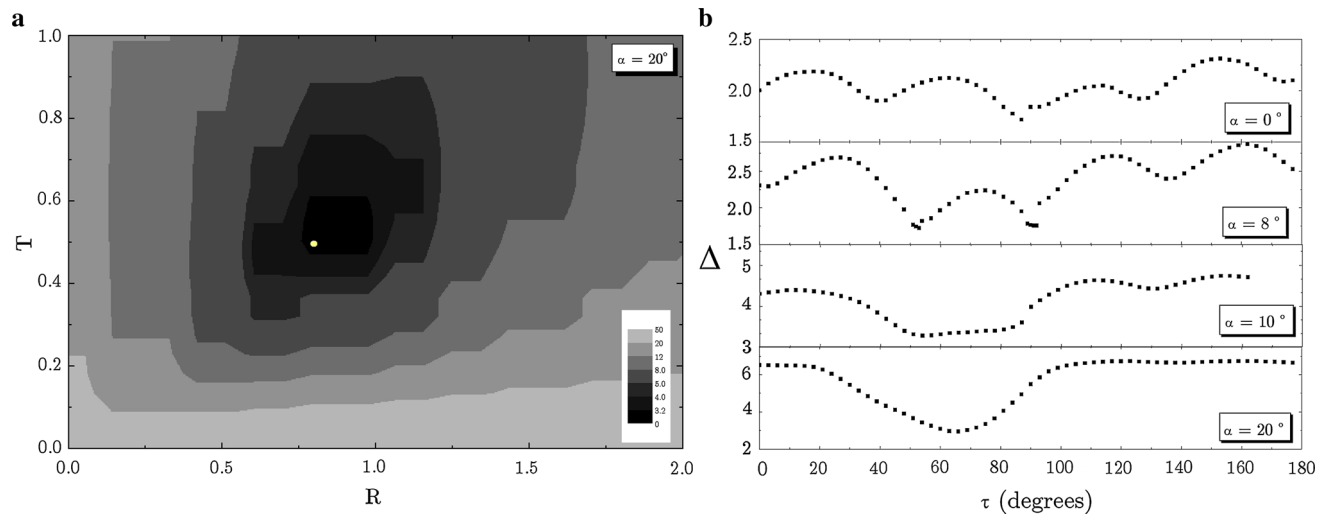


Fig. 3 Fitting technique. **a** Contour plot, in the \$(R, T)\$ parameter plane, of the normalized difference \$\Delta\$ (Eq. 1) between the numerical data and the elastic prediction. The other parameters are \$\nu_{21} = 0.15\$ and \$\tau = 66^\circ\$. The layer inclination is \$\alpha = 20^\circ\$. White bullet location of the best fit. **b**

Difference \$\Delta\$ as a function of the orthotropic angle \$\tau\$ for four values of \$\alpha\$ (see legends). These are GG data. For each of these points, all other parameters are also set to their best fitting values

3.2 Fitting numerical data

The idea is to fit the elastic response profiles to the numerical data, in order to extract the effective elastic parameters of the layer. For a given inclination \$\alpha\$, the four numbers \$\tau\$, \$R\$, \$T\$ and \$\nu_{21}\$ must be adjusted to reproduce at the same time the profiles measured for all three stress components \$\sigma_{nn}\$, \$\sigma_{tn}\$ and \$\sigma_{tt}\$, and for all overload angles \$\theta\$. This is achieved by minimizing the RMS difference

$$\Delta = \sqrt{\frac{1}{N_p} \sum_{\{i,j\}, \theta} \sum_{k=1}^{N_p} \left(\frac{\sigma_{ij}^k|_{\text{num}} - \sigma_{ij}^k|_{\text{elas}}}{\delta\sigma_{ij}^k} \right)^2}, \quad (1)$$

where \$N_p\$ is the number of data points in the profiles, and \$\delta\sigma_{ij}^k\$ is the standard deviation around the mean stress computed from the ensemble averaging.

An example of a contour plot of \$\Delta\$ in the \$(R, T)\$ plane, for given \$\tau\$ and \$\nu_{21}\$, is shown in Fig. 3a. There is a clear deepest point, which corresponds to the best fit. In Fig. 3b, we display \$\Delta\$ as a function of the orthotropic angle \$\tau\$, each point of these curves corresponding to the best fitting \$R, T\$ and \$\nu_{21}\$. These curves have been computed for the GG data at different inclination angles. It shows how the minimum, corresponding to the best fitting \$\tau\$, changes rather abruptly from \$\simeq 90^\circ\$ to \$\simeq 60^\circ\$ around \$\alpha \simeq 9^\circ\$ (see also next section and Fig. 5c).

Some of these fits are displayed in Fig. 2, for various angles \$\alpha\$ and \$\theta\$, and for the different preparations. The overall agreement between the elastic predictions and the numerical data is quantitatively good. In Fig. 4, we show the elastic modulus ratios \$G/E_1\$ and \$E_2/E_1\$ extracted from these fits, as func-

tion of the inclination. \$G/E_1\$ decreases with \$\alpha\$ but does not vanish close to the critical angle, in agreement with the observation that frictional granular systems remain hyperstatic at the unjamming transition [1–3, 23, 42]. Such a discontinuous behaviour at the transition has also been seen in simulations by Otsuki and Hayakawa [34] investigating the rheology of sheared frictional grains close to jamming, and in experimentally created shear-jammed states reported in [9]. The sudden drop of \$G/E_1\$ around \$\alpha \simeq 9^\circ\$ is associated with the change of the orthotropic directions mentioned above. The behaviour of \$E_2/E_1\$ also present an overall decrease with \$\alpha\$, except for the AV data close to \$\alpha_c\$. The complete interpretation of this behavior of the AV data is not entirely clear, but it is clearly related to an increase of friction mobilization at the contacts (see Figs. 5, 6 and discussion below).

4 Microscopic variables

In addition to the above global mechanical properties of the system, we have studied the evolution of various microscopic quantities with \$\alpha\$. The first one of interest is the coordination number \$Z\$, i.e. the average number of contacts per grain, here computed in the bulk of the layer, where it is fairly uniform—it obviously drops down close to the surface. \$Z\$ monotonously decreases with \$\alpha\$ for the GG preparation, while it stays approximately constant for RL and AV data (Fig. 5a). In all cases, it stays always far from the isostatic value \$Z_{\text{iso}} = 3\$ (for frictional grains in 2D). Grains of the bulk that only carry their own weight do not contribute much to the global stability of the contact network. As for so-called rattlers in gravity-free packings (see [13], chap. 6), these grains can be

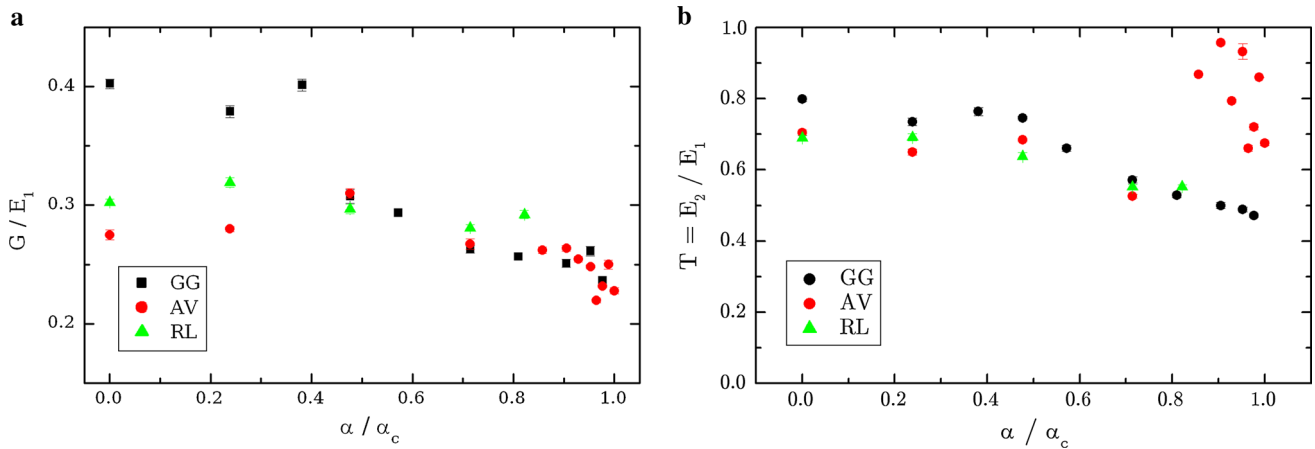


Fig. 4 Shear and Young moduli ratios G/E_1 (**a**) and E_2/E_1 (**b**) as functions of α/α_c . These data include all three preparations GG, RL and AV, see legend (color figure online)

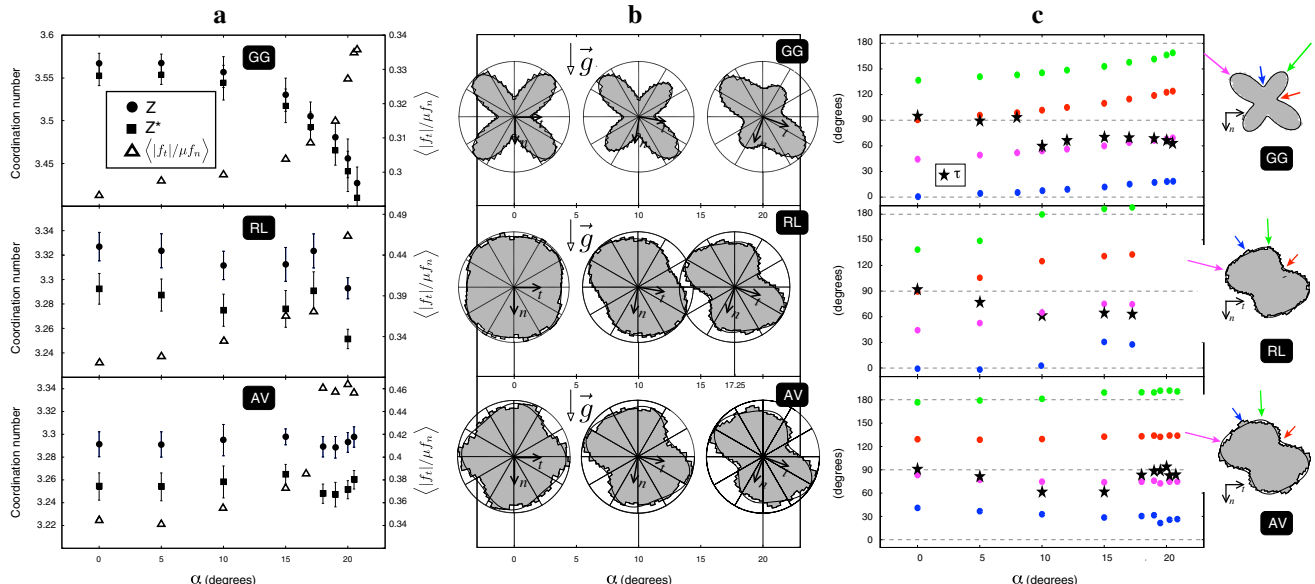


Fig. 5 Microscopic data for the three preparation protocols GG (top), RL (middle) and AV (bottom). **a** Coordination number Z (circle) and modified ('rattlers' removed) coordination number Z^* (square) as functions of the inclination of the layer α . Right y-axis: relative importance of the average friction mobilisation at contact (triangle). **b** Contact angle polar distributions at three inclination angles α . Solid black line fourth-

order Fourier fit. Gravity is vertical (black arrow). **c** Fitted orthotropic elastic angle τ as a function of α (star). The four characteristic angles of the contact angle distribution, computed with respect to the direction n , are also shown—these angles corresponds to the directions of the lobes, and those in between the lobes, see sketch and corresponding coloured arrows in legend (color figure online)

removed from the contact counting, leading to a modified coordination number of the layer Z^* (see Fig. 5a). However, we find that their number is roughly independent of α .

We have also studied the friction mobilisation at the contact level. In the MD simulations, the number of contacts with a ratio of the tangential force f_t to the normal force f_n strictly equal to the microscopic friction μ is zero when static equilibrium is reached. However, some of them are effectively close to the Coulomb criterion. We have first computed the average $\langle |f_t|/\mu f_n \rangle$. This quantity, displayed in Fig. 5a, increases as $\alpha \rightarrow \alpha_c$ for all three preparations, but its overall varia-

tion is weaker for the GG data (see right y-scales), as could be expected. More precisely, we also display in Fig. 6a, b the probability distribution function of the friction mobilisation at contact for the two preparations GG and AV, and for several inclinations. For the GG preparation, the distribution is only slightly skewed towards larger values of $|f_t|/\mu f_n$ when α is increased, but nothing particular happens close to $|f_t|/\mu f_n = 1$. For the AV preparation, however, a peak close to $|f_t|/\mu f_n = 1$ appears for $\alpha \gtrsim 18^\circ$, corresponding to quasi-sliding contacts. Figure 6d shows that they are uniformly distributed all through the layer depth. Following [23, 25, 41], we

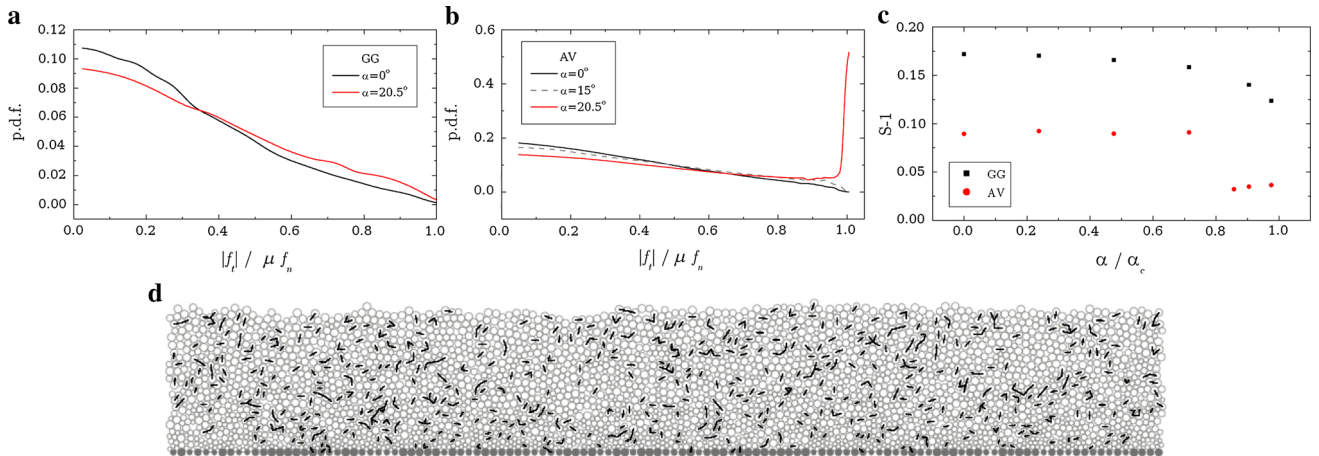


Fig. 6 Probability distribution function of the friction mobilisation at contact $|f_t|/(\mu f_n)$ for the GG (a) and the AV (b) preparations. The distributions for several values of α are displayed. For the AV preparation, the distribution at $\alpha = 18^\circ$ is not shown but is identical to that

at $\alpha = 20.5^\circ$. c Redundancy factor, as defined in [25], as a function of α/α_c . d Spatial distribution of quasi-sliding contacts (bold dashes) in an AV-layer at $\alpha = 20.5^\circ$ (color figure online)

have computed the redundancy factor S , i.e. the ratio of the total number of force degrees of freedom at contacts over the number of equilibrium equations, taking into account these quasi-sliding contacts: $S = (2n_c - n_s)/(3N)$, where n_c is the total number of contacts and n_s is the number of quasi-sliding contacts—recall the system is two-dimensional. We see that S decreases with α (see Fig. 6c), and, for the AV preparation, approaches 1 (the isostatic value), though remaining above this value at α_c .

Finally, we have studied contact angle distributions. Three of these distributions are represented as polar diagrams for $\alpha = 0, 10$ and 20 (or 17.25 for RL) degrees in Fig. 5b. Let us first comment the GG data. The four strongly pronounced lobes are typical of this preparation [13] (chap. 6). The vertical and horizontal directions are always in between these lobes. When the layer is horizontal ($\alpha = 0^\circ$), the orthotropic stiff and soft directions are also found to be (almost) along the horizontal and vertical axis respectively. Note that the fitting procedure effectively gives here $\tau = 93^\circ$ in this case, while $\tau = 90^\circ$ (or 0°) would have been expected for symmetry reasons. This effectively indicates the typical precision we have on the measure of this orthotropic angle. Close to the critical slope, however, the orthotropic orientations are close to those of the lobes, the stiff one being in the direction of the slope. As evidenced in Fig. 5c, the transition between these two microscopic configurations occurs around $\alpha \simeq 9^\circ$, i.e. well below α_c , in correspondence with the drop of G/E_1 between 8° and 10° (see Fig. 4). The polar distributions computed with RL and AV data are more isotropic than in the GG case (Fig. 5b). However, although the lobes are less pronounced, the overall behaviour of the RL data is similar to the GG ones. In the AV case, the orthotropic direction roughly follows that of the lobes over the all range of inclination.

5 Conclusions

To sum up, we have simulated 2D frictional and polydisperse granular layers under gravity inclined at an angle α , and investigated their mechanical and microscopic properties when the unjamming transition is approached. This work tells us what to expect in real experiments, i.e. a layer that becomes elastically softer as $\alpha \rightarrow \alpha_c$, as e.g. inferred from acoustic experiments on a granular packing in the vicinity of the transition [10]. More precisely, the shear modulus G and the stiff Young modulus E_1 both decrease with respect to the soft modulus E_2 , but not to the point at which the system would lose its rigidity before avalanching. In particular, as evidenced by the comparison of the curves in Figs. 4 and 5a, the shear modulus is not found to be a linear function of $Z - Z_{\text{iso}}$ (or $Z^* - Z_{\text{iso}}$), in contrast with the finding of [42] on homogeneous frictional systems, close to isostaticity. In fact, in agreement with the analysis of [21], the idea that the whole granular layer reaches the isostatic limit at the critical angle α_c is too simple because it ignores the anisotropy and inhomogeneity of the packing induced by the preparation and the gravity field. Interestingly, in the simple shear geometry considered in [25], the redundancy factor S does tend to 1 when the critical state is reached, but here remains (slightly) above this value for the avalanched layers, even though some (quasi) sliding contacts appear.

As for perspectives, similarly to what we did for the GG layers in [8], one should compute the vibration modes for the AV layers, taking into account the presence of these quasi-sliding contacts. Also, it could be interesting to use granular simulations with a rolling resistance [15] in order to explore a wider range of ϕ , Z and α .

Acknowledgments We thank I. Cota Carvalho, R. Mari and M. Wyart for fruitful discussions. This work is part of the ANR JamVibe, project # 0430 01. A.P.F. Atman has been partially supported by the exchange program ‘Science in Paris 2010’ (Mairie de Paris) and by a visiting professorship ‘ESPCI-Total’. A.P.F. Atman thanks CNPq and FAPEMIG Brazilian agencies for financial funding, and PMMH/ESPCI for hospitality.

Appendix: Orthotropic elastic response

In this Appendix, we detail elastic calculations on a 2D orthotropic slab of finite thickness h . Following the notations of Fig. 1, we note (1, 2) the orthotropic directions, while (n, t) are the directions respectively normal and tangential to the slab. We note τ the angle between axes (1, 2) and (n, t). For the sake of the computation of the stress profiles in response to a force \mathbf{F}_0 applied at the free surface, one can switch off gravity, and the mechanical equilibrium of the system writes

$$\partial_n \sigma_{nn} + \partial_t \sigma_{tn} = 0 \quad \text{and} \quad \partial_n \sigma_{tn} + \partial_t \sigma_{tt} = 0, \quad (2)$$

where σ_{ij} is the stress tensor. We define the strain tensor u_{ij} from the displacement field u_i as $u_{ij} = \frac{1}{2}(\partial_i u_j + \partial_j u_i)$. It verifies the compatibility condition:

$$\partial_n^2 u_{nn} + \partial_t^2 u_{tt} - 2\partial_n \partial_t u_{tn} = 0. \quad (3)$$

Introducing the two Young moduli E_1 and $E_2 < E_1$, the shear modulus G and two Poisson coefficients ν_{12} and ν_{21} , the generalised Hooke’s law relating strain and stress tensors writes, in the orthotropic axes, as follows:

$$\begin{pmatrix} u_{11} \\ u_{22} \\ u_{12} \end{pmatrix} = \begin{pmatrix} \frac{1}{E_1} & -\frac{\nu_{21}}{E_2} & 0 \\ -\frac{\nu_{12}}{E_1} & \frac{1}{E_2} & 0 \\ 0 & 0 & \frac{1}{2G} \end{pmatrix} \begin{pmatrix} \sigma_{11} \\ \sigma_{22} \\ \sigma_{12} \end{pmatrix}. \quad (4)$$

We call \mathcal{W}_\dagger this 3×3 compliance matrix. It must be symmetric and these coefficients thus verify $\nu_{12}/E_1 = \nu_{21}/E_2$. Elastic energy is well defined if all moduli E_1, E_2, G are positive and $1 - \nu_{12}\nu_{21} > 0$. In (n, t) axes, we have

$$\begin{pmatrix} u_{nn} \\ u_{tt} \\ u_{tn} \end{pmatrix} = \mathcal{W}_\tau \begin{pmatrix} \sigma_{nn} \\ \sigma_{tt} \\ \sigma_{tn} \end{pmatrix} \quad \text{with} \quad \mathcal{W}_\tau = \mathcal{Q}^{-1} \mathcal{W}_\dagger \mathcal{Q} \quad (5)$$

and the rotation matrix

$$\mathcal{Q} = \begin{pmatrix} \cos^2 \tau & \sin^2 \tau & 2 \cos \tau \sin \tau \\ \sin^2 \tau & \cos^2 \tau & -2 \cos \tau \sin \tau \\ -\cos \tau \sin \tau & \cos \tau \sin \tau & \cos^2 \tau - \sin^2 \tau \end{pmatrix}. \quad (6)$$

The matrix \mathcal{W}_τ can be made explicit as follows:

$$\mathcal{W}_\tau = \frac{1}{E_2} \begin{pmatrix} A & -C & 2D \\ -C & B & 2F \\ D & F & H \end{pmatrix}, \quad (7)$$

with

$$A = T \cos^4 \tau + \sin^4 \tau + 2R \cos^2 \tau \sin^2 \tau, \quad (8)$$

$$B = \cos^4 \tau + T \sin^4 \tau + 2R \cos^2 \tau \sin^2 \tau, \quad (9)$$

$$C = \nu_{21} + \cos^2 \tau \sin^2 \tau (2R - 1 - T), \quad (10)$$

$$D = \cos \tau \sin \tau [(\sin^2 \tau - \cos^2 \tau)R + \cos^2 \tau (1 + T) - 1], \quad (11)$$

$$F = \cos \tau \sin \tau [(\cos^2 \tau - \sin^2 \tau)R + \sin^2 \tau (1 + T) - 1], \quad (12)$$

$$H = \nu_{21} - 2 \cos^2 \tau \sin^2 \tau (2R - 1 - T) + R, \quad (13)$$

and where we have introduced the two dimensionless numbers

$$T = \frac{E_2}{E_1} = \frac{\nu_{21}}{\nu_{12}}, \quad \text{and} \quad R = \frac{1}{2} E_2 \left(\frac{1}{G} - \frac{\nu_{12}}{E_1} - \frac{\nu_{21}}{E_2} \right). \quad (14)$$

With the four roots X_k ($k = 1, \dots, 4$) of the biquadratic equation $X^4 + 2RX^2 + T = 0$, that is

$$X = \pm \sqrt{-R \pm (R^2 - T)^{1/2}}, \quad (15)$$

the general solution of the problem can be written as sums of Fourier modes:

$$\sigma_{nn}(n, t) = \sum_{k=1}^4 \int_{-\infty}^{+\infty} b_k(q) e^{iqt+iY_k q n} dq, \quad (16)$$

$$\sigma_{tt}(n, t) = \sum_{k=1}^4 \int_{-\infty}^{+\infty} b_k(q) Y_k^2 e^{iqt+iY_k q n} dq, \quad (17)$$

$$\sigma_{tn}(n, t) = - \sum_{k=1}^4 \int_{-\infty}^{+\infty} b_k(q) Y_k e^{iqt+iY_k q n} dq, \quad (18)$$

where $Y_k = (X_k - \tan \tau)/(1 + X_k \tan \tau)$. The four functions b_k are determined by the boundary conditions at the top and the bottom of the slab.

At the free surface ($n = 0$), the overload force imposes two components of the stress:

$$\sigma_{nn} = F_0 \cos \theta \Delta(t) \quad \text{and} \quad \sigma_{tn} = F_0 \sin \theta \Delta(t), \quad (19)$$

where θ is the angle between \mathbf{F}_0 and the direction of the n axis (see Fig. 1), and where $\Delta(t)$ is a normalised function which tells how this force is distributed along the surface—e.g. a Dirac or a Gaussian of width w_F . We need here its Fourier transform $s(q)$. For the Gaussian case, $s(q) = \frac{1}{2\pi} \exp(-\frac{1}{2} w_F^2 q^2)$. We typically take $w_F \rightarrow 0$ (a δ -peak). These top conditions (19) then give

$$\sum_{k=1}^4 b_k = F_0 \cos \theta s(q) \quad \text{and} \quad \sum_{k=1}^4 b_k Y_k = -F_0 \sin \theta s(q). \quad (20)$$

At the bottom of the slab ($n = h$), we impose rigid and rough conditions, i.e. vanishing displacements in both t and

n directions: $u_t = u_n = 0$. In order to get equations on the functions b_k , we must transform these conditions into equations on the stress components. Taking its derivative along t , the condition $u_t = 0$ gives $u_{tt} = 0$, i.e.

$$-C\sigma_{nn} + B\sigma_{tt} + 2F\sigma_{tn} = 0, \quad (21)$$

leading to

$$\sum_{k=1}^4 b_k \left[-C - 2FY_k + BY_k^2 \right] e^{iY_k q h} = 0. \quad (22)$$

Similarly, the condition $u_n = 0$ gives, after a double derivative along t , the relation $2\partial_t u_{tn} = \partial_n u_{tt}$, leading to

$$\sum_{k=1}^4 b_k \left[2D + (C - 2H)Y_k + 4FY_k^2 - BY_k^3 \right] e^{iY_k q h} = 0. \quad (23)$$

The four linear Eqs. (20, 22, 23) can be inverted, leading to large but analytic expressions for the functions b_k . Integrations over q involved in Eqs. 16–18 must, however, be computed numerically. Finally, the stress components, made dimensionless by F_0/h , can be plotted for given values of the five parameters τ , T , R , v_{21} and θ , as functions of t/h at a given depth (e.g. $n = h$). We checked that the results are insensitive to the value of w_F/h , as long as it remains small.

References

1. Agnolin, I., Roux, J.-N.: Internal states of model isotropic granular packings. I. Assembling processes, geometry and contact networks. *Phys. Rev. E* **76**, 061302 (2007)
2. Agnolin, I., Roux, J.-N.: Internal states of model isotropic granular packings. II. Compression and pressure cycles. *Phys. Rev. E* **76**, 061303 (2007)
3. Agnolin, I., Roux, J.-N.: Internal states of model isotropic granular packings. III. Elastic properties. *Phys. Rev. E* **76**, 061304 (2007)
4. Atman, A.P.F., Brunet, P., Geng, J., Reydellet, G., Claudin, P., Behringer, R.P., Clément, E.: From the stress response function (back) to the sandpile ‘dip’. *Eur. Phys. J. E* **17**, 93 (2005)
5. Atman, A.P.F., Brunet, P., Geng, J., Reydellet, G., Combe, G., Claudin, P., Behringer, R.P., Clément, E.: Sensitivity of the stress response function to packing preparation. *J. Phys. Condens. Matter* **17**, S2391 (2005)
6. Atman, A.P.F., Claudin, P., Combe, G., Goldenberg, C., Goldhirsch, I.: Transitions in the response of a granular layer. In: Nakagawa, M., Luding, S. (eds.) Proceedings of the 6th International Conference on Micromechanics of Granular Media, Powders and Grains 2009, p. 492. American Institute of Physics (2009)
7. Atman, A.P.F., Claudin, P., Combe, G.: Departure from elasticity in granular layers: investigation of a crossover overload force. *Comput. Phys. Commun.* **180**, 612 (2009)
8. Atman, A.P.F., Claudin, P., Combe, G., Mari, R.: Mechanical response of an inclined frictional granular layer approaching unjamming. *Europhys. Lett.* **101**, 44006 (2013)
9. Bi, D., Zhang, J., Chakraborty, B., Behringer, R.P.: Jamming by shear. *Nature* **480**, 355 (2011)
10. Bonneau, L., Andreotti, B., Clément, E.: Evidence of Rayleigh–Hertz surface waves and shear stiffness anomaly in granular media. *Phys. Rev. Lett.* **101**, 118001 (2008)
11. Brito, C., Dauchot, O., Biroli, G., Bouchaud, J.-P.: Elementary excitation modes in a granular glass above jamming. *Soft Matter* **6**, 3013 (2010)
12. da Cruz, F., Emam, S., Prochnow, M., Roux, J.-N., Chevoir, F.: Rheophysics of dense granular materials: discrete simulation of plane shear flows. *Phys. Rev. E* **72**, 021309 (2005)
13. Radjai, F., Dubois, F. (eds.): Discrete-Element Modeling of Granular Materials. ISTE, Wiley (2011)
14. Ellenbroek, W.G., van Hecke, M., van Saarloos, W.: Jammed frictionless disks: connecting local and global response. *Phys. Rev. E* **80**, 061307 (2009)
15. Estrada, N., Taboada, A., Radjai, F.: Shear strength and force transmission in granular media with rolling resistance. *Phys. Rev. E* **78**, 021301 (2008)
16. Geng, J., Howell, D., Longhi, E., Behringer, R.P., Reydellet, G., Vanel, L., Clément, E., Luding, S.: Footprints in sand: the response of a granular material to local perturbations. *Phys. Rev. Lett.* **87**, 035506 (2001)
17. Gland, N., Wang, P., Makse, H.A.: Numerical study of the stress response of two-dimensional dense granular packings. *Eur. Phys. J. E* **20**, 179 (2006)
18. Goldenberg, C., Atman, A.P.F., Claudin, P., Combe, G., Goldhirsch, I.: Scale separation in granular packings: stress plateaus and fluctuations. *Phys. Rev. Lett.* **96**, 168001 (2006)
19. Goldhirsch, I., Goldenberg, C.: On the microscopic foundations of elasticity. *Eur. Phys. J. E* **9**, 245 (2002)
20. Goldhirsch, I., Goldenberg, C.: Friction enhances elasticity in granular solids. *Nature* **435**, 188 (2005)
21. Henkes, S., Brito, C., Dauchot, O., van Saarloos, W.: Local coulomb versus global failure criterion for granular packings. *Soft Matter* **6**, 2939 (2010)
22. Henkes, S., Shundyak, K., van Saarloos, W., van Hecke, M.: Local contact numbers in two-dimensional packings of frictional disks. *Soft Matter* **6**, 2935 (2010)
23. Henkes, S., van Hecke, M., van Saarloos, W.: Critical jamming of frictional grains in the generalized isostaticity picture. *Europhys. Lett.* **90**, 14003 (2010)
24. Heussinger, C., Barrat, J.-L.: Jamming transition as probed by quasistatic shear flow. *Phys. Rev. Lett.* **102**, 218303 (2009)
25. Kruyt, N.P.: Micromechanical study of plasticity of granular materials. *C. R. Mec.* **338**, 596 (2010)
26. Leonforte, F., Tanguy, A., Wittmer, J.P., Barrat, J.-L.: Continuum limit of amorphous elastic bodies II: linear response to a point source force. *Phys. Rev. B* **70**, 014203 (2004)
27. Liu, A.J., Nagel, S.R.: Nonlinear dynamics: jamming is not just cool any more. *Nature* **396**, 21 (1998)
28. Liu, A.J., Nagel, S.R.: Granular and jammed materials. *Soft Matter* **6**, 2869 (2010)
29. Liu, A.J., Nagel, S.R., van Saarloos, W., Wyart, M.: The jamming scenario—an introduction and outlook. In: Berthier, L., Biroli, G., Bouchaud, J.-P., Cipelletti, L., van Saarloos, W. (eds.) *Dynamical Heterogeneities in Glasses, Colloids, and Granular Media*, p. 298. Oxford University Press, Oxford (2011)
30. Majmudar, T.S., Sperl, M., Luding, S., Behringer, R.P.: Jamming transition in granular systems. *Phys. Rev. Lett.* **98**, 058001 (2007)
31. Moukarzel, C.F.: Isostaticity in granular matter. *Granul. Matter* **3**, 41 (2001)
32. O’Hern, C.S., Langer, S.A., Liu, A.J., Nagel, S.R.: Random packings of frictionless particles. *Phys. Rev. Lett.* **88**, 075507 (2002)
33. O’Hern, C.S., Silbert, L.E., Liu, A.J., Nagel, S.R.: Jamming at zero temperature and zero applied stress: the epitome of disorder. *Phys. Rev. E* **68**, 011306 (2003)

34. Otsuki, M., Hayakawa, H.: Critical scaling near jamming transition for frictional granular particles. *Phys. Rev. E* **83**, 051301 (2011)
35. Otto, M., Bouchaud, J.-P., Claudin, P., Socolar, J.E.S.: Anisotropy in granular media: classical elasticity and directed force chain network. *Phys. Rev. E* **67**, 031302 (2003)
36. Rapaport, D.C.: *The Art of Molecular Dynamics Simulation*. Cambridge University Press, Cambridge (1995)
37. Roux, J.-N.: Geometric origin of mechanical properties of granular materials. *Phys. Rev. E* **61**, 6802 (2000)
38. Serero, D., Reydellet, G., Claudin, P., Clément, E., Levine, D.: Stress response function of a granular layer: quantitative comparison between experiments and isotropic elasticity. *Eur. Phys. J. E* **6**, 169 (2001)
39. Silbert, L.E.: Jamming of frictional spheres and random loose packing. *Soft Matter* **6**, 2918 (2010)
40. Silbert, L.E., Ertaş, D., Grest, G.S., Halsey, T.C., Levine, D.: Geometry of frictionless and frictional sphere packings. *Phys. Rev. E* **65**, 031304 (2002)
41. Shundyak, K., van Hecke, M., van Saarloos, W.: Force mobilization and generalized isostaticity in jammed packings of frictional grains. *Phys. Rev. E* **75**, 010301 (2007)
42. Somfai, E., van Hecke, M., Ellenbroek, W.G., Shundyak, K., van Saarloos, W.: Critical and noncritical jamming of frictional grains. *Phys. Rev. E* **75**, 020301 (2007)
43. Staron, L., Villette, J.-P., Radjai, F.: Preavalanche instabilities in a granular pile. *Phys. Rev. Lett.* **89**, 204302 (2002)
44. Tkachenko, A.V., Witten, T.A.: Stress propagation through frictionless granular material. *Phys. Rev. E* **60**, 687 (1999)
45. van Hecke, M.: Jamming of soft particles: geometry, mechanics, scaling and isostaticity. *J. Phys. Condens. Mat.* **22**, 033101 (2010)
46. Wyart, M., Nagel, S.R., Witten, T.A.: Geometric origin of excess low-frequency vibrational modes in weakly connected amorphous solids. *Europhys. Lett.* **72**, 486 (2005)
47. Zhang, H.P., Makse, H.A.: Jamming transition in emulsions and granular materials. *Phys. Rev. E* **72**, 011301 (2005)

A.4 *Non-Gaussian behavior in jamming / unjamming transition in dense granular materials*

Este artigo foi publicado no quatrienal do congresso *Powders & Grains 2013*, que é o maior congresso sobre materiais granulares, e que estava em sua 7^a edição.

Non-Gaussian behavior in jamming / unjamming transition in dense granular materials

A. P. F. Atman*, E. Kolb[†], G. Combe**, H. A. Paiva[‡] and G.H.B. Martins §

*Departamento de Física e Matemática and National Institute of Science and Technology for Complex Systems,
Centro Federal de Educação Tecnológica de Minas Gerais, CEFET-MG,
Av. Amazonas 7675, 30510-000, Belo Horizonte, MG, Brazil.

[†]PMMH, CNRS UMR 7636, UPMC and Université Paris Diderot, ESPCI-ParisTech,
10 rue Vauquelin, 75231 Paris Cedex 05, France

^{**}Laboratoire 3S-R (Sols,Solides,Structures - Risques) UMR 5521 (UJF, INPG, CNRS) BP 53, Grenoble, France.

[‡]Departamento de Física e Matemática, CEFET-MG.

[§]Departamento de Engenharia Elétrica, CEFET-MG.

Abstract. Experiments of penetration of a cylindrical intruder inside a bidimensional dense and disordered granular media were reported recently showing the jamming / unjamming transition. In the present work, we perform molecular dynamics simulations with the same geometry in order to assess both kinematic and static features of jamming / unjamming transition. We study the statistics of the particles velocities at the neighborhood of the intruder to evince that both experiments and simulations present the same qualitative behavior. We observe that the probability density functions (PDF) of velocities deviate from Gaussian depending on the packing fraction of the granular assembly. In order to quantify these deviations we consider a q -Gaussian (Tsallis) function to fit the PDF's. The q -value can be an indication of the presence of long range correlations along the system. We compare the fitted PDF's obtained with those obtained using the stretched exponential, and sketch some conclusions concerning the nature of the correlations along a granular confined flow.

Keywords: jamming/unjamming transition, granular systems, q -gaussian distributions, flow in channels

PACS: 81.05.Rm, 05.10-a, 83.50.Ha

INTRODUCTION

Due to its importance for technological applications as well for better understanding of natural phenomena, in last years increasing interest has been paid on the so-called jamming/unjamming transition in confined granular systems [1, 2, 3, 4, 5]. Of particular interest is the clogging of granular material around an intruder – or obstacle– which is a quite common situation in the industry (transport and confining materials) or civil engineering (pile driving for deep foundations). From the mechanical point of view, this type of experiment may provide a better understanding of yielding in granular media by observing directly the structural and dynamic features of the mechanisms which govern the plasticity in dense granular media [4, 5, 6]. Thus, the study of the rheology of a confined granular system close to the jamming became one of the key points of current research, and one of the fundamental issues on current research is to characterize the velocity distribution which governs the system at different jamming/unjamming situations. It is well known that, assuming molecular chaos hypothesis, the expected distribution for a set of colliding particles is that from Maxwell-Boltzmann theory, the Gaussian distribution with its typical bell-shape format and, indeed, it is observed in dilute granular systems and granular

gases [7, 8]. However, previous studies in different confining situations (jamming) [9, 10, 11] have shown that the measured distribution usually deviates a lot from the Gaussian, and the function generally used to fit the data in this scenario is the stretched exponential [12, 13].

In this work, we propose to investigate the grain velocities' distribution around the intruder as a function of the packing fraction of the granular system, in order to verify a possible connection between the characteristic exponent of the distribution and the degree of jamming. We have fitted the data by two kinds of probability distribution functions (PDF's). First, we have considered the stretched exponential,

$$f_\alpha(x) = A * \exp(B * (x - x_0)^\alpha), \quad (1)$$

where A , B , and x_0 are free parameters usually employed in the fit function, and α is the degree of the distribution. Second, we have used the q -Gaussian which was proposed by C.Tsallis [14] as a generic distribution to describe pdf in non-extensive systems:

$$f_q(x) = \frac{\sqrt(D)}{C} (1 - Dx^2(1 - q))^{-\frac{1}{1-q}}, \quad (2)$$

where D is an adjustable parameter (analogous to the inverse of temperature in the Boltzmann-Gibbs formula-

METHODOLOGY

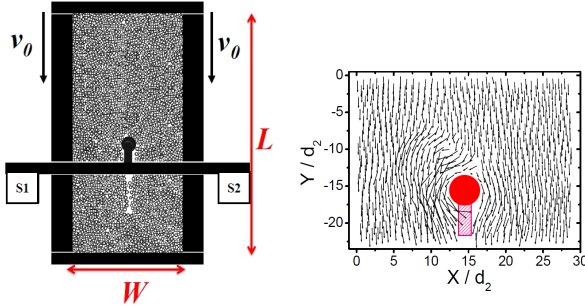


FIGURE 1. Schematic of the experiment. The containing box of dimensions $W = 54 d_2$ and $L \leq 94 d_2$ is placed horizontally over a translating plate and filled with the bidisperse mixture with 7 : 4 proportion of large to small disks. The arrows on both sides indicate the movement of the box at velocity v_0 ; the small circle in the middle marks the intruder, which is fixed in the laboratory frame and connected to two force sensors S1 and S2. The right panel shows a typical displacement map obtained between two successive snapshots with a magnification factor of 50.

tion) and C is a normalization factor. In the fitting procedure, we let D and C vary as free parameters. For tangential velocity distributions for q -gaussian as well as for stretched exponential fits, we also included a 4th parameter, x_0 in order to consider distributions not centered at the origin. The parameter q , which gives the name of this q -Gaussian PDF, is the control parameter which allows to recover the usual Gaussian distribution when $q = 1$, while for $q > 1$ we should expect long range correlations along the system. The major advantage of this particular choice for the PDF is its ability to fit all the data range with a single function, and no need to use a combination of stretched exponential and Gaussian to fit separately the tail and the central part of the distribution [3]. Another interesting feature of the q -Gaussian is the possibility to link directly the value of the q to the length of correlations along the system. For $q = 1$, we expect short range correlations, as assumed in the molecular chaos hypothesis; for $q > 1$, long-range correlations should arise in the system, and the distribution exhibits heavy tails. Thus, we expect that for unjammed, looser systems, the velocity distribution should be rather well described by Gaussian functions or q -Gaussians with $q \rightarrow 1$, while for jammed situations we expect to find a good fit with $q > 1$.

The paper is structured as the following: in the next section we present the experimental set up and the simulation method, and the analysis technique to build the distributions. Next, we compare the fitted exponent values for the experiments and simulations, and their dependence with the packing fraction ϕ and temporal evolution. Finally, we sketch some conclusions.

The experimental setup was already presented in details previously [5] and consists in an horizontal rectangular box filled with a bidisperse mixture of grains – see Figure 1. with $d_2 = 1.25 d_1$, where d_2 (d_1) is the diameter of the large (resp. small) species. In the experiments shown, typically around ~ 6500 grains were used. The packing fraction ϕ was adjusted to $0.8 < \phi < 0.84$, typically below or equal the jamming packing fraction for a frictional granular medium. A CCD camera of 1600×1200 pixels placed above the set-up recorded images every $d_2/30$ displacement of the box, while the box was pulled at a constant velocity v_0 along the tangential t direction. Then an image analysis software is used to localize the positions of grains in each image. By calculating the displacement of each grain between successive images, we construct the cumulative velocity PDF and fit with the q -Gaussian function and stretched exponential, as shown in Figure 2. More precisely, we measured the velocity distributions along the normal v_n and tangential v_t directions of box displacement. We used a minimum square method to obtain the best fit values for the PDF's using equations 1 and 2 as fitting functions.

The simulation is designed to be closer as possible to the experimental situation. We have used a molecular dynamics (MD) code in 2 dimensions, with velocity Verlet implementation and 3rd order Gear predictor-corrector [15]. The rheology for the particles was a modified version of the original Cundall-Strack model [16], with the contact between grains represented as normal and tangential springs, and Coulomb friction between grains. The simulated system has the same geometry, number of grains and aspect ratio as the experimental setup, but the range of packing fraction values simulated was a bit different from the experiments, since we can better explore the parameter space with simulations. Besides, the microscopic parameters were chosen in order to get the best performance for the code, and do not correspond literally to the values expected if a direct conversion of the experimental values was made. Thus, in normalized units the values used for the parameters were: $k_n = 1000$, $k_t = 750$ for the normal and tangential spring stiffnesses, and $\mu = 0.5$ for the friction coefficient. We have used a critical damping in the normal direction of the contacts, but no damping in the tangential one, only Coulomb friction dissipates energy in tangential contact direction. (Please find in [17] the precise definitions of the normalized unities and in [18] more details concerning the simulation method. The normalization of length used here was the width of the system, W).

We ran simulations with the same number of realizations as performed in the experiments. Then we averaged the same number of snapshots to build the velocity pdf's (the “snapshots” in simulations correspond to the config-

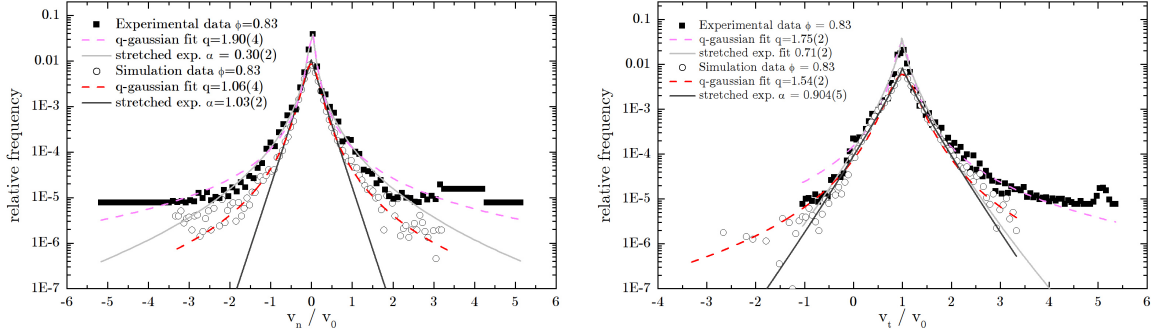


FIGURE 2. Velocities PDF's for experimental data and simulations. The distribution along the normal direction of displacement is shown at left while the distribution along the tangential direction is shown at right.

urations taken at the same frequency as in the experiment – at each $d_2/30$ displacement of the box. Thus, we were able to compare directly simulations with experimental data - Figure 2.

The distributions usually considered about 160 consecutive snapshots, and we averaged the velocities obtained from the displacements calculated between 2 consecutive snapshots (please find interesting features when different values of snapshots are used to calculate the displacement [19]). A typical experiment runs along 1600 snapshots and we can obtain the temporal evolution of the distribution. We show here only the results for distributions taken in front of the intruder in a region corresponding to the right panel of Figure 1. We study the temporal evolutions of the best fit parameters for the two PDF's used to fit the data as well the dependence of the fitted value at the half time of the experiment in function of the initial packing fraction ϕ .

DISCUSSION

In figures 2 we show some results for the velocities PDF's at the same packing fraction, for experiments and simulations. Despite not observing a perfect match, most of the qualitative features observed in the experimental PDF's were successfully reproduced by simulation and, sometimes, even quantitatively. For example, the distributions for $v_{n,t}/v_0 < 1$ show a remarkable match. Moreover, some observations were common to all packing fractions:

- First, it is clear that the confinement provoked by the presence of the intruder induces strong correlations for grains velocities, expressed by heavy tail distributions.
- Due probably to the box aspect ratio, longer than wider, we observe that the confining effect – jamming – is stronger in the normal velocities distribu-

tion than in tangential one. Thus, we have systematically verified that the stretched exponential fits v_n distributions better than q -Gaussian, since the systems are almost completely correlated along this direction.

- The v_t distributions were frequently asymmetrical, with heavy tails with different sizes for $v_t/v_0 > 1$ and $v_t/v_0 < 1$. The long heavy tails for $v_t/v_0 > 1$ systematically were better fitted by q -Gaussian.

The asymmetry observed in the tangential case can be explained considering the rectangular region of snapshot around the intruder: since the intruder is placed in the central bottom part of the region, most of the particles in average were placed in front of the intruder and moving with the same velocity as the box. As they approached the intruder, due to the flux conservation in average, the grains gained velocity, and competed to pass aside the intruder. Other grains which are located just in front of the intruder slowed down, and an excess of small velocities is observed in the distributions. The recirculation of grains just in the vicinity of the intruder (see the right panel in Figure 1) contributes for the negative values of velocities.

Another feature is the excess of velocities for experimental distributions close to $v_t/v_0 = 1$ and $v_n/v_0 = 0$, compared with simulations. This is probably due to the limited experimental frame of observation: When a new grain enters in the window observation, its preceding position is not known. Thus its first velocity is arbitrarily set to 0 in normal direction and to v_0 in the tangential one. Therefore we systematically observe an excess of velocities v_n close to zero or v_t close to v_0 in experiments compared with simulations where all the velocities are known, even outside the window observation.

Figure 3 shows the temporal evolution of the fitted parameter q from the q -Gaussian PDF's at the same value of packing fraction. We observe that the values obtained in the experiments are almost constant (except at the

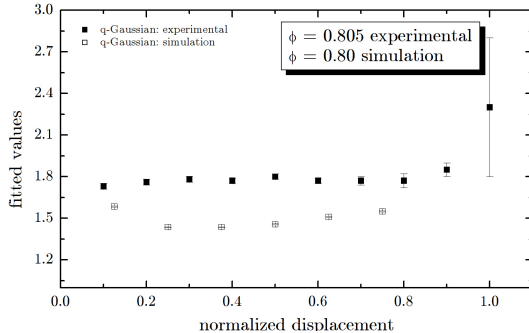


FIGURE 3. Temporal evolution of the exponents of the PDF's used to fit the data, for the packing fraction $\phi = 0.805$ in the experimental case, and $\phi = 0.8$ in simulation. Both plots show the q -Gaussian best fit for v_t in function of the normalized displacement of the containing box.

end of travelling), while in the simulations we observe a rather small but non-monotonic variation with time.

Figure 4 shows results for the fitted exponents q in function of the packing fraction. Clearly, the simulation data show a clear tendency for $q \rightarrow 3/2$ as the packing fraction increases. The experimental results, however, do not show clearly this feature, which could be due to the excess of experimental velocity v_t close to v_0 , as previously discussed. Another possible explanation, is the absence of friction between grains and the table in the case of the simulation. In simulations, since we considered the 2D case, we have no manner to implement this friction. In the experiments, the region in front of the intruder attains progressively a critical packing fraction as the box moves, and we can observe voids and inhomogeneities in the packing of grains. In simulations, the system is considerably more homogeneous, and maybe it can explain why the simulation displays monotonic dependence on the values of the fitted parameters with the packing fraction while the experimental results are inconclusive.

CONCLUSIONS AND PERSPECTIVES

We have presented experimental and simulation results for the velocity PDF's of confined granular systems in the presence of an intruder. We fit the data with q -Gaussian and stretched exponential functions, and sketch the temporal evolution of the fitted values. We verified that the system exhibits strong correlations in both normal and tangential directions, expressed by the $q > 1$ and $\alpha < 1$, but we could not verify quantitative concordance between the simulations and experiments. In simulations, a clear monotonic tendency was verified, pointing to $q \rightarrow 3/2$ and $\alpha \rightarrow 1$ as ϕ increases, but the experimental values do not display any clear tendency.

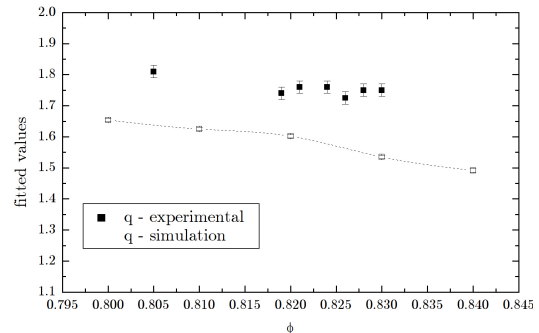


FIGURE 4. Dependence of the fitted values with the packing fraction. The best fitted values of the pdf used - q -Gaussian - were shown in function of the packing fraction at the half-time of the experiment, for v_t distribution.

ACKNOWLEDGMENTS

APFA and GHBM thanks FAPEMIG and CNPq for financial support. APFA and GC thanks CEFET and Université Joseph Fourier for making possible a 3 month invited professor grant.

REFERENCES

1. R. P. B. H. M. Jaeger, S. R. Nagel, *REV MOD PHYS* **68**, 1259 (1996).
2. M. S. Y. Murayama, *J PHYS SOC JAP* **67**, 1826 (1998).
3. P. R. N. S. Moka, *PHYS REV LETT* **95**, 068003 (2005).
4. J. L. P. C. E. C. E. Kolb, J. Cvikelinski, *PHYS REV E* **69**, 031306 (2004).
5. N. G. P. Cixous, E. Kolb, and J.-C. Charmet, *Powders and Grains 2009 AIP Conference Proceedings* **1145**, 539 (2009).
6. A. L. E. K. J. C. J. L. E. C. G. Caballero, E. Kolb, *J PHYS COND MATT* **17**, S2503 (2005).
7. F. C. M. J.S. van Zon, *PHYS REV LETT* **93**, 038001 (2004).
8. J. S. O. J. S. Urbach, *PHYS REV E* **60**, R2468 (1999).
9. A. K. D. L. Blair, *PHYS REV E* **64**, 050301(R) (2001).
10. A. K. A. V. Orpe, *PHYS REV LETT* **98**, 238001 (2007).
11. H. H. A. Kawarada, *J PHYS SOC JAP* **73**, 2037 (2004).
12. N. M. F. Rouyer, *PHYS REV LETT* **85**, 3676 (2000).
13. A. V. A. Puglisi, F. Cecconi, *J PHYS COND MATT* **17**, S2715 (2005).
14. C. Tsallis, *BRAZ J PHYS* **39**, 337 (2009).
15. D. T. M.P. Allen, *Computer simulation of liquids*, Oxford University Press, Oxford, 1987.
16. O. S. P.A. Cundall, *GEOTECHNIQUE* **29**, 47 (1979).
17. G. C. A.P.F. Atman, P. Claudin, *COMP PHYS COMM* **180**, 612 (2009).
18. J. G. G. R. G. C. P. C. R. P. B. E. C. A. P. F. Atman, P. Brunet, *J PHYS COND MATT* **17**, S2391 (2005).
19. G. V. V. Richefeu, G. Combe, *GÉOTECH LETT* **2**, 113 (2012).

Appendix B – Códigos

Coloquei os códigos utilizados para este projeto de tese em um GIT para a maior comodidade e facilidade do acesso. O endereço eletrônico é <<https://github.com/BoscoWarhammer/Doutorado>>.

Appendix C – Turbulence

C.1 Turbulent steady-state regime

There are several turbulence models to be addressed in a fluid approach. In this work we choose the Prandtl turbulence model and the term turbulent viscosity is presented as in the following equation:

$$\begin{aligned} \nu_t &= l^2 |\dot{\gamma}|, \text{ in other words,} \\ \nu_t &= l^2 \left| \frac{\partial u_x}{\partial z} \right|, \end{aligned} \quad (72)$$

where ν_t is the turbulent model, l is the characteristic vortex turbulence length, $\dot{\gamma}$ is the fluid strain rate, u_x is the fluid velocity in the flow direction and z is the gravity direction.

Fluid shear controls some fluid characteristics, such as the flow regime. The equation that governs shear is the equation:

$$\tau = \rho^f \left(\nu + l^2 \left| \frac{\partial u_x}{\partial z} \right| \right) \frac{\partial u_x}{\partial z}, \quad (73)$$

where τ is the shear flow, ρ^f is the fluid density, ν is the intrinsic fluid viscosity, $l^2 \left| \frac{\partial u_x}{\partial z} \right|$ is the viscosity term that emulates average turbulence¹ and $\frac{\partial u_x}{\partial z}$ is the fluid strain rate tensor and is equivalent to the Equation 22.

For the mixture of fluid and granular, we take the characteristic length of the turbulence always above the static layers of the granular material, and therefore assume the behavior of the turbulent characteristic length described by the Equation 74, proposed by van Driest [81]:

$$l(z_b) = \begin{cases} 0 & \text{se } z \leq z_b, \\ \kappa(z - z_b) \left[1 - e^{-(z-z_b)\frac{u_*}{\sqrt{\mathcal{R}_{vD}}}} \right] & \text{if } z > z_b, \end{cases} \quad (74a)$$

$$(74b)$$

where $l(y_b)$ is the turbulent characteristic length, $\kappa \approx 0.4$ is the von Karman's constant, z is the height of the fluid, z_b is the position of the granular bed, u_* is the characteristic shear velocity imposed at the top of the fluid, ν is the viscosity of the fluid and $\mathcal{R}_{vD} \approx 26$ is the van Driest's Reynolds number [81]. However, other characteristic lengths of turbulence were taken into account and are described in the references [81, 82].

We wish to find the final velocity profile that does not change in time, like equation 27, and by consequence, also the shear profile does not change in space, like Equation 28. Again, if Equation 28 do not change in space, then τ is a constant everywhere, making Equation 29 to be a constant. Making explicit the change of velocity in function of space

¹ RANS - Reynolds average Navier-Stokes: time average equations of the motion for fluid flow.

$(\partial u / \partial z)$, we get Equation 75, with $\partial u / \partial z \geq 0$. It means that Equation 75 must be integrated according to z to get the velocity profile of the fluid.

$$\frac{\partial u}{\partial z} = \frac{-v + \sqrt{v^2 + 4l^2\tau/\rho}}{2l^2}, \quad (75)$$

with $\tau = \rho u_*^2$ imposed on top, and it is constant everywhere. In the case of this this equation, the solution is not analytical, and we computed it through Runge-Kutta 4th order solution², presented in equation 90. Figure 48 shows us the shape of the normalized solution to equation 75.

To best characterize the solution of equation 75, we are going to looking at the two asymptotic behaviors it has: one lower, at $z \rightarrow 0$, and the other at $z \rightarrow \infty$. When $z \rightarrow 0$, the mixing length tends to zero because the exponential tends to one, killing the contribution of the mixing length. So, for small size, compared with the characteristic length of the fluid (u_*/v), the fluid behave as a viscous fluid. Then the asymptotic behavior near to the wall:

$$\lim_{z \rightarrow 0} \frac{\partial u}{\partial z} = \frac{u_*^2}{v}, \quad (76)$$

we get equation 29, because we are working with a very small mixing length, given by equation 74. We already know this solution, and it is showed in equation 30. On the other hand, the other asymptotic at $z \rightarrow \infty$, leads the mixing length to κz because the exponential tends to zero, having almost the full contribution of κz , then the asymptotic equation to be analyzed is:

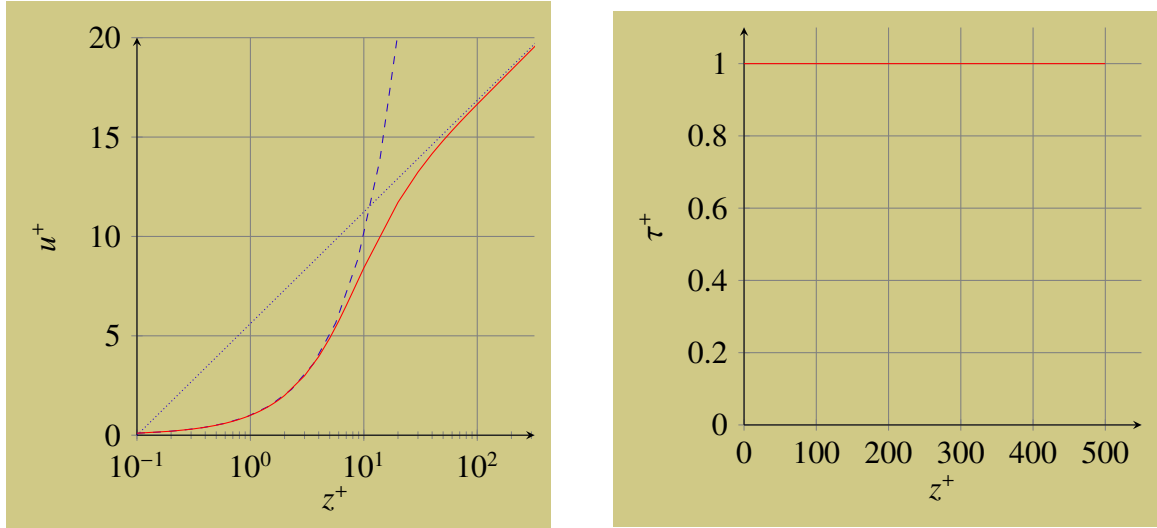
$$\lim_{z \rightarrow \infty} \frac{\partial u}{\partial z} = \frac{u_*}{\kappa z}, \quad (77)$$

and the solution to this differential equation is, as next:

$$u^+ = \frac{1}{\kappa} \ln \left(\frac{z}{z_0} \right), \quad (78)$$

where $z_0 = 0.1v/u_*$ is the length that came from a perfect flat surface in a pure turbulent regime, and it is as if it scales with this perfect flat surface, although it faces a viscous sublayer.

² In section B we are presenting the Runge-Kutta method to solve a ordinary differential equation numerically.



(a) Normalized velocity of viscous-turbulent steady-state profile. (b) Normalized shear of viscous-turbulent steady-state profile.

Figure 48 – Velocity and shear steady-state profiles for the viscous-turbulent fluid. The red continuous line is the solution to van Driest's equation. The dashed blue line is the viscous asymptotic regime, like in the previous section 6.1.1. The dotted blue line is the pure turbulent behavior, which corresponds to the normalized velocity profile: $u^+ = \kappa^{-1} \ln(z^+/0.1)$.

As expected, there is a viscous sublayer regime, combined with a transitional layer to the turbulent behavior. The profile of the viscous regime is linear profile, while the turbulent regime has an asymptotic to logarithmic function. Again, as we are not limited by an upper boundary, the fluid has an infinity characteristic length in the steady-state regime.

C.1.0.1 A little bit more complicated mixing length

This complication on mixing length will give us a different approach to the temporal evolution of the fluid equation. To the steady state, it was built to give approximately same result as equation 74. Equation 79 has been proposed by Orencio Durán in [81].

$$\frac{\partial l}{\partial z} = \kappa \left[1 - e^{-\sqrt{\frac{1}{R_c}} \left(\frac{ul}{v} \right)} \right], \quad (79)$$

where $R_c = 7$ is a Reynolds number that control the response of the equation to achieve the best comparison of the velocity profile obtained by integration of this equation to the one obtained using the van Driest's expression 74. With equation 75 and 79, we can write a system and solve by Runge-Kutta method extended to first-order ODEs, as shown in B.

ANNEX

Annex A – Solving the diffusion equation

In this part, I will show the calculations we did for previous parts in Chapter 6, with some details and some tricks to handle with it, if it is necessary. In this sense, we can start with the linear diffusion equation (equations 80), and its solution is presented at [80], chapter 10.

$$\rho \frac{\partial u}{\partial t} = \frac{\partial \tau}{\partial z}, \quad (80a)$$

$$\tau = \rho v \frac{\partial u}{\partial z}. \quad (80b)$$

To solve this system, we need to know two boundary conditions and the initial condition. As we have discussed in section 6.1.1, the boundary conditions gives us the initial and the final condition, once we are going to change between one known steady state to another known steady state with a difference of Δu_* between them (equation 30 has all information to give us initial and final condition). To solve equations 80, we apply a variable separation on the function by guessing the solution is in the form of:

$$u(t,z) = Z(z)T(t). \quad (81)$$

Rewriting equations 80 with guess 81, we get:

$$\frac{1}{T} \frac{dT}{dt} = \frac{v}{Z} \frac{d^2Z}{dz^2} = -\lambda^2. \quad (82)$$

As we know the steady state, and it must fulfill as solution of the equation, we will remove it from transient. Calling $s(z) = u(z,t \rightarrow \infty)$, the final steady state, and $w(z,t) = u(z,t) - s(z)$ the transient solution of the diffusion equation, we get:

$$\frac{\partial u}{\partial t} = \frac{\partial}{\partial t} [s(z) + w(z,t)] \implies \frac{\partial u}{\partial t} = \frac{\partial w}{\partial t}, \quad (83a)$$

$$\frac{\partial^2 u}{\partial z^2} = \frac{\partial^2}{\partial z^2} [s(z) + w(z,t)] \implies \frac{\partial^2 u}{\partial z^2} = \frac{\partial^2 s}{\partial z^2} + \frac{\partial^2 w}{\partial z^2}, \quad (83b)$$

and since $s(z) = z(u_* + \Delta u_*)^2/\nu$, $\partial^2 s/\partial z^2 = 0$. Applying all condition, we get the following:

$$w(z = 0, t) = u(0, t) - s(0) \implies w(z = 0, t) = 0 \quad \text{Bottom wall}, \quad (84\text{a})$$

$$\frac{\partial w(z = h, t)}{\partial z} = \frac{\partial u(z = h, t)}{\partial z} - \frac{\partial s(z = h)}{\partial z} \implies \frac{\partial w(z = h, t)}{\partial z} = 0 \quad \text{Top shear}, \quad (84\text{b})$$

$$w(z, t = 0) = u(z, t = 0) - s(z) \implies w(z, t = 0) = -z \frac{2u_*\Delta u_* + (\Delta u_*)^2}{\nu} \quad \text{Initial}. \quad (84\text{c})$$

The solutions for the transient regime are, considering that $w = w_t(t)w_z(z)$:

$$\frac{\dot{w}_t}{\nu w_t} = -\lambda^2 \implies w_t = A e^{-\lambda^2 \nu t}, \quad (85\text{a})$$

$$\frac{w''_z}{\nu w_z} = -\lambda^2 \implies w_z = B_1 \sin(\lambda z) + B_2 \cos(\lambda z). \quad (85\text{b})$$

Now we can see that solutions must have the form of an exponential decay according the transition between one steady state and another, and at same time, they should be written in modes of sin and cos. To determine some missing coefficients, we need to apply boundary conditions to this solutions:

$$w(z = 0, t) = 0 \implies B_2 = 0, \quad (86\text{a})$$

$$\frac{\partial w(z = h, t)}{\partial z} = 0 \implies \lambda = \pi \frac{2n - 1}{2h}, \quad (86\text{b})$$

and initial condition

$$w(z, t = 0) = -z \frac{2u_*\Delta u_* + (\Delta u_*)^2}{\nu} \implies A \cdot B_1 = \frac{2}{h} \int_0^h \left[-z \frac{2u_*\Delta u_* + (\Delta u_*)^2}{\nu} \right] \sin(\lambda z) dz, \quad (87)$$

since we have rewritten initial condition to same base of solution, by a Fourier's series. Fourier modes appear in initial condition "caused" by boundary conditions in the nature of the equation. Only certain frequencies can appear in the solution, and they are given by this Fourier's frequencies of final solution:

$$\frac{2}{h} \int_0^h \left[-z \frac{2u_*\Delta u_* + (\Delta u_*)^2}{\nu} \right] \sin(\lambda z) dz = \frac{8h}{\pi^2} \left[\frac{2u_*\Delta u_* + (\Delta u_*)^2}{\nu} \right] \sum_{n=1}^{\infty} \frac{(-1)^n}{(2n-1)^2} \sin(\lambda z), \quad (88)$$

just another way to describe the initial condition in same base of allowed solutions.

Final solution is then in the form of:

$$u(z, t) = \frac{(u_* + \Delta u_*)^2}{\nu} z + \frac{8h}{\pi^2} \left[\frac{2u_*\Delta u_* + (\Delta u_*)^2}{\nu} \right] \sum_{n=1}^{\infty} \frac{(-1)^n}{(2n-1)^2} \sin(\lambda z) e^{-\lambda^2 \nu t}, \quad (89)$$

by summing steady state and transient state.

Annex B – Runge-Kutta

The main advantage here is the precision in calculations than in Euler method. Runge-Kutta method uses the explicit way to calculate the first approximation order and implicit way to correct the higher orders. If the differential function is independent of the function, than Runge-Kutta is the 1/6 Simpson integration rule. The method consist in calculate the differential equation as:

$$y_{n+1} = y_n + \frac{k_{na} + 2k_{nb} + 2k_{nc} + k_{nd}}{6} \Delta x, \quad (90)$$

where

$$k_{na} = f(x_n, y_n), \quad (91a)$$

$$k_{nb} = f\left(x_n + \frac{\Delta x}{2}, y_n + \frac{\Delta x k_{na}}{2}\right), \quad (91b)$$

$$k_{nc} = f\left(x_n + \frac{\Delta x}{2}, y_n + \frac{\Delta x k_{nb}}{2}\right), \quad (91c)$$

$$k_{nd} = f(x_n + \Delta x, y_n + \Delta x k_{nc}), \quad (91d)$$

and the global error associated with the calculation is in the order of $(\Delta x)^4$.

Also, we can extend the method to solve first-order ODEs system. The system must be differentiated at the same variable, and for each sub-step, we repeat the process of calculation for each first-order equation. This is useful when we use high-order ODE, cause we always can rewrite high-order ODE into n first-order ODEs. An example of a 2 equation system:

$$\frac{dy}{dx} = f(x, y, z), \quad (92a)$$

$$\frac{dz}{dx} = g(x, y, z), \quad (92b)$$

with discretization onto variable x , y and z becomes

$$y_{n+1} = y_n + \frac{k_{na} + 2k_{nb} + 2k_{nc} + k_{nd}}{6} \Delta x, \quad (93a)$$

$$z_{n+1} = z_n + \frac{l_{na} + 2l_{nb} + 2l_{nc} + l_{nd}}{6} \Delta x, \quad (93b)$$

where

$$k_{na} = f(x_n, y_n, z_n), \quad (94a)$$

$$l_{na} = g(x_n, y_n, z_n), \quad (94b)$$

$$k_{nb} = f\left(x_n + \frac{\Delta x}{2}, y_n + \frac{\Delta x k_{na}}{2}, z_n + \frac{\Delta x k_{na}}{2}\right), \quad (94c)$$

$$l_{nb} = g\left(x_n + \frac{\Delta x}{2}, y_n + \frac{\Delta x k_{na}}{2}, z_n + \frac{\Delta x l_{na}}{2}\right), \quad (94d)$$

$$k_{nc} = f\left(x_n + \frac{\Delta x}{2}, y_n + \frac{\Delta x k_{nb}}{2}, z_n + \frac{\Delta x k_{nb}}{2}\right), \quad (94e)$$

$$l_{nc} = g\left(x_n + \frac{\Delta x}{2}, y_n + \frac{\Delta x k_{nb}}{2}, z_n + \frac{\Delta x k_{nb}}{2}\right), \quad (94f)$$

$$k_{nd} = f(x_n + \Delta x, y_n + \Delta x k_{nc}, z_n + \Delta x l_{nc}), \quad (94g)$$

$$l_{nd} = g(x_n + \Delta x, y_n + \Delta x k_{nc}, z_n + \Delta x l_{nc}), \quad (94h)$$

and the global error associated with the calculation is still in the order of $(\Delta x)^4$.